The Thesis Committee for John Philip Mersch
Certifies that this is the approved version of the following thesis:

On the Hydraulic Bulge Testing of Thin Sheets

APPROVED BY
SUPERVISING COMMITTEE:

Supervisor:

Stelios Kyriakides, Supervisor

Kenneth Liechti

On the Hydraulic Bulge Testing of Thin Sheets

by

John Philip Mersch, BS

Thesis

Presented to the Faculty of the Graduate School of

The University of Texas at Austin

in Partial Fulfillment

of the Requirements

for the Degree of

Master of Science in Engineering

The University of Texas at Austin

December 2013

Acknowledgements

I would like to thank my advisor, Dr. Stelios Kyriakides, for his dedication to furthering myself as a student, engineer, and person. I believe I have improved under his direction in many ways. I would also like to thank Dr. Kuwabara for sharing his bulge tester design, giving me a great starting point for my own design. This work was conducted with financial support from the MURI project N00014-06-1-0505-A00001. This support as well as that of the University of Texas through a teaching assistantship are acknowledged with thanks. My work also received partial support from Sandia National Laboratories with Dr. Edmundo Corona as the main contact.

The hard work and attention to detail of machinists Travis Crooks, Ricardo Palacios, Israel Gutierrez, and Joe Pokluda, and electrician Pablo Cortez, were essential to the success of this project, and I thank them for their important contributions. I would also like to thank my fellow graduate students, especially Dr. Liang-Hai Lee for his help with ABAQUS and Nathan Bechle for his help in the lab.

I would finally like to thank my friends and family for their constant love and support. You have carried me to places I never thought I could go, and I am forever thankful.

Abstract

On the Hydraulic Bulge Testing of Thin Sheets

John Philip Mersch, MSE

The University of Texas at Austin, 2013

Supervisor: Stelios Kyriakides

The bulge test is a commonly used experiment to establish the material stress-strain response at the highest possible strain levels. It consists of a metal sheet placed in a die with a circular opening. It is clamped in place and inflated with hydraulic pressure. In this thesis, a bulge testing apparatus was designed, fabricated, calibrated and used to measure the stress-strain response of an aluminum sheet metal and establish its onset of failure. The custom design incorporates a draw-bead for clamping the plate. A closed loop controlled servohydraulic pressurization system consisting of a pressure booster is used to pressurize the specimens. Deformations of the bulge are monitored with a 3D digital image correlation (DIC) system. Bulging experiments on 0.040 in thick Al-2024-T3 sheets were successfully performed. The 3D nature of the DIC enables simultaneous estimates of local strains as well as the local radius of curvature. The successful performance of the tests required careful design of the draw-bead clamping arrangement.

Experiments on four plates are presented, three of which burst in the test section as expected. Finite deformation isotropic plasticity was used to extract the true equivalent stress-strain responses from each specimen. The bulge test results correlated well with the

uniaxial results as they tended to fall between tensile test results in the rolling and transverse directions. The bulge tests results extended the stress-strain response to strain levels of the order of 40%, as opposed to failure strains of the order of 10% for the tensile tests.

Three-dimensional shell and solid models were used to investigate the onset of localization that precedes failure. In both models, the calculated pressure-deformation responses were found to be in reasonable agreement with the measured ones. The solid element model was shown to better capture the localization and its evolution. The corresponding pressure maximum was shown to be imperfection sensitive.

Table of Contents

Chapter 1: Introduction 1
1.1: Objectives of Present Study 2
Chapter 2: Design and Fabrication of Bulge Tester 4
2.1: Design of Bulge Tester 4
2.2: Pressurization System 6
2.3: DIC Setup 7
Chapter 3: Numerical Modeling 11
3.1: Axisymmetric Model 11
3.2: Shell Element Model 13
3.3: Solid Element Model 15
Chapter 4: Experimental Results 19
4.1: Formulation 19
4.2: Tensile Tests 21
4.3: Bulge Tests 22
4.4: Comparison of Measaured and Predicted Responses 26
Chapter 5: Summary and Conclusions 28
Figures 30
Appendix A 86
Appendix B 90
References 91
Vita 93

Chapter 1: INTRODUCTION

It has been a long-term objective of the mechanics and materials community to find ways to extend material responses to larger strains (e.g., Bridgeman, 1944). Tensile tests on sheet metal are limited due to the complex instabilities that take place, while efforts to extract the material response from the necked region are rather complicated (e.g., see recent work by Tardif and Kyriakides, 2012). It has long been noticed that equi-biaxial stretching of a sheet can delay the onset of necking, thus enabling establishment of the material response to significantly larger strain levels. A relatively simple method for developing an equi-biaxial state of stress is through a *bulge test*. This test, first developed in the mid-1940s, involves a sheet placed in a die with a (usually) circular opening. It is clamped in place and inflated with hydraulic pressure. In this thesis a bulge testing apparatus was designed, fabricated, calibrated and used to measure the stress-strain response of an aluminum sheet metal and establish its onset of failure.

Hill [1950] developed a finite deformation axisymmetric analysis of the inflation of a circular diaphragm. He assumed a true stress-strain response to establish a criterion for expected pressure maximum which was associated with the onset of localization and failure. The same instability was further studied by Swift [1952]. Mellor [1956] developed a custom bulge tester and used it to establish a stress-strain response for several materials. He measured strains by drawing concentric circles in ink and analyzing their deformed shape. He reported that the stress-strain response assumed by Hill was only applicable to a half-hard aluminum alloy (see also analysis by Chakrabarty and Alexander [1970] using Tresca's yield function).

At these early stages of testing, loading was suspended periodically to take local measurements of strain and the shape of the specimen, as in Ranta-Eskola [1979].

However, care needed to be taken, as Mellor showed the effects of creep on bulging when internal pressures were maintained over time. The interruptions were eliminated by adopting a spherometer to measure the local radius of the apex of the bulge coupled with an extensometer mounted in the same device (Young *et al.*, 1981). Both were electrically operated providing for a continuous monitoring of the shape and strain. With these innovations, the bulge test became a rather standard test for measuring the material response and to some degree prevalent anisotropies to larger strain levels.

More recently, with the advent of more advanced diagnostic techniques, extraction of the material response from bulge tests became simpler and this expanded its use. Dziallach *et al*. [2007] and Rana *et al*. [2010] used two noncontact, perpendicular laser lines to obtain shape data, and a dot grid was placed on the surface to collect local strains. Yanaga *et al.* [2012] used local strain gages to measure the strain and a spherometer to establish the apex radius. More recently, digital image correlation (DIC) has been used to obtain strain fields, as in Koc *et al.* [2010] where the shape of the apex was monitored photographically. Lazarescu *et al.* [2012] appear to have used the DIC system to evaluate both the strains as well as the radius of the apex.

1.1 Objectives of Present Study

The objective of this work is to design and fabricate a custom bulge testing facility capable of testing sheet metal to failure. Chapter 2 describes the design and fabrication of the bulge tester. Bulging is performed by the application of hydraulic pressure using a custom pressurization system. A commercially available digital image correlation system is to be utilized to allow for a completely noncontact and accurate data acquisition process. Relevant parameters, including the local strains and radius of curvature, will be extracted from the DIC software to calculate the equivalent stress-true

plastic strain response to be compared to tensile test responses. The measured responses are compared with corresponding ones from uniaxial tension data in Chapter 4. The bulging is simulated numerically using several levels of finite element modeling in Chapter 3. The results are compared with the measured responses. The thesis finishes with conclusions and recommendations to future users of the facility.

Chapter 2: DESIGN AND FABRICATION OF BULGE TESTER

A bulge tester is a widely used testing facility for applying a nearly equi-biaxial state of stress to a thin plate. This chapter describes a bulge tester designed and fabricated for the purposes of this study. The design of the tester itself is influenced by a similar facility reported in Yanaga *et al*. [2012]. The facility is designed to test circular metal plates with a six-inch diameter bulging section. The main components of the tester are a base plate, clamping ring, and closing plate, which are shown in Figure 2.1. Because this is a research testing facility, the system is clamped together with bolts for simplicity.

2.1 Design of the Bulge Tester

The system was designed using axisymmetric finite element models developed in ABAQUS. In the design used, the plate is clamped using a draw-bead machined into the base plate. In particular, the detailed design of the draw-bead and the corresponding recess groove in the clamping ring were determined from these models. Details of the numerical modeling appear in Chapter 3. Figure 2.2a shows the initial configuration of the setup. The first step in the simulation is the clamping process, and this is performed by prescribing a displacement to the clamping ring in the y-direction. This displacement presses the plate between the draw-bead and recess groove, thus sealing it in the process (see Figure 2.3). The extent of clamping was chosen so as to minimize both the slipping of the plate during pressurization and the strains around the clamped section. Both of these problem parameters were also influenced by the shapes of the draw-bead and recess groove. The draw-bead shape was fixed as shown in Figure 2.4 and the width, radii (R_o and R_i), and position of the recess groove relative to the bead were varied. Once

clamped, the specimen is pressurized by prescribing a fluid flux that increases the volume of the cavity. The deformed, pressurized configuration is shown in Figure 2.2b.

Figure 2.3 shows expanded views of the draw-bead zone of the FE model. The strains on the inside and top of the draw-bead were of particular interest, and therefore the inner and outer radii of the recess groove were analyzed in detail. Figure 2.3a shows the undeformed configuration of this zone, Figure 2.3b shows the same zone after clamping, and Figure 2.3c shows the zone after full pressurization. Two areas, identified as A and B in the figures, experience relatively high strains. The effect of the dimensions of the recess groove's radii, R_o and R_i, and the clamping displacement, Δ, on the local strains at these points are illustrated in the results shown in Figures 2.5. The figures show the evolution of the strains during the incremental loading process which is divided into two steps: clamping and pressurization. R_o, R_i, and Δ are varied in the figures. In these variations, the strain at zone A remains relatively constant. Thus, the objective was to minimize the strain at zone B while simultaneously minimizing slipping of the edge of the plate. Figure 2.5b shows that as the fillet radius increases, the strain decreases, but the specimen must be clamped further down to complete the seal and prevent slip. Thus, a nonsymmetric design utilizing a larger inner groove radius (0.175 in) to help minimize the strain at zone B and a smaller outer groove radius (0.125 in) to ensure proper sealing was selected.

The mechanical parts of the bulge tester are drawn in detail in Appendix A. The base plate shown in Figure 2.6a and in the drawing in Figure A.1a is 1.25 in thick with a diameter of 13 in machined out of 4140 steel. A 9-inch depression, 0.400 in deep, is machined into the plate in order to receive the circular test specimen. A draw-bead with the dimensions shown in Figure A.1b protrudes from the base of the depression for the purpose of clamping the specimen. The draw-bead has a diameter of 7.72 in and a height

of 0.131 in. An inlet and outlet are machined into the bottom of the plate to apply and relieve hydraulic pressure.

The disk specimen is clamped in place with the clamping ring as shown in Figure 2.6b (see detailed drawing in Figure A.2). The ring has a 6 in diameter central hole to accommodate the bulging of the disk. A 0.315 in radius fillet allows for a smooth transition from the clamped to bulged sections. A recess groove that mates with the draw-bead is machined in the ring as shown in the expanded view of Figure A.2. The recess groove is offset a few thousandths of an inch towards the center to ensure sealing occurs on the outside of the draw-bead.

The facility is closed and clamped with the closing plate shown in Figure 2.6c (see detailed drawing in Figure A.3). It also has a 6 in diameter opening to accommodate the bulging. It is placed above the ring, and clamping is completed using eight ¾ in bolts that thread into the base plate (see Figure 2.1).

The facility is closed with a protective transparent cover as shown in Figure 2.7. The top cover is made of acrylic and is 0.210 in thick. Its perimeter is reinforced with a half inch square acrylic bar. It rests on four PVC tubes 6 in long. Threaded rods pass through the cover and tubes and are secured with nuts on each end. Four 0.171 in thick acrylic plates are hung around the perimeter of the top cover thus enclosing the facility.

2.2 Pressurization System

The bulge testing facility is pressurized using a custom servohydraulic pressurization system shown in Figure 2.8. It consists of a pressure booster with a capacity of 59 in^3. The booster operates on standard 3,000 psi pressure that is available in the lab, and it multiplies the pressure so that the facility has a maximum capacity of 10,000 psi. The booster operates as a closed loop system using an MTS 407 controller. It

can run either in “pressure” or “volume” control. The pressure is monitored with a pressure transducer and the volume with an LVDT as shown schematically in Figure 2.9. The transducers are operated through a DC and AC conditioner, respectively, that are part of the controller. Each was calibrated to 10 V at full scale (see calibration curves in Appendix B).

2.3 DIC System

3D Digital image correlation (DIC) is used for deformation analysis throughout the experiment. To track the deformation, a random pattern is applied to the area of interest, commonly performed by spraying white and black paint onto the surface. Photographs are taken throughout the experiment and DIC software is used to analyze, calculate, and document the deformation of the bulge (ARAMIS 2011).

The DIC setup used for this specific experiment is a 3D ARAMIS 5M adjustable base model consisting of a sensor with two cameras, 50 mm lenses, adjustable stand, two LEDs for specimen lighting, PC, ARAMIS application software, and calibration objects. For the bulge test, ABAQUS simulations indicate a depth of field of at least 50 mm is required. This makes the 3D system essential to the experimental procedure because of its ability to easily accommodate large out-of-plane deformations and retain focus. This feature allows the cameras to be stationary throughout the duration of the experiment which is vital for monitoring the developing curvature of the bulging specimen.

The specimen is cleaned with acetone and measurements of the thickness are made with a micrometer. The pattern is applied by first adding a layer of white spray paint to the surface over a six inch diameter circle centered on the specimen. Black paint is then sprayed to produce a random pattern that is approximately balanced between white and black as shown in Figure 2.10. The specimen is painted as close to the time of

the experiment as possible to avoid drying and chipping. Once the specimen has been prepared, the cameras are set up to capture the photographs. The ARAMIS user manual advises that an approximate location of the camera be established first, and fine adjustments are later performed to achieve the optimal setup. The Sensor Configuration Examples (Adjustable Base) from the ARAMIS help documents provide the approximate aperture setting, measuring distance, and measuring volume needed to continue the setup which are defined in Figure 2.11. Depth of field is identified as the limiting dimension for this test, and the smallest configuration satisfying the 50 mm requirement is chosen to ensure optimal resolution. This configuration corresponds to a depth of field of 70 mm and a measuring volume of 80x65 mm and can be seen in the 7^{th} row of Figure 2.12.

Once the cameras have been set up according to the sensor configuration manual, adjustments are made to the slider distance and focus. The calibration object (Figure 2.13) is placed in the center of the calibrated volume (Figure 2.11) and the cameras are configured such that the laser is aligned with the crosshairs seen in the ARAMIS camera view. The aperture is opened to decrease the depth of field and each lens is focused. The writing on the calibration object is used as a focusing reference. After optimal focus is achieved, the aperture is closed to the value specified in the sensor configuration manual that satisfies the required depth of field.

Lighting throughout the experimental process must be consistent, and the two LEDs and polarizing lenses are adjusted until lighting between both the left and right cameras is approximately equivalent. To check the intensity of light, the "false color" view is chosen in ARAMIS. Optimal lighting is defined as a blue-purple color and overexposure red-yellow. Due to the specimen moving closer to the lights and cameras as it bulges, the initial lighting is set to the lower end of the optimal spectrum.

After camera setup and adjustment is complete, the cameras are calibrated using the GOM/CP 20/ MV 90x72 mm calibration object (Figure 2.13). Prompted by the ARAMIS software (Figure 2.14), the calibration process is carried out by taking a sequence of 13 photos of the calibration object at different angles and locations in the calibrated volume. Once the final calibration photo is taken, a dialog box appears providing calibration details including a calibration deviation value, which is a measure in pixels of the approximate error.

To analyze the deformation history of a bulge test, ARAMIS monitors the specimen through the images by means of various square or rectangular image details called facets (ARAMIS, 2011). Figure 2.15 shows an example of 15x15 pixel facets with 2 pixels of overlap (*step size* equal to 13 pixels). The evolution of these facets throughout the experiment provides data points for deformation analysis. Using photogrammetric methods, the 2D coordinates of a facet, observed from the left camera and the 2D coordinates of the same facet, observed from the right camera, lead to a common 3D coordinate (ARAMIS, 2011). This out-of-plane displacement data found by the 3D system is essential for the calculation of the curvature of the specimen.

For the bulge test a size and step of 25 pixels and 15 pixels, respectively, are typically selected. To begin analysis of the test, a start point is chosen which defines the location of the first facet to be calculated. Once the start point is accepted for all stages, the project is computed and analyzed. For the bulge test, the quantities of interest are the local major and minor strains, pressure, and radius of curvature of the apex. The local strains and radius of curvature are calculated using the ARAMIS software. Specifically, the radius of curvature is obtained by creating a best fit sphere from the data points within approximately a 0.75-1.0 in radius of the apex of the bulge. The system accepts external inputs, one of which was connected to the output of the pressure transducer (via the MTS

DC conditioner). This variable is stored synchronously with the DIC images. The recorded data are later exported from ARAMIS into a MATLAB script that calculates various quantities that will be discussed in Chapter 4.

Chapter 3: NUMERICAL MODELING

The bulge test experimental setup was first modeled to be axisymmetric. This 2D model was used to guide the design of the draw-bead and recess groove and to predict the maximum pressure in experiments. The bulging process is subsequently modeled using fully 3D finite elements in order to estimate the process of localization that leads to failure. This is performed first with shell elements and subsequently with solid elements. The three models are described in detail in this chapter.

3.1 Axisymmetric Model

The axisymmetric model developed, shown in Figure 2.2a, consists of four components: the clamping ring with recess groove, the specimen, the base plate with draw-bead, and a fluid-filled cavity. Dimensions of the clamping ring and base plate are given in Section 2.1. The clamping ring and base plate are modeled as analytical rigid bodies and the plate is modeled with 2780 solid, axisymmetric, continuum stress/displacement, 4-node, reduced integration elements (CAX4R). Five elements are used through the 0.040 in thickness and 556 along the 4.45 in length (see Figures 2.2 and 3.1). A fluid cavity is created between the specimen and base plate with 1018 axisymmetric, 2-node, fluid elements (FAX2). The density of the fluid was set equal to the density of the hydraulic oil used in the experiments, which is 0.0316 lb/in^3.

The plate is modeled as a finitely deforming J_2 elastic-plastic material with isotropic hardening. The constitutive model is calibrated using stress-strain data from a tension test from the plate tested (see Fig. 3.2). This response was extrapolated (linearly) and used in the initial parametric study performed for the purposes of designing the facility. Following the first successful bulge test, a more accurate response was extracted

from the experiment that is shown in Figure 3.3. The extracted response was used to preform most of the calculations that follow. The basic parameters of this material response are given in Table 3.1.

Table 3.1 Main geometric and material parameters of the base case

Mat.	r_o in	t in	E Msi	ν	σ_o ksi
Al-2024-T3/S	3.0	0.040	10.4	0.3	50.3

Contact between the rigid surfaces and aluminum plate is modeled as finite sliding with a Coulomb friction coefficient of 0.4.

The calculated pressure-volume response is shown in Figure 3.4. A set of seven deformed configurations of the meridian are depicted in Figure 3.5. They correspond to the seven points marked on the response with solid bullets. The first step in the simulation involves clamping the plate by prescribing an incremental downward displacement for the clamping ring. During this process, the pressure in the cavity is prescribed to be zero, which implies that the volume of fluid in the cavity is reduced. The amount of clamping is one of the variables of the problem that decides the extent of straining that the draw-bead area undergoes. In this case, the displacement of the ring is 0.090 in. The pressurization is performed by increasing incrementally the volume of the fluid cavity by prescribing a fluid flux. Typically, it takes approximately 170 volume increments to reach the pressure maximum.

The response is initially relatively stiff, becoming incrementally softer after approximately a pressure of 1200 psi. In this case, a pressure maximum of 1375 psi was attained at a volume of 35.3 in^3. The bulge grows in a parabolic shape shown in Figure 3.5. It is interesting that at the pressure maximum, the apex reaches a height of about $0.7r_o$ (measured from the base plate). At $r = r_o$, the specimen has a small change in height throughout the experiment due to the presence of the fillet of the clamping ring.

Figures 3.6a and 3.6b show respectively the logarithmic strains and true stresses in the r and θ directions at the pressure maximum. Both coincide at the apex illustrating the equi-biaxial state that develops there. The strains are reduced nearly equally as the radial position increases. They deviate slightly from each other close to the edge due to the presence of the circular fillet on the clamping ring (see Figure 3.1c). The stresses also decrease with radial position but τ_θ remains larger than τ_r throughout the domain.

The evolution of the stress and strains as the specimen bulges is detailed in Figure 3.7. While the true plastic equivalent strain increases substantially over the last 200 psi of pressurization, the effect on the true equivalent stress is more subtle. From 1190 psi to 1375 psi, the increase in strain is 155% while the increase in stress is 20.2%. At the limit load, the true plastic equivalent strain and true equivalent stress are a maximum and reach 70.8% and 105.7 ksi, respectively. It is worth noting that the small change in both the stresses and strains at $r = r_o$ is due to the present of the fillet. The equivalent stress and strain in the deformed cross-section at the pressure maximum are also illustrated in Figure 3.8 using color contours.

3.2 Shell Element Model

A shell element model of the bulge test was also developed in order to investigate the onset of localization that precedes failure. The FE mesh developed is shown in Figures 3.9a and 3.9b, while and isometric view of the model can be seen in Figure 3.10. The model consists of the specimen, clamping ring, and fluid. The specimen has a 7.70 in diameter and is composed of 10240 four-noded, reduced integration, shell elements (S4R). A one inch square section in the center of the plate is assigned a refined mesh in order to facilitate localization. It is assigned 40 x 40 elements and is shown in Figure 3.11. The ring once again has an opening of $r_o = 3.0$ in, but for simplicity the recess

groove is not included. Instead, the specimen perimeter is fixed at the approximate location of the draw-bead. Below the specimen is a 0.131 in tall fluid cavity that is composed of 20640 four-noded fluid elements (F3D4). The height of the fluid cavity was chosen to match the height of the draw-bead and therefore it is nearly equivalent to the fluid cavity parameters in the axisymmetric model.

The plate is again modeled as a finitely deforming J_2 elastic-plastic material with isotropic hardening. Contact between the rigid surfaces and aluminum plate is modeled using finite sliding with a coefficient of Coulomb friction of 0.4. The loading was again accomplished by incrementally prescribing a fluid flux.

The bulging response of the plate was repeated using this shell element model and the calculated pressure-volume response is shown in Figure 3.12. The corresponding response from the axisymmetric model is also included for comparison, and the shell model results are shifted such that both responses start at the same value. The two responses are quite similar with the shell model developing a pressure maximum of 1365 psi at 34.83 in^3. These values compare quite favorably with the corresponding values for the axisymmetric model. The small difference can be attributed in part to the absence of the draw-bead, which causes the fluid cavity in the shell model to have slightly different geometry.

The failure of the specimen is modeled by incorporating a small geometric imperfection (similar to Korkolis and Kyriakides, 2008) in the central part of the plate as shown in Figure 3.11. The imperfection has a length of 1.0 in, a width of 0.06 in, and a thickness reduction of 5% (i.e., a local thickness of 0.038 in). The model is again pressurized under volume control and the resultant pressure-volume response is shown in Figure 3.13. The imperfection model follows a very similar response until it reaches a pressure of about 1300 psi when deformation begins to localize. A zoomed in plot of the

P-υ response of the imperfection model is shown in Figure 3.14, and a set of deformed images of the imperfection neighborhood are depicted in Figure 3.15. They correspond to points on the response marked with the numbered bullets. The response develops a pressure maximum at 1319 psi which can be assumed to represent the burst pressure in an actual bulge test. Images ① and ② are before the pressure maximum and image ③ captures the model at the maximum load. Deformation in the imperfection is seen to progressively increase up to the pressure maximum. At the pressure maximum, the thickness at the imperfection is approximately $0.431\,t_o$ while in the adjacent elements $0.645\,t_o$. Beyond it, in images ④,⑤, and ⑥, deformation is localized taking the form of a widening of the imperfect strip. Figure 3.16 shows the thickness across the imperfection at the center of the model. The localization is in the form of uniform thinning, an artifact of the shell elements adopted. Despite this, the results demonstrate that "burst" pressure exhibits some imperfection sensitivity.

The results of the shell model described above were confirmed by using an alternate incremental loading scheme based on Riks' Method. Here a uniform pressure was applied to the bottom of the plate. For better convergence, the Coulomb friction was set to a value of 0. All other problem parameters were kept the same. Figure 3.17 shows the calculated pressure-apex height response. Included for comparison is the corresponding response from the volume controlled calculation. The pressure maximum occurs at approximately the same height at a pressure of 1325 psi which compares favorably with the 1319 psi yielded by the volume controlled model.

3.3 Solid Element Model

A solid element model was also developed to further investigate the onset of localization. Top and cross-sectional views of the mesh are shown in Figures 3.18a and

3.18b, and an isometric view is shown in 3.19. It consists of the specimen and clamping ring. The specimen has a diameter of 7.70 in and is composed of 29098 eight-noded, reduced integration, linear solid elements (C3D8R). There are five elements through the thickness, and four elements through the imperfection thickness. The specimen's diameter is approximately equal to the diameter of the draw-bead, and a fixed boundary condition is enforced around the outer edge. The ring once again has an opening of $r_o = 3.0$ in. An one inch square section in the center of the plate is assigned a refined mesh in order to facilitate localization (see Figure 3.20). The plate is modeled as a finitely deforming J_2 elastic-plastic material with isotropic hardening. Contact between the rigid surfaces and aluminum plate is modeled as finite sliding, and for better convergence, the Coulomb friction was set at zero.

In order to facilitate the expected localization at the apex, an imperfection is introduced in the central part of the plate as shown in Figure 3.20. The imperfection has a length of 1.0 in, a width of 0.06 in, and a thickness reduction of 5% (i.e., a local thickness of 0.038 in). The length is composed of 40 elements, and the width and thickness are each composed of four elements. The bottom of the imperfection is flush with the remaining mesh, and the 5% thickness reduction is taken entirely from the top of the plate.

The model is again pressurized by applying a uniform pressure to the bottom of the plate using the Riks' Method, and the pressure-height response is shown in Figure 3.21. A pressure maximum of 1312 psi is reached at a height of 1.91 in. A zoomed in plot of the $P - H$ response is shown in Figure 3.22, and a set of deformed images of the imperfection neighborhood are depicted in Figure 3.23. They correspond to the points on the response marked with the numbered bullets. Figure 3.24 in turn shows the thickness across the imperfection at the center of the model at the same times ($t(T)/t_o$). The

response develops a pressure maximum at 1312 psi and can be assumed to represent the burst pressure in an actual bulge test. Images ① and ② are before the pressure maximum and image ③ captures the model at the maximum load. The thickness in the neighborhood of the apex has been significantly reduced. At the pressure maximum the wall thickness outside the groove is about $0.62t_o$, while at the center of the imperfection it is down to $0.357t_o$ (Figure 3.24). Beyond the pressure maximum, in images ④,⑤, and ⑥, deformation localizes further in the groove imperfection as illustrated in Figures 3.23 and 3.24. This takes the form of both widening as well as thinning. The localized deformation here is to be contrasted with the corresponding results in Figures 3.15 and 3.16 from the shell element model, where the widening was accentuated and the groove wall thickness was constant. The solid elements allow for changes in thickness across the element, and therefore the details of the imperfection are more complete but still appear to be rough and discretized by the mesh.

For completeness, Figure 3.25 compares the $P-H$ responses from two solid models. Drawn with a solid line is the previously discussed case while the dashed line represents the same general model, but here, the imperfection is represented with two elements across the width instead of a four. The two responses are identical until the neighborhood of the pressure maximum is reached. The model with the four element groove reaches a pressure maximum of 1312 psi at height of 1.91 in while the pressure maximum for the two element model is delayed, reaching a pressure of 1328 psi at H = 2.03 in. The responses beyond the pressure maximum also differ, with the four element model exhibiting a sharper localization and capturing the groove deformation more accurately.

A comparison of the pressure-height response of the shell and solid models is shown in Figure 3.26. The solid model experiences a slightly different response at the

beginning of pressurization, but overall the response is quite similar to the shell model. The solid model reaches a pressure maximum of 1312 psi at a height of 1.91 in, and the shell model attains a pressure maximum of 1319 psi at 1.81 in.

Chapter 4: EXPERIMENTAL RESULTS

One of the advantages of bulge testing is that it prolongs the onset of instability and failure, thereby allowing a more complete material model to be obtained as compared to a simple tensile test. This chapter presents the results of several bulging experiments performed on Al-2024-T3 plates. This includes the strains measured at the apex and the measured radius of the apex, both using DIC, and the calculation of the stresses. A simple formulation is then used to obtain the material stress-strain response up to failure.

4.1 Formulation

Let ε_1 and ε_2 be the principal strains of a bulge test. Thus, the true principal strains in the 1 and 2 directions are given by

$$e_{1,2} = \ln(1+\varepsilon_{1,2})\,. \tag{1}$$

An approximation of the thickness of the plate is next calculated to obtain an initial "guess" for the stress and therefore an initial value for the plastic strains. The thickness approximation is calculated as

$$t_a = t_o \exp(-(e_1 + e_2))\,, \tag{2}$$

where t_o is the initial thickness of the plate. An approximation of the true principal stresses are then found by

$$\tau_1 = \tau_2 \approx \frac{\mathrm{Pr}}{2t_a}\,, \tag{3}$$

where P is the internal pressure and r is the average radius of curvature of the bulged specimen. Next, the true plastic strains can be calculated as

$$e^p_{1,2} = e_{1,2} - \frac{\tau_1(1-\nu)}{E}\,, \tag{4}$$

where E is the Young's modulus calculated from a tensile test. Invoking incompressibility,

$$e_3^p = -(e_1^p + e_2^p). \tag{5}$$

The plastic strain in the 3-direction can be found. Using 3D Hooke's Law and obtaining e_3^e, the true strain thickness and thus the thickness of the plate can be found by

$$e_3 = e_3^p - e_3^e \tag{6a}$$

$$e_3^e = -\frac{2\nu\tau_1}{E} \tag{6b}$$

$$t_p = t_o \exp(e_3). \tag{6c}$$

An iterative method is then used such that t_a and t_p converge. Let us call this new value of the converged thickness t. Then, the final stresses are calculated as

$$\tau_1 = \tau_2 = \frac{\mathrm{Pr}}{2t}. \tag{7}$$

The equivalent stresses and strains are then found

$$\tau_e = \sqrt{\frac{3}{2} s_{ij} s_{ij}} = \frac{\mathrm{Pr}}{2t} \tag{8a}$$

$$e_e^p = \sqrt{\frac{2}{3} e_{ij}^p e_{ij}^p}, \tag{8b}$$

where s_{ij} and e_{ij}^p are the deviatoric stress components and true plastic strains, respectively.

Tensile tests were also performed to obtain initial material responses and to later compare to bulge test results. The stress and strain values obtained from the tests were then converted into true stress and true plastic strain by the following:

$$\tau = \sigma(1+\varepsilon) \tag{9a}$$

$$e = \ln(1+\varepsilon) \tag{9b}$$

$$e^p = e - \frac{\tau}{E}. \tag{9c}$$

Due to the uniaxial stress state of the tensile test, these values are also the "equivalent" stress and strain values.

4.2 Tensile Tests

Two different plates of Al-2024-T3 were used in the experiments, both of approximately 0.040 in thickness. They are identified as Al-2024-T3/S and Al-2024-T3/UT. Tensile tests were performed for each plate in the rolling as well as the transverse direction. Table 4.1 shows the basic parameters of these responses: E is the Young's modulus, ν Poisson's ratio, and σ_o the stress at a 0.2% strain offset.

Table 4.1 Main geometric and material parameters of the Al2024-T3 tensile tests

Direction	w in	t in	E Msi	ν	σ_o ksi
S-Rolling	0.3513	0.0401	10.39	0.3	51.5
S-Transverse	0.3515	0.0398	10.47	0.3	43.9
UT-Rolling	0.4373	0.0401	9.76	0.3	48.6
UT-Transverse	0.4362	0.0401	9.70	0.3	45.6

Figure 4.1 shows the results of the Al-2024-T3/S tests. The tests were performed on dog-bone type specimens with the usual radius transition zones at each end. Strains were measured with two strain gages and an extensometer. Both directions had very similar responses, with the rolling direction having a slightly higher yield stress and a sharper transition to plastic deformation. Due to this difference, the yield stress is nearly 8 ksi higher. The rolling direction specimen reaches a stress maximum of 68.3 ksi at a strain of 17.9% and the transverse direction specimen reaches a stress maximum of 66.8 ksi at a strain of 18.8%.

The results of the Al-2024-T3/UT tests are shown in Figure 4.2. These tests had similar responses, with the rolling direction having a 3 ksi higher yield stress. However,

the transition to plastic deformation was smoother. These specimens were uniform strips and consequently failed at smaller strains. The rolling direction reached a stress maximum of 63.7 ksi at a strain of 12.9% and the transverse direction specimen reached a stress maximum of 62.7 ksi at a strain of 11.1%.

4.3 Bulge Tests

In this section, the results of four bulge tests are presented, one performed on the Al/2024-T3/S sheet, and three others performed on the Al-2024-T3/UT. In each case, the measured pressure-volume response and the extracted true stress-strain material response are reported. The main parameters of the four experiments appear in Table 4.2. The thickness and diameter of the discs tested are approximately 0.040 in and 8.980 in, respectively, in all cases.

Table 4.2 Main parameters of the bulge tests

Exp. No.	Plate No.	t in	$P_{\max}$ (psi)	$\tau_{e\max}$ (ksi)	$e^p_{e\max}$ (%)
BU8	S6	0.0401	1352	87.4	28.0
BU10	UT1	0.0401	1347	85.2	38.1
BU11	UT2	0.0401	1329	85.6	40.9
BU12	UT3	0.0401	1321	83.7	37.7

Experiment BU8

The pressure-volume response from test BU8/S6 can be seen in Figure 4.3. The initial value is nonzero due to the clamping that takes place before the beginning of the test, and the initial response is vertical because the manual pressurization unit was used to

apply pressure until a value of approximately 200 psi was attained. The response exhibits relatively linear behavior until about 1000 psi and then becomes progressively less stiff. The plate failed at a pressure of 1352 psi and a photograph of the bulged plate can be seen in Figure 4.4. In this experiment, failure was due to fracture at the inner edge of the draw-bead as identified in the figure. A number of wrinkles on the outer rim indicate that some slipping may have occurred which was probably responsible for this premature failure.

Several bulge tests that preceded this one exhibited similar characteristics, and after analysis it was determined there were two factors leading to this type of premature failure. First, previous clamping had not been uniform and therefore compression was uneven. To remedy this problem, three spacers were placed between the base plate and closing plate throughout the duration of clamping and pressurization. Second, it was determined the strains in this region were too high, and this led to an analysis and the change in the design of the clamping ring groove that was discussed in Section 2.1. After these changes were made, failure occurred in the middle of the specimen and these tests will be discussed later in this chapter.

Despite this premature failure, the bulge test had introduced significant deformations to the plate enabling the calculation of the material response to larger strains than those of the uniaxial tests. The extracted equivalent stress-true plastic equivalent strain response of a bulge test performed on the Al-2024-T3/S material is shown in Figure 4.5. It extends to a plastic strain of about 28%, which compares with about 16% for the tensile tests that are included in the figure for comparison. It is noteworthy that the small amount of anisotropy was neglected in the calculation of the material response for the bulge test. Specifically, the radius of curvature was obtained by creating a best fit sphere from the data points within approximately a 0.75-1.0 in radius of

the apex of the bulge, thus taking the average of the radii of curvature of the bulging section. Consequently, the bulge test response falls between the two tensile tests throughout their history.

Experiments BU10, BU11, BU12

Three bulge tests were performed using the Al/2024-T3/UT sheet. These were performed with the modified clamping ring geometry given in Figure A.2. For two of the three tests, in order to help initiate localization near the apex, a small imperfection was placed in the middle of the plate by carefully sanding the specimen in the rolling direction. For the first test (UT1), the imperfection was approximately 0.001 in thick over a strip about 0.75 in wide by 3.0 in long along the middle of the specimen. For the second test (UT2) the imperfection was approximately 0.0005 in extending over about the same area at the center of the circular plate specimen. The third specimen (UT3) was tested free of induced imperfections.

The pressure-volume responses of the three UT plate bulge tests can be seen in Figure 4.6. They follow very similar trajectories. Once again, the initial pressure is nonzero due to the clamping that takes place before the beginning of the test. Thus, the initial responses are vertical because the manual pressurization unit was used to apply an initial pressure of approximately 200 psi. The curves exhibit relatively linear behavior until approximately 900 psi and then begin a gradual decrease in stiffness. In all three cases, failure occurred in the neighborhood of the apex.

The first test (UT1) reached a pressure maximum of 1347 psi and the failed specimen can be seen in Figure 4.7. The specimen burst and failed down the middle of the plate in the transverse direction, allowing additional strain data to be extracted as compared to previous experiments where failure occurred at the draw-bead.

The second test (UT2) had a pressure maximum of 1329 psi, and Figure 4.8 shows the specimen after failure. The burst in this case is interesting as there are two perpendicular failures that occurred. Similar to UT1, the full fracture is in the transverse direction. The manufactured imperfection in the rolling direction most likely led to the transverse fracture seen on the left in the photograph.

The third test (UT3) did not have any imperfection, and a maximum pressure of 1321 psi was reached before failure. The burst specimen can be seen in Figure 4.9. In this case, the plate failed slightly off-center from the apex. In this case, photographs were taken every 0.5 seconds. Furthermore, we were able to zoom in and extract some information about the evolution of the strain field near the apex. Figure 4.10 shows four strain field images just before failure that correspond to the bulleted numbers on the expanded pressure-volume response in Figure 4.11. The images show a higher strain developing at the apex approximately one inch in diameter. As deformation grows, two zones of higher strain appear oriented approximately along the rolling direction. Image ① shows the early stages of localization, and this takes place at a pressure of 1274 psi. Images ② at a pressure of 1298 psi and ③ at 1313 psi show the appearance and development of the two zones of higher strain with the two "islands" becoming more distinct. Image ④ is the last one captured before burst, corresponding to a pressure of 1321 psi. The final failure of the plate occurred along the lower longitudinal "island" in image ④.

The equivalent stress-true plastic equivalent strain responses of bulge tests BU10, BU11, and BU12 are shown in Figures 4.12, 4.13, and 4.14, respectively. Included in each figure are the tensile test results for the rolling and transverse directions. It is worth pointing out that at the early stages of bulging, the radius of curvature of the apex is rather difficult to estimate. Despite this, the three bulge tests results tend to once again

stay in between the two tensile test results. The tensile test in the rolling direction reaches a strain of 11.4% before localization and the transverse direction test reaches a strain of 10.4%. The first bulge test (UT1) attains a strain of 38.1% before burst, which is more than three times larger than either of the tensile tests. Similarly, the second test (UT2) has a failure strain of 40.9%, nearly four times larger than the tensile tests. The third test (UT3) attains a failure strain of 37.7%.

4.4 Comparison of Measured and Predicted Responses

The numerical results discussed in Chapter 3 were calculated for the Al-2024-T3/S plates, and these results are compared to the pressure-volume response obtained from experiment BU8/S6 in Figure 4.15. The experimental response was shifted to the right such that volume and pressure values are initially equivalent to the numerical responses. The experimental response is somewhat less stiff than the numerical responses, but this is expected due to some of the assumptions that were made. The fluid is compressible, and the actual cavity is somewhat different than that of the model. It also includes the booster and hose, and the hose expands as pressure increases. Despite these assumptions and the specimen failing at the draw-bead, the pressure maximum and corresponding volume are quite similar. The bulge test reached a maximum pressure of 1352 psi at an adjusted volume of 32.2 in^3, while the axisymmetric and shell models had maximum pressures of 1375 psi and 1365 psi at volumes of 35.3 in^3 and 34.8 in^3, respectively.

The pressure-height response of experiment BU8/S6 is shown in Figure 4.16. Also included are the responses of the shell and solid model discussed in Sections 3.2 and 3.3. The bulge test response is once again translated to the right such that the initial values of pressure and height are equivalent to the numerical models. The pressure-height

response is quite similar to the numerical responses throughout most of the test. The bulge test begins to deviate from the numerical results at approximately 1000 psi as it maintains a stiffer response. A maximum pressure of 1352 psi at an adjusted height of 1.77 in is attained which are comparable to 1319 psi at 1.81 in for the shell model and 1312 psi at 1.91 in for the solid model.

Chapter 5: SUMMARY AND CONCLUSIONS

In this work a custom bulge testing apparatus was designed and fabricated with a six-inch circular opening to test thin aluminum plates under equi-biaxial tension. The device includes a base plate with draw-bead, clamping ring with recess groove, and closing plate. Clamping is achieved by compressing the specimen between the mating draw-bead and recess groove as in Yanaga *et al.* [2012].

The device is pressurized using a custom servohydraulic pressurization system with a pressure booster capacity of 10,000 psi and a maximum displaced volume of 59 in^3. The booster is operated as a closed loop system using an MTS 407 controller. The pressure is monitored with a pressure transducer and the volume with an LVDT. Pressurization was performed under volume control. The pressure and displaced volume are monitored via a data acquisition system.

The design of the draw-bead and groove was found to be crucial for a successful test. They were designed using an axisymmetric finite element model to minimize the induced strain in this neighborhood. A new clamping ring was designed that produced successful experiments once the optimum recess groove geometry was adopted. Three successful tests were performed that burst near the apex of the bulged specimens at strains nearly four times greater than the maximum strains obtained in corresponding tensile tests.

In the initial two tests on this material, small geometric imperfections were placed in the middle of the plates by carefully sanding the specimen in the rolling direction to help induce localization. Both of these plates failed in the transverse direction. The third plate had no induced imperfection and failed in the rolling direction but the failure was slightly off-center. A detailed analysis of the local strain using the DIC images revealed

two elongated zones of localized deformation straddling the apex. One of these was responsible for the failure.

Finite deformation isotropic plasticity was used to extract the true equivalent stress-strain responses from the plates tested. The results were compared to their corresponding uniaxial tensile tests. The bulge test results correlated well with the uniaxial results as they tended to fall between the rolling and transverse direction tensile results. The bulge tests results extended the stress-strain response to strain levels of the order of 40%. This compares with failure strains of the order of 10% for the tensile tests.

Three-dimensional shell and solid models were used to investigate the onset of localization that precedes failure. In both models, the calculated pressure-deformation responses were found to be in reasonable agreement with the measured ones. The solid element model was shown to better capture the localization and its evolution (in agreement with related works Giagmouris et al. [2010], and Tardif and Kyriakides [2012]). The corresponding pressure maximum was shown to be imperfection sensitive.

Future work with this bulge tester should include a more complete study of the localization and failure of the specimen. Later experiments produced some information about the evolution of the localized strain fields, but no model was developed to analyze this behavior more closely. Additionally, a further investigation of the behavior of anisotropic materials tested in biaxial tension should be included in both the numerical modeling and experimental calculations to obtain a more accurate material model. Although the best fit sphere of the bulged surface is a good approximation of the deformed specimen, the radii of curvature along orthogonal meridians of the plate are slightly different and should be further analyzed. Finally, it became clear that if the draw-bead geometry is fixed, the clamping ring groove plays an important role in the location of failure and consequently must be tailored to the specimen tested.

Figures

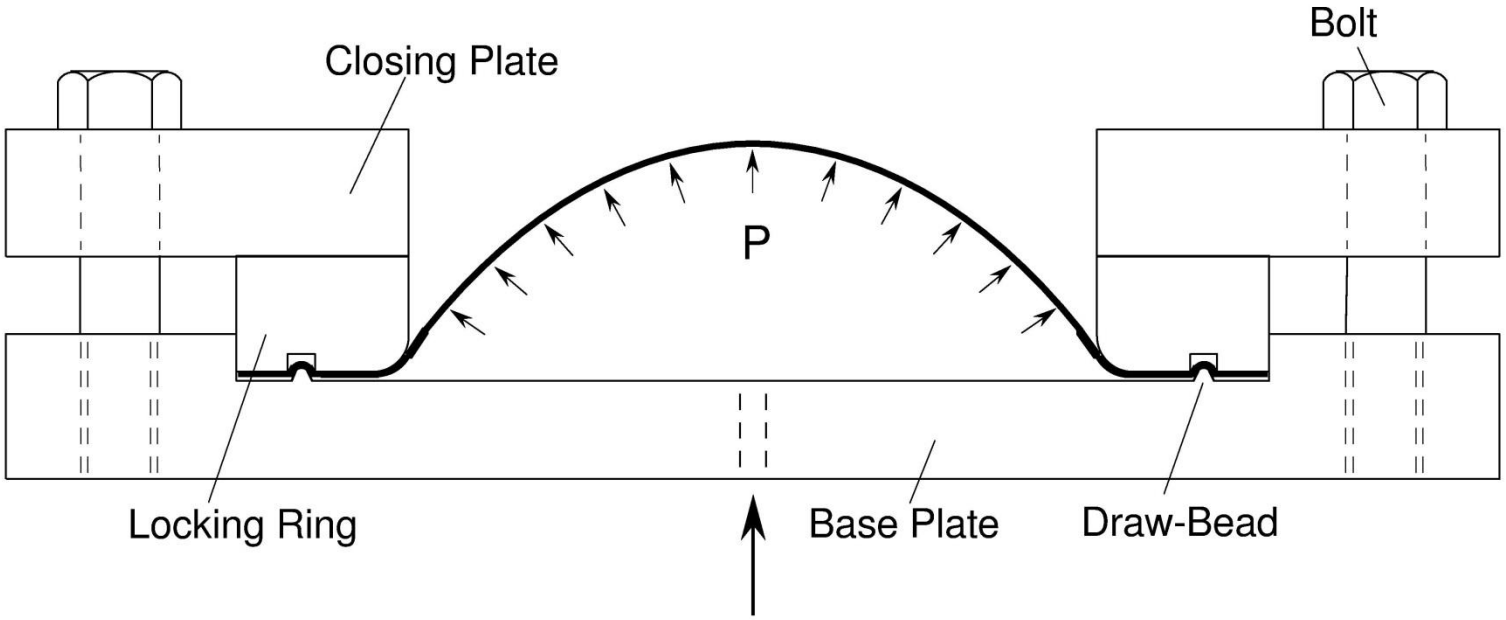

Figure 2.1 Schematic of bulge tester including base plate, clamping ring, and closing plate.

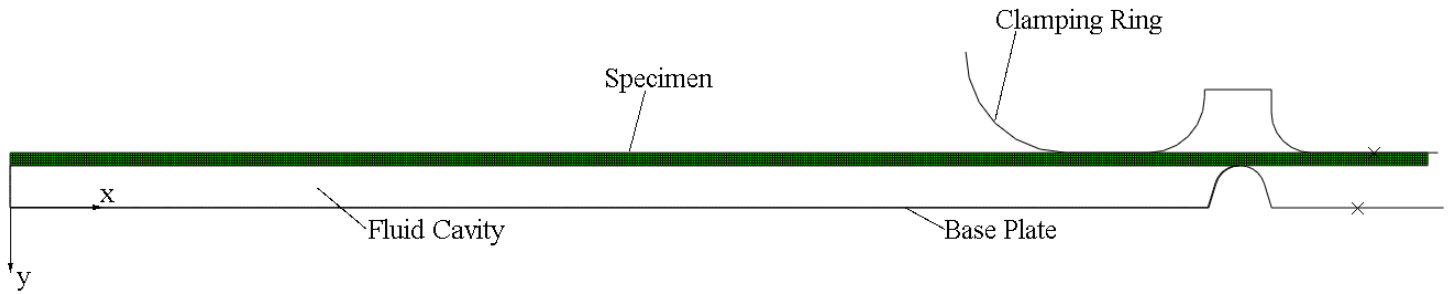

(a)

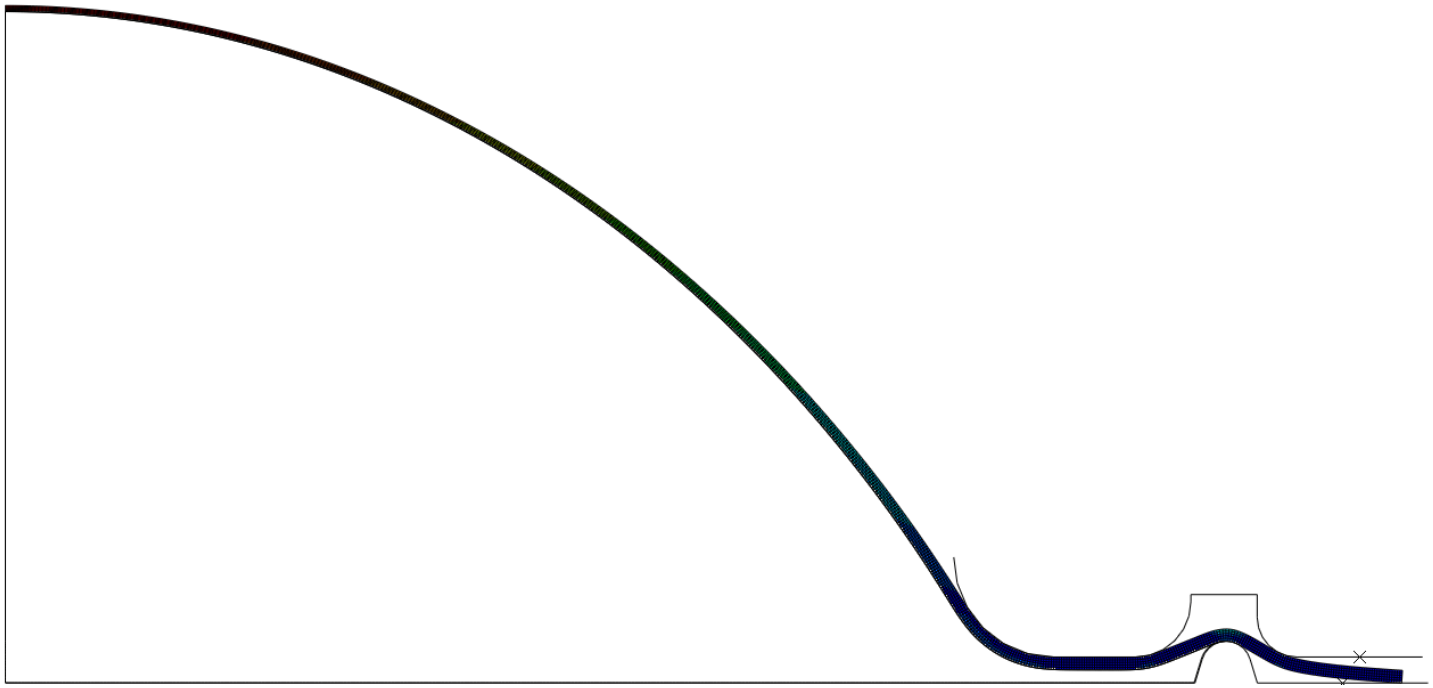

(b)

Figure 2.2 Original (a) and deformed (b) configurations of the axisymmetric model.

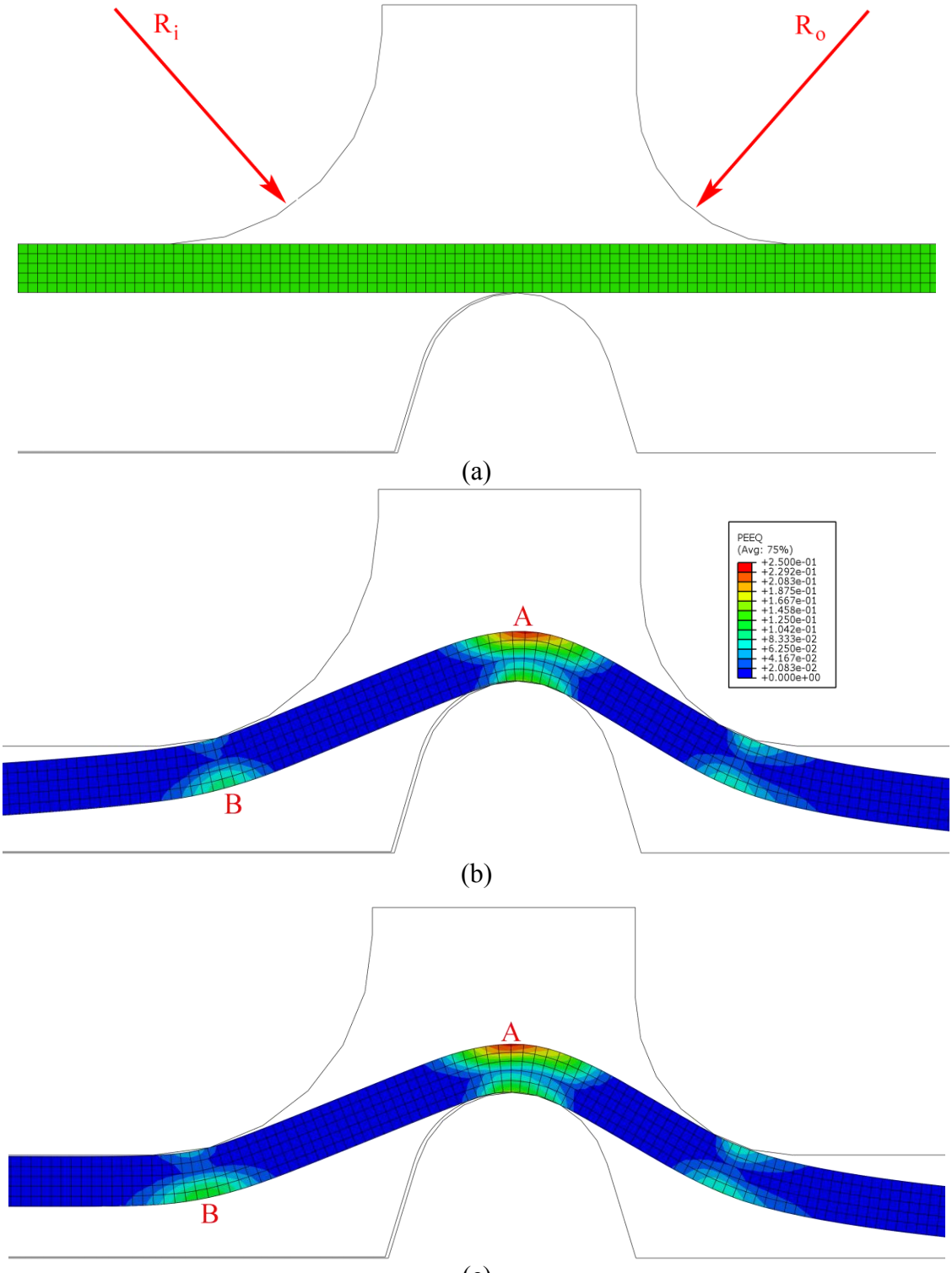

Figure 2.3 Strain contours around the draw-bead: (a) undeformed, (b) clamped, (c) pressurized.

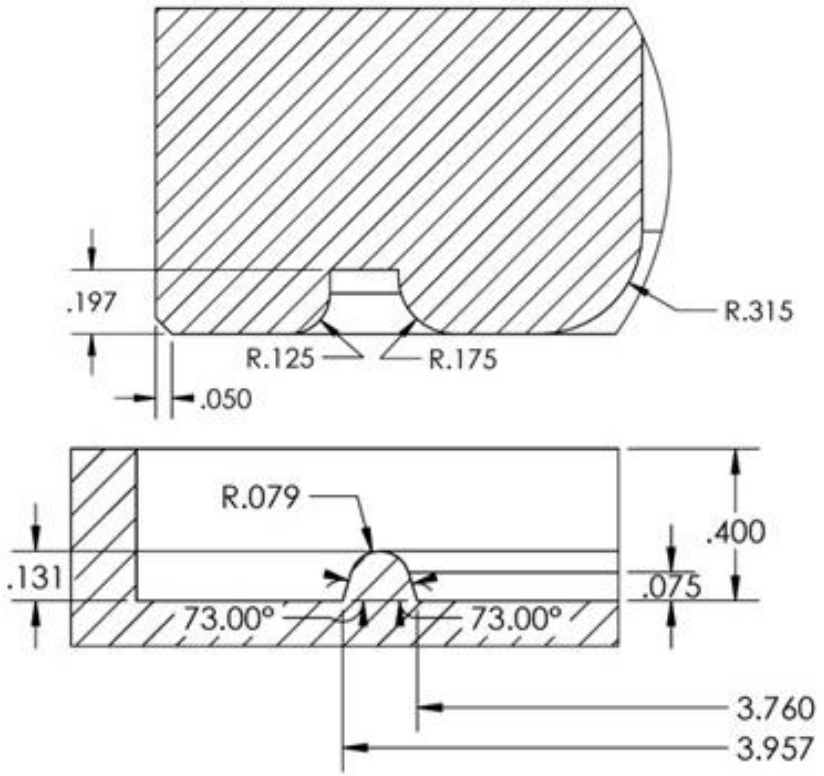

Figure 2.4 Geometric details of draw-bead and recess groove.

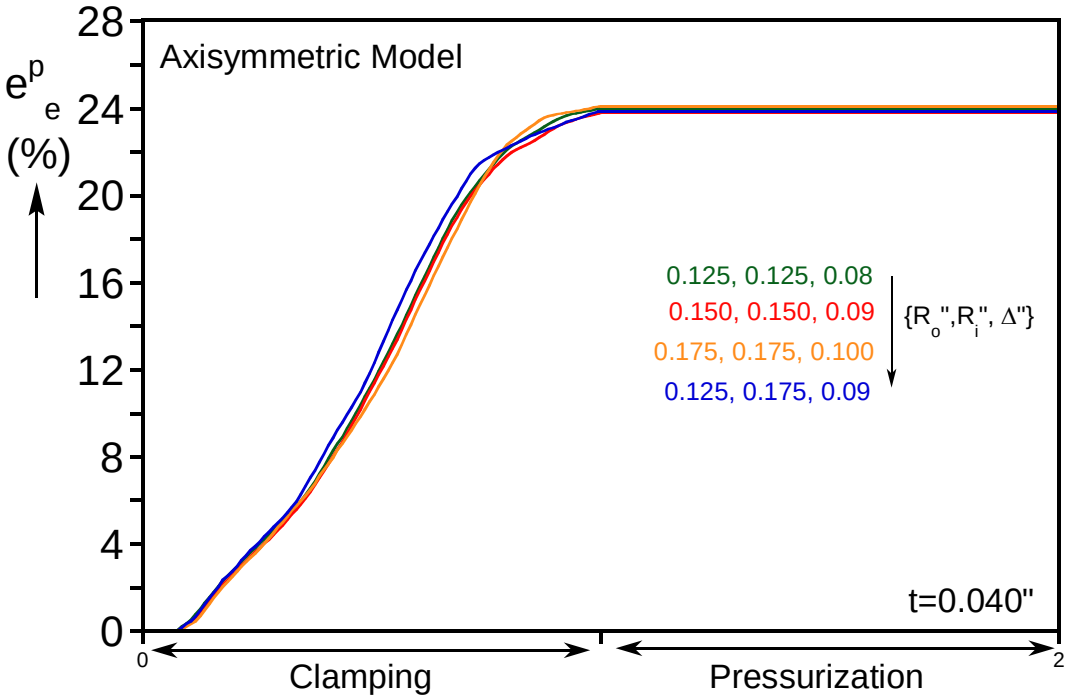

(a)

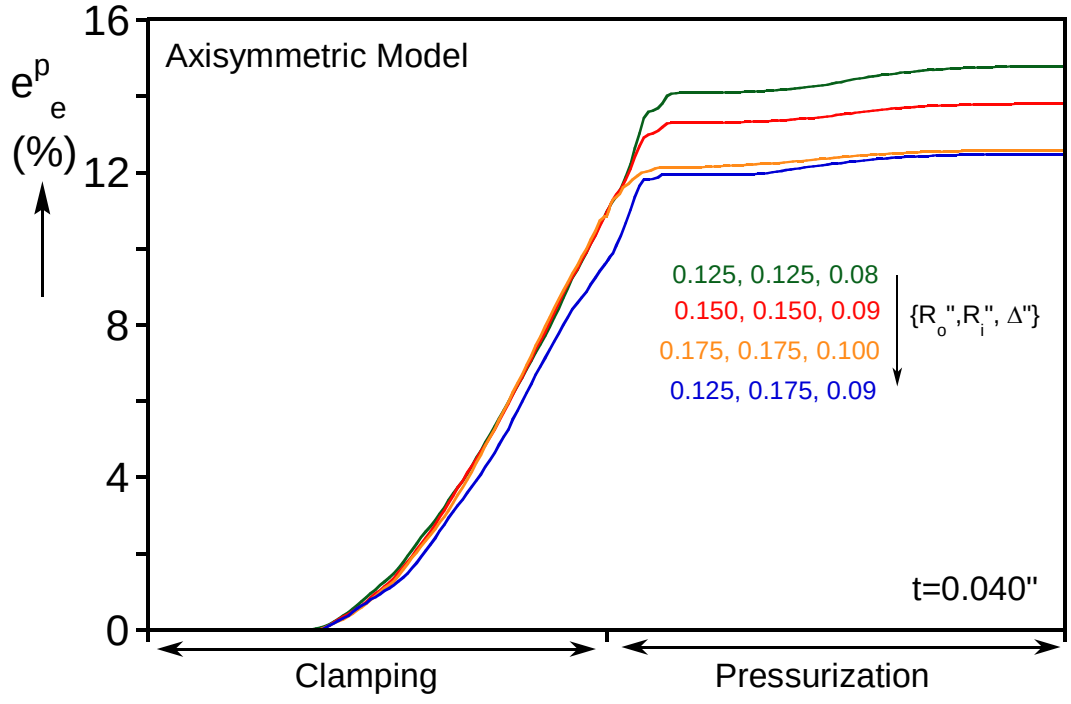

(b)

Figure 2.5 Strains at zones A and B.

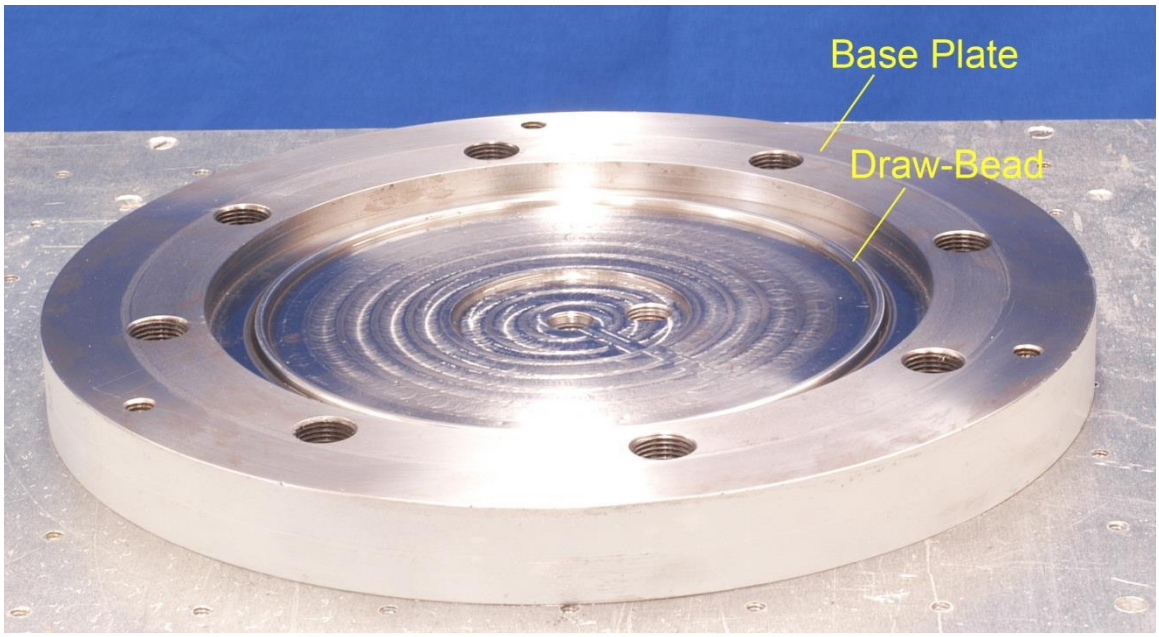

Figure 2.6a Bulge tester: base plate.

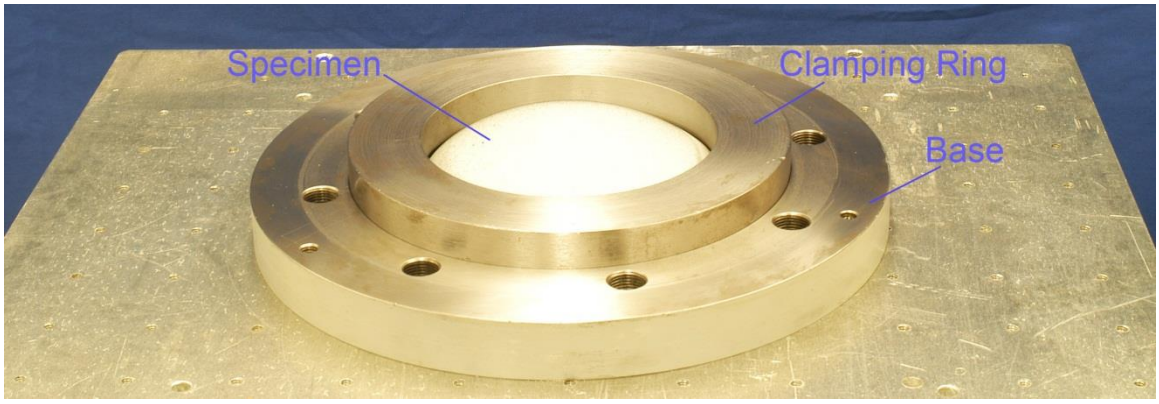

Figure 2.6b Bulge tester: clamping ring.

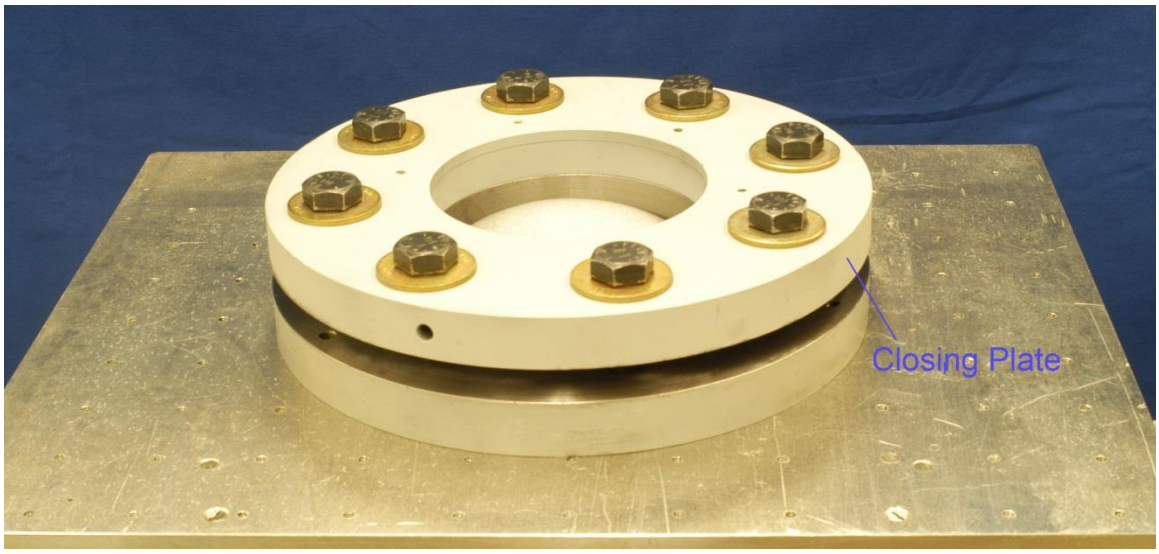

Figure 2.6c Bulge tester: closed.

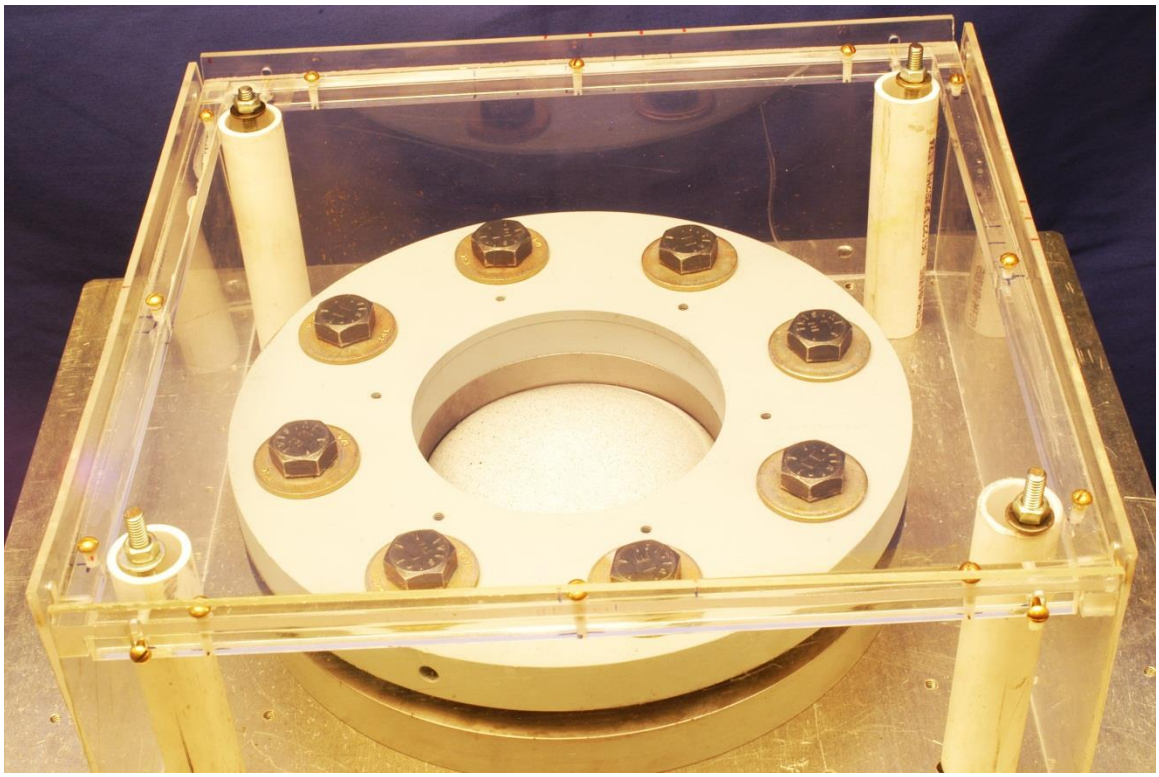
Figure 2.7 Bulge tester with protective cover.

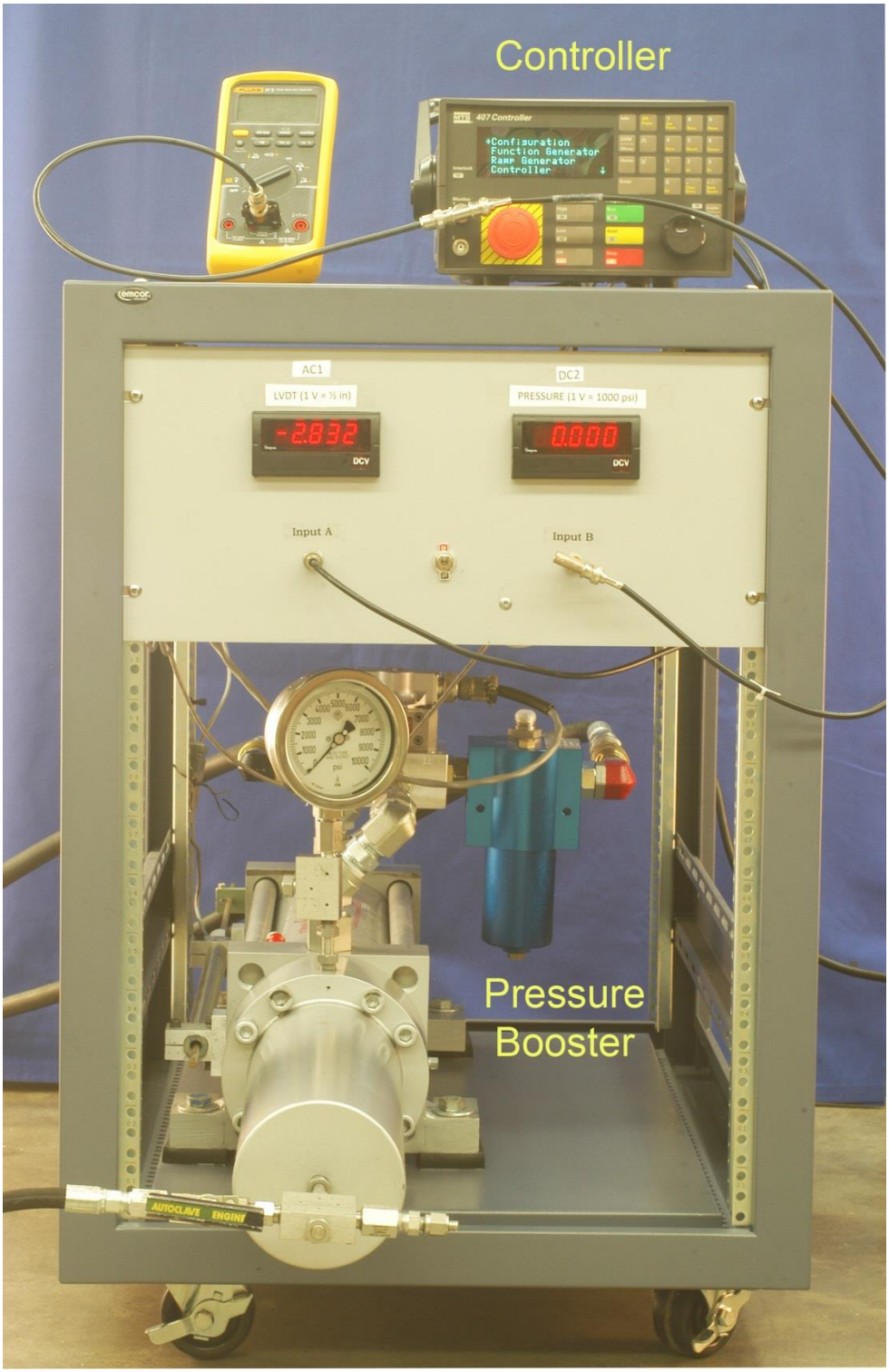

Figure 2.8 Pressurization system.

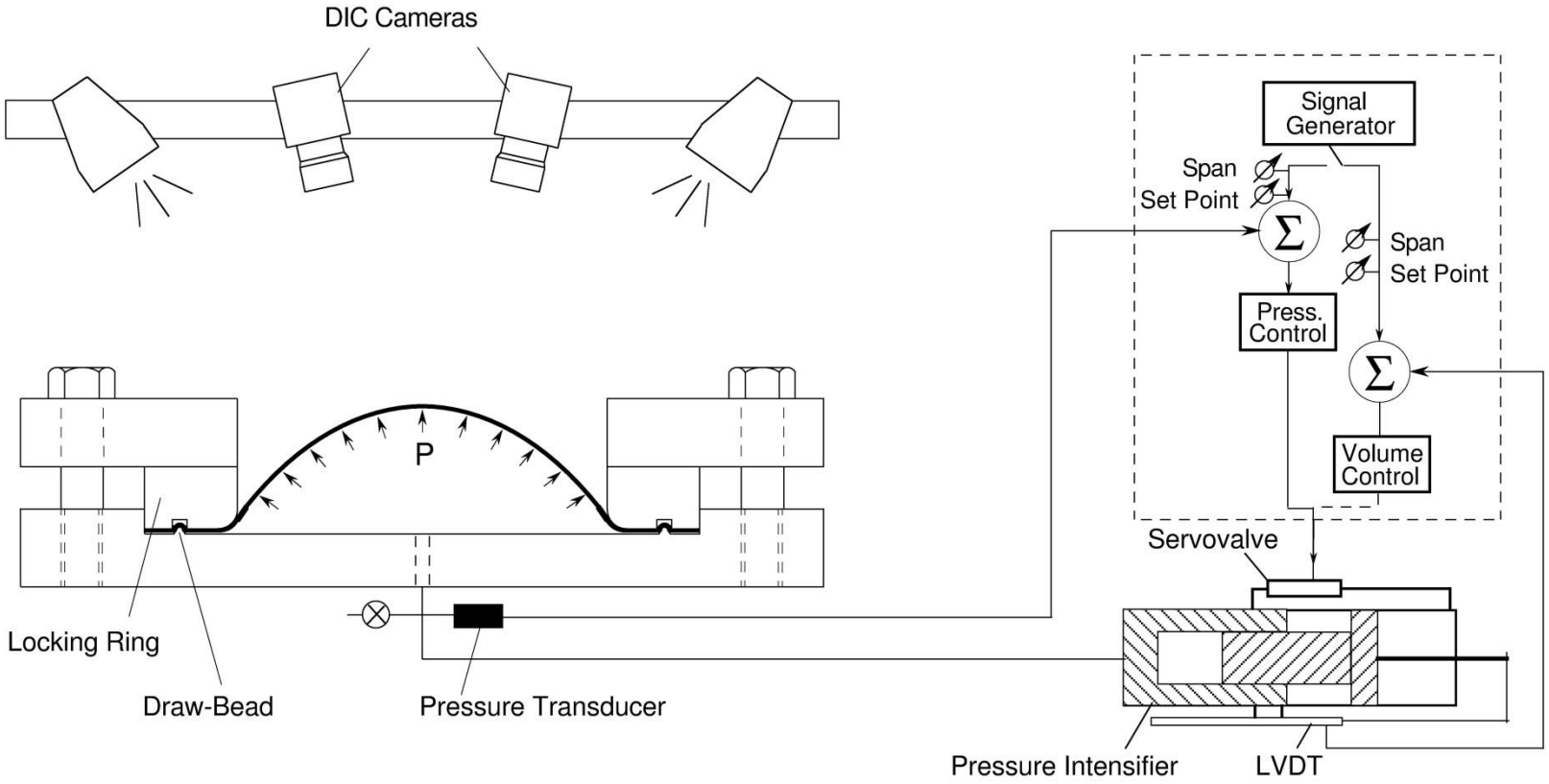

Figure 2.9 Schematic of experimental setup consisting of the bulge tester, the pressurization system, and the DIC cameras.

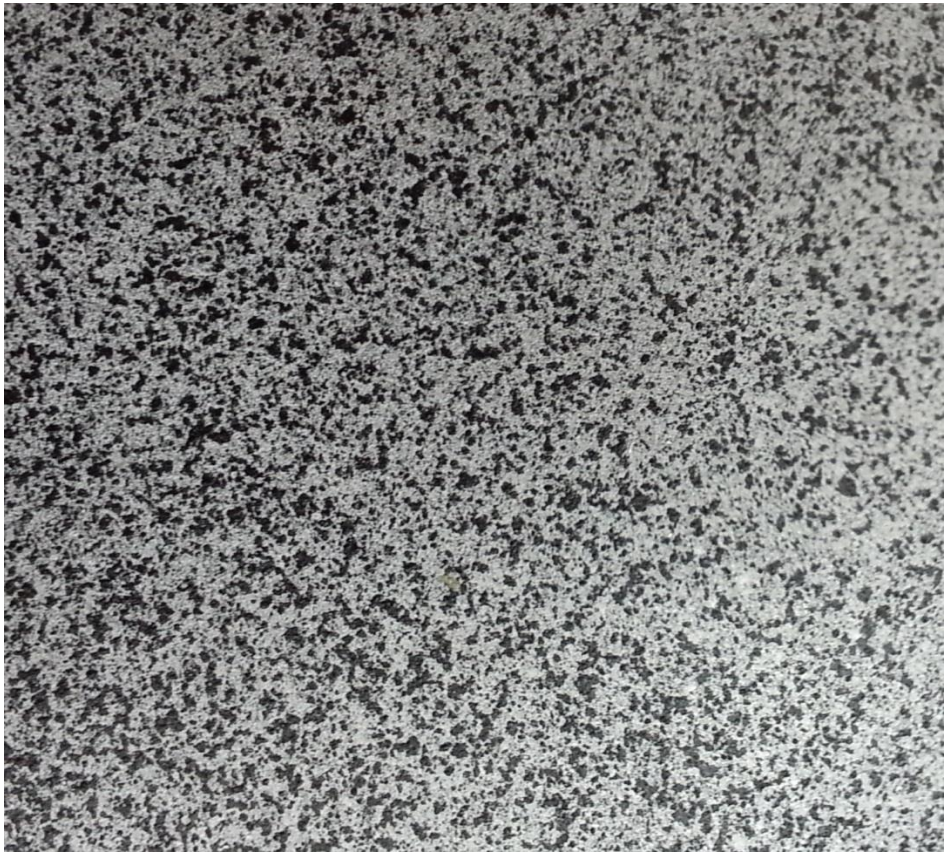

Figure 2.10 Pattern.

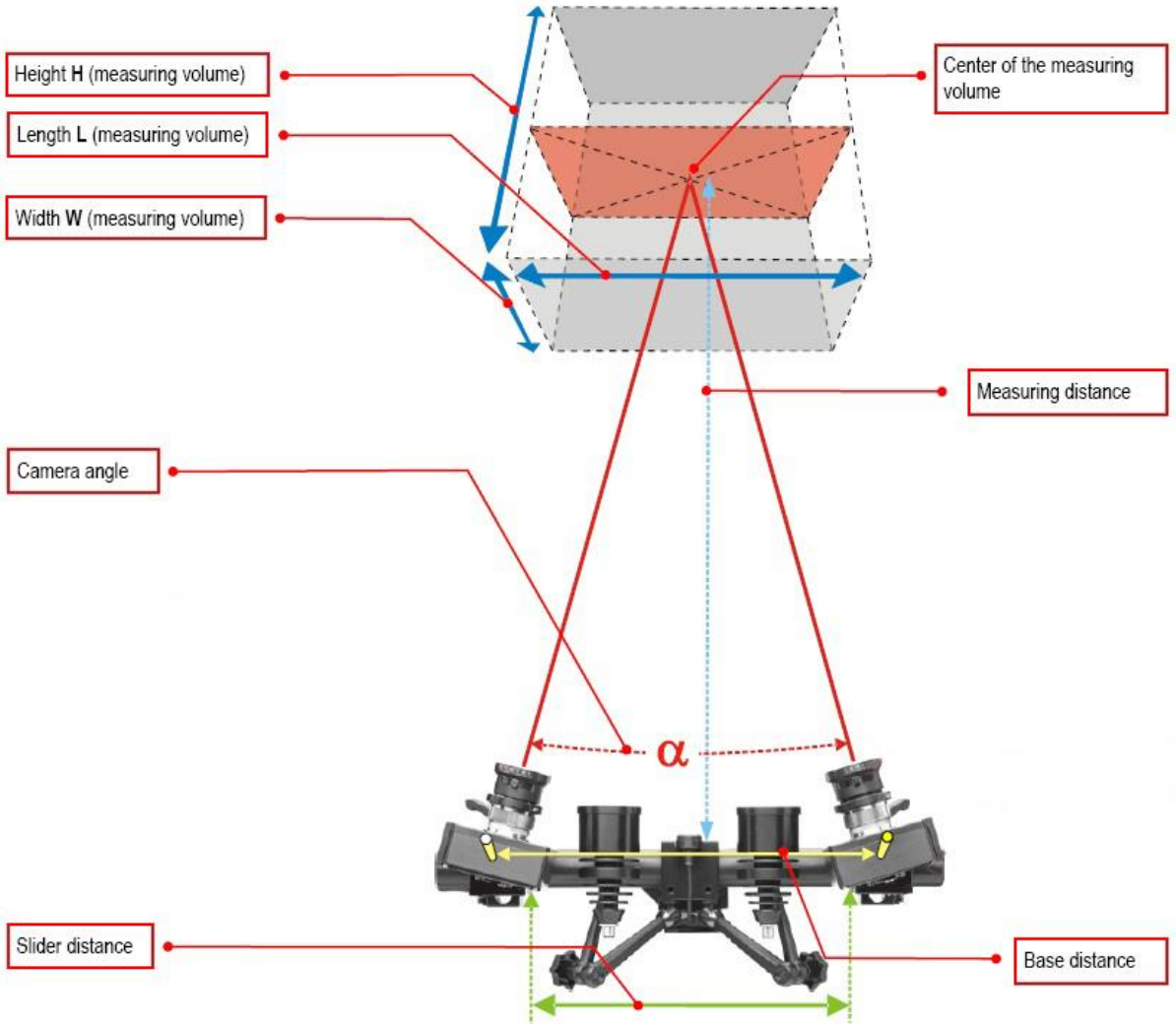

Figure 2.11 Definition of DIC setup variables.

3.6 50 mm Lens (ARAMIS 5M, 5M LT)

Sensor	Lens	Measuring volume [mmxmm]	Comment	Min. length camera support [mm]	Distance ring [mm]	Measuring distance [mm]	Slider distance [mm]	Camera angle [°]	Calibration Object	Aperture dependent depth of field [mm]									
										1,4	2	2,8	4	5,6	8	11	16	22	32
ARAMIS 5M	Titanar 50mm	**15 x 13**	---	500	20	**205**	MS	26	CQ 15x12	---	---	n.a.	n.a.	n.a.	**n.a.**	n.a.	0,9	---	---
		20 x 17	---	500	10	**230**	64	25	CQ 23x18	---	---	n.a.	n.a.	n.a.	**n.a.**	0,4	2,7	---	---
		25 x 21	---	500	10	**250**	74	25	CQ/CP20 30x24	---	---	n.a.	n.a.	n.a.	**n.a.**	1,4	4,5	---	---
		35 x 29	---	500	---	**310**	98	25	CQ/CP20 30x24	---	---	n.a.	n.a.	n.a.	**1,5**	5	11	---	---
		50 x 42	---	500	---	**395**	136	25	CQ/CP20 55x44	---	---	n.a.	n.a.	1,4	**6,8**	14	25	---	---
		65 x 55	---	500	---	**485**	176	25	CQ/CP20 55x44	---	---	n.a.	0,3	6,1	**15**	26	45	---	---
		80 x 65	---	500	---	**575**	216	25	CP20 90x72	---	---	n.a.	4,1	13	**26**	43	70	---	---
		100 x 85	---	500	---	**695**	270	25	CP20 90x72	---	---	1,2	11	25	**45**	70	>100	---	---
		125 x 100	---	500	---	**845**	336	25	CP20 90x72	---	---	8,3	24	45	**76**	120	>125	---	---
		150 x 130	---	800	---	**995**	402	25	CP20 175x140	---	---	18	40	70	**110**	>150	>150	---	---
		175 x 150	---	800	---	**1150**	472	25	CP20 175x140	---	---	31	61	100	**160**	>175	>175	---	---
		200 x 170	---	800	---	**1300**	540	25	CP20 250x200	---	---	46	85	140	**>200**	>200	>200	---	---
		250 x 210	---	800	---	**1600**	674	25	CP20 250x200	---	---	85	150	230	**>250**	>250	>250	---	---
		300 x 250	---	800	---	**1920**	688	21	CP20 350x280	---	---	150	230	>300	**>300**	>300	>300	---	---
		350 x 290	2)	1200 fixed	---	**2160**	---	31	CP20 350x280	---	---	170	290	>350	**>350**	>350	>350	---	---
		400 x 330	2)	1200 fixed	---	**2490**	---	27	CP20 350x280	---	---	260	>400	>400	**>400**	>400	>400	---	---
		500 x 420	2)	1200 fixed	---	**3140**	---	21	CC20 500x400	---	---	470	>500	>500	**>500**	>500	>500	---	---
		750 x 630	2)	1600 fixed	---	**4685**	---	19	CC20 1000x800	---	---	>750	>750	>750	**>750**	>750	>750	---	---

Legend

1) without laser pointer
2) For further information please refer to the user information Hardware for ARAMIS (Fixed Base).
MS Slider distance at Mech. Stop

--- Lens cannot be adjusted to the aperture value.
n.a. It is not possible to focus the complete measuring volume.
* Resolution limited by aperture.

Figure 2.12 Sensor configuration table.

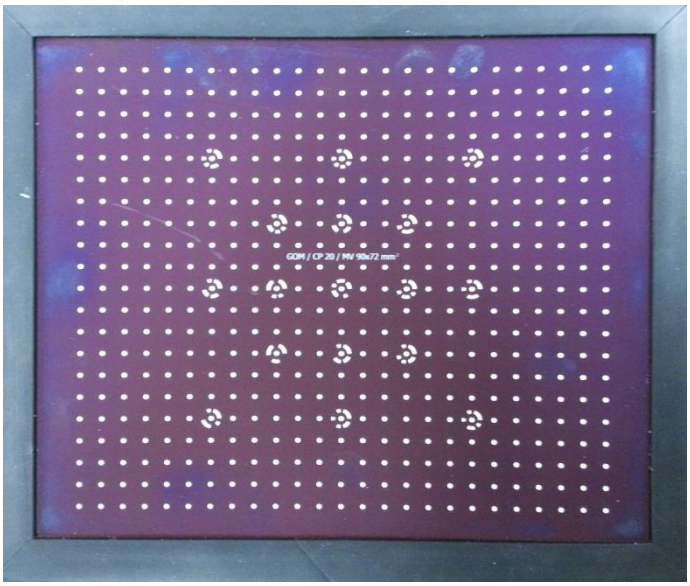

Figure 2.13 GOM / CP 20 / MV 90x72 mm calibration object.

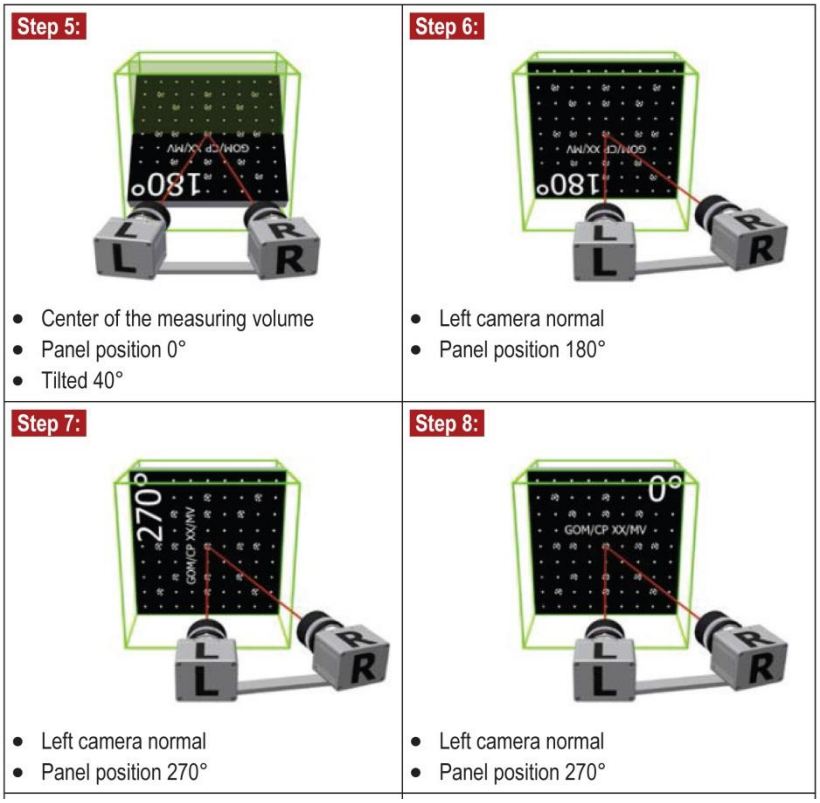

Figure 2.14 Examples of calibration procedure.

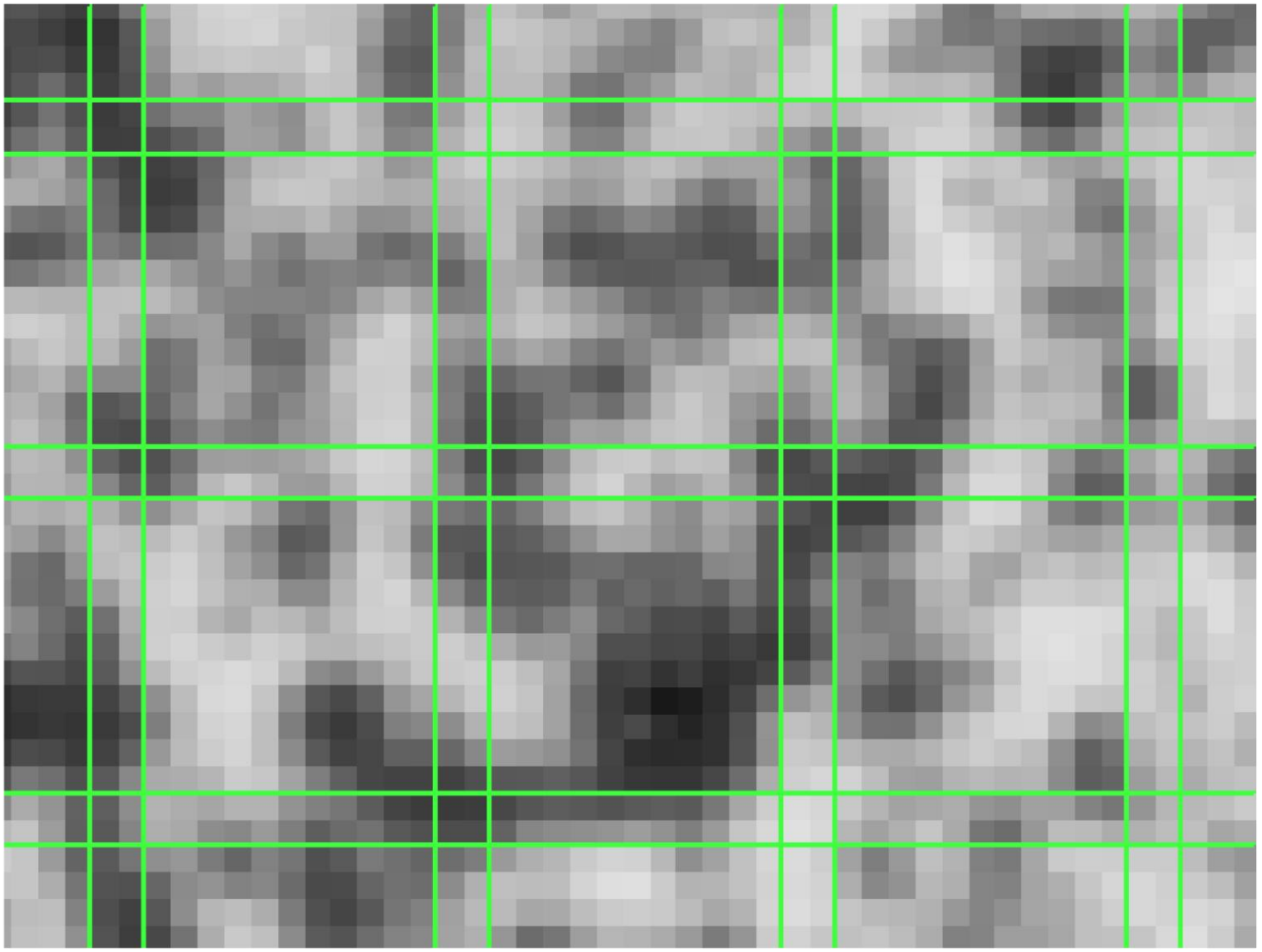

Figure 2.15 Facets with size 15x15 pixels and a step of 13 pixels (overlap of 2 pixels).

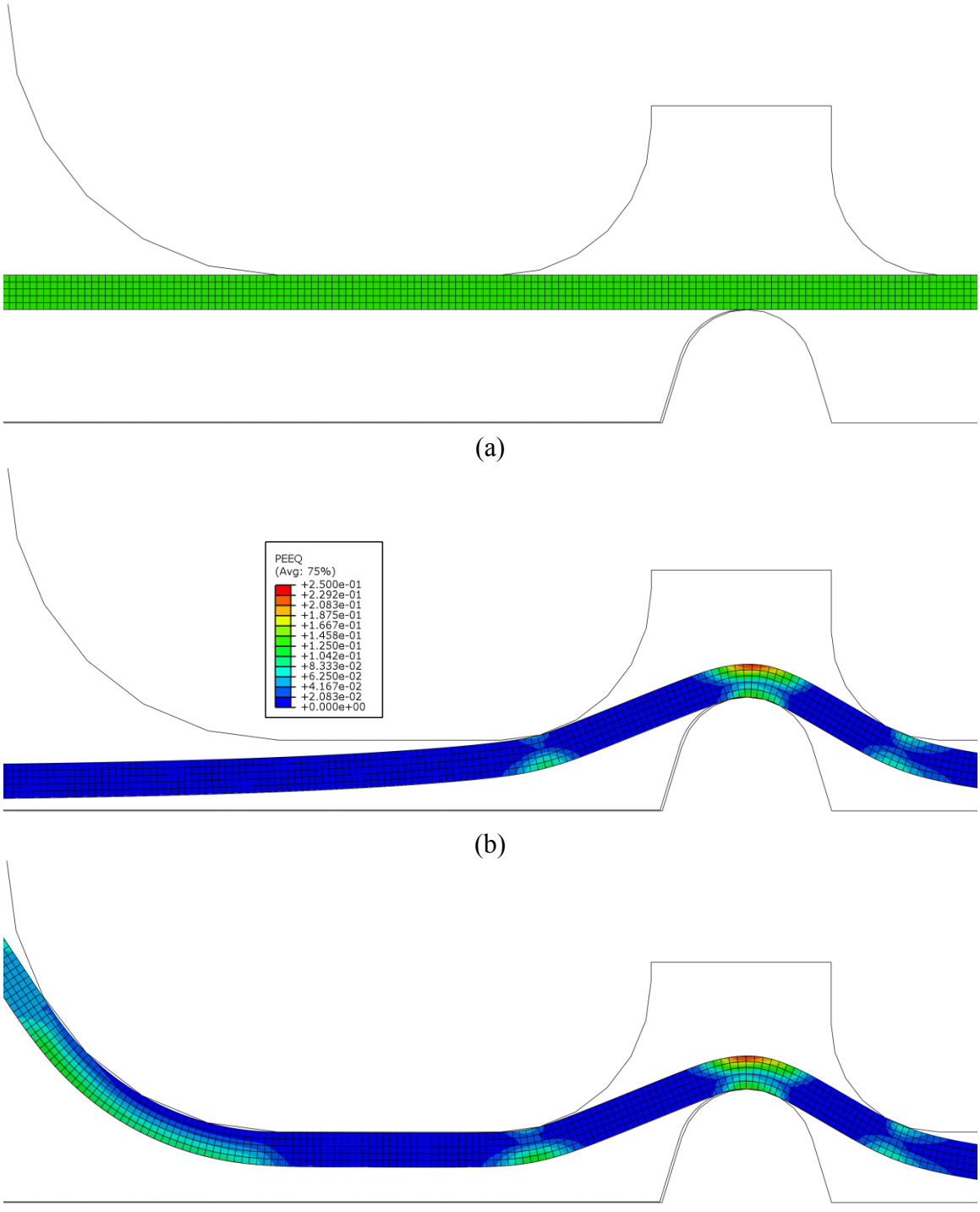

(a)

(b)

(c)

Figure 3.1 Undeformed, clamped, and pressurized configurations.

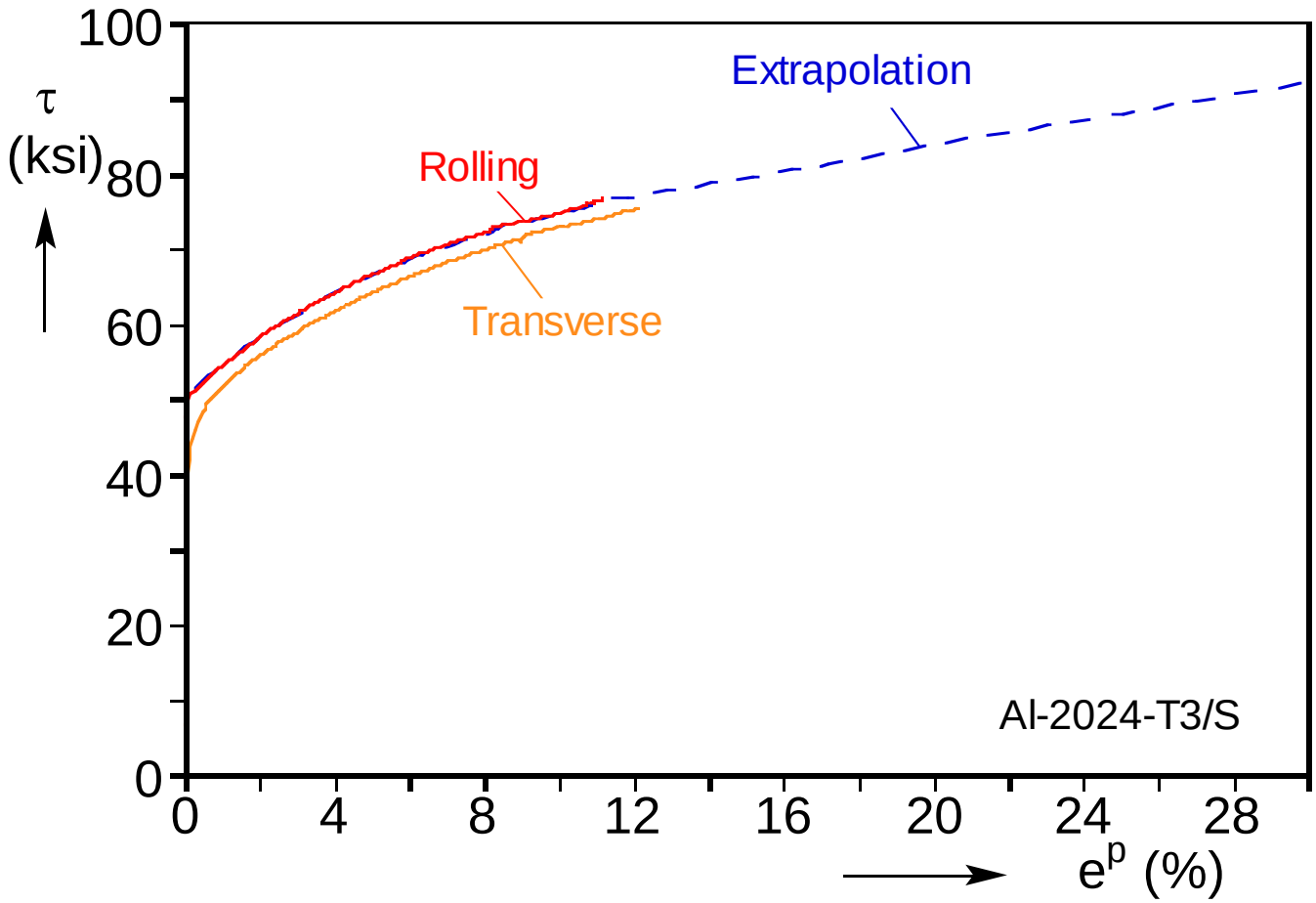

Figure 3.2 True stress-logarithmic strain measured in tension tests on plate specimens from rolling and transverse directions.

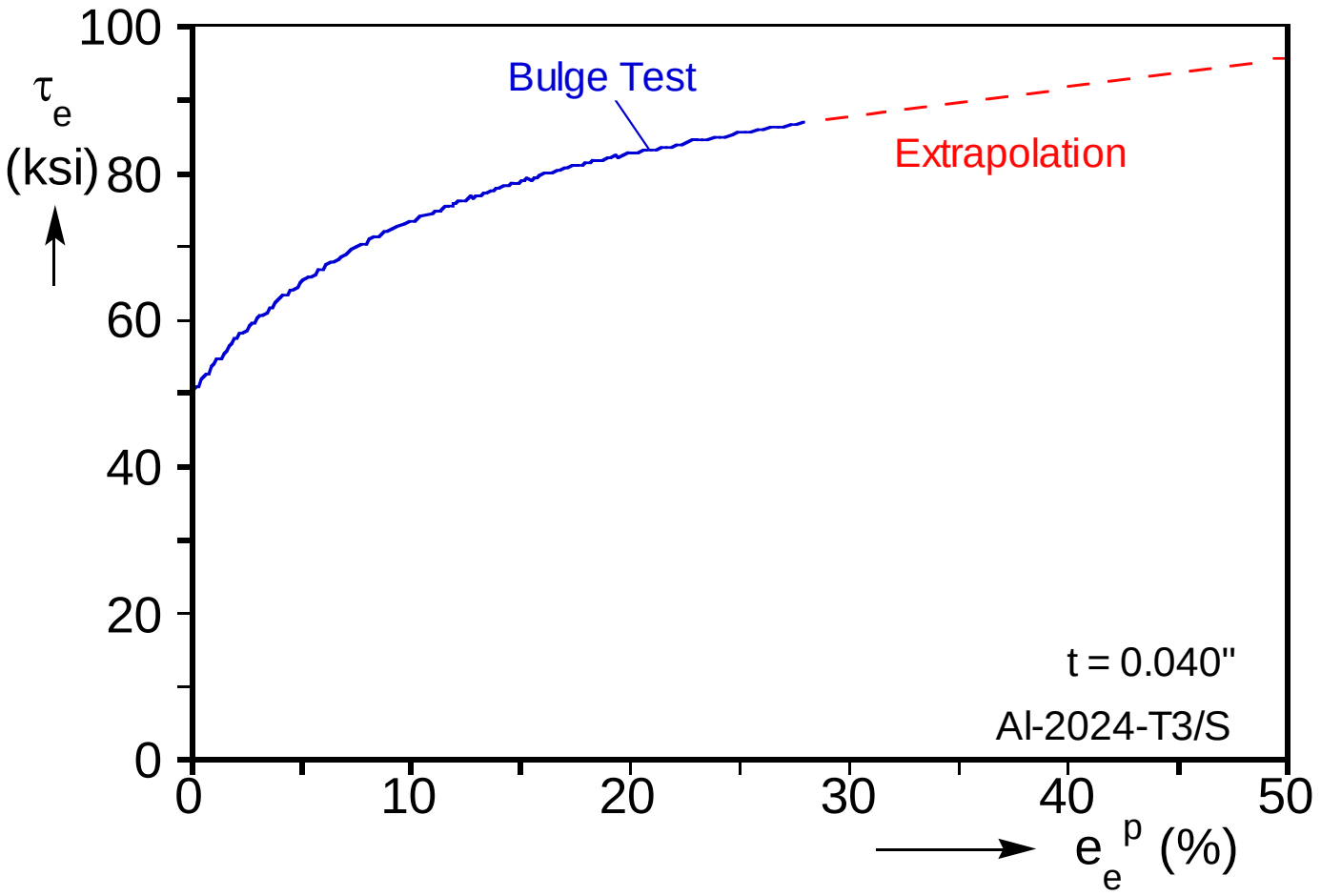

Figure 3.3 True stress-logarithmic strain extracted from a bulge test and the extrapolation adopted.

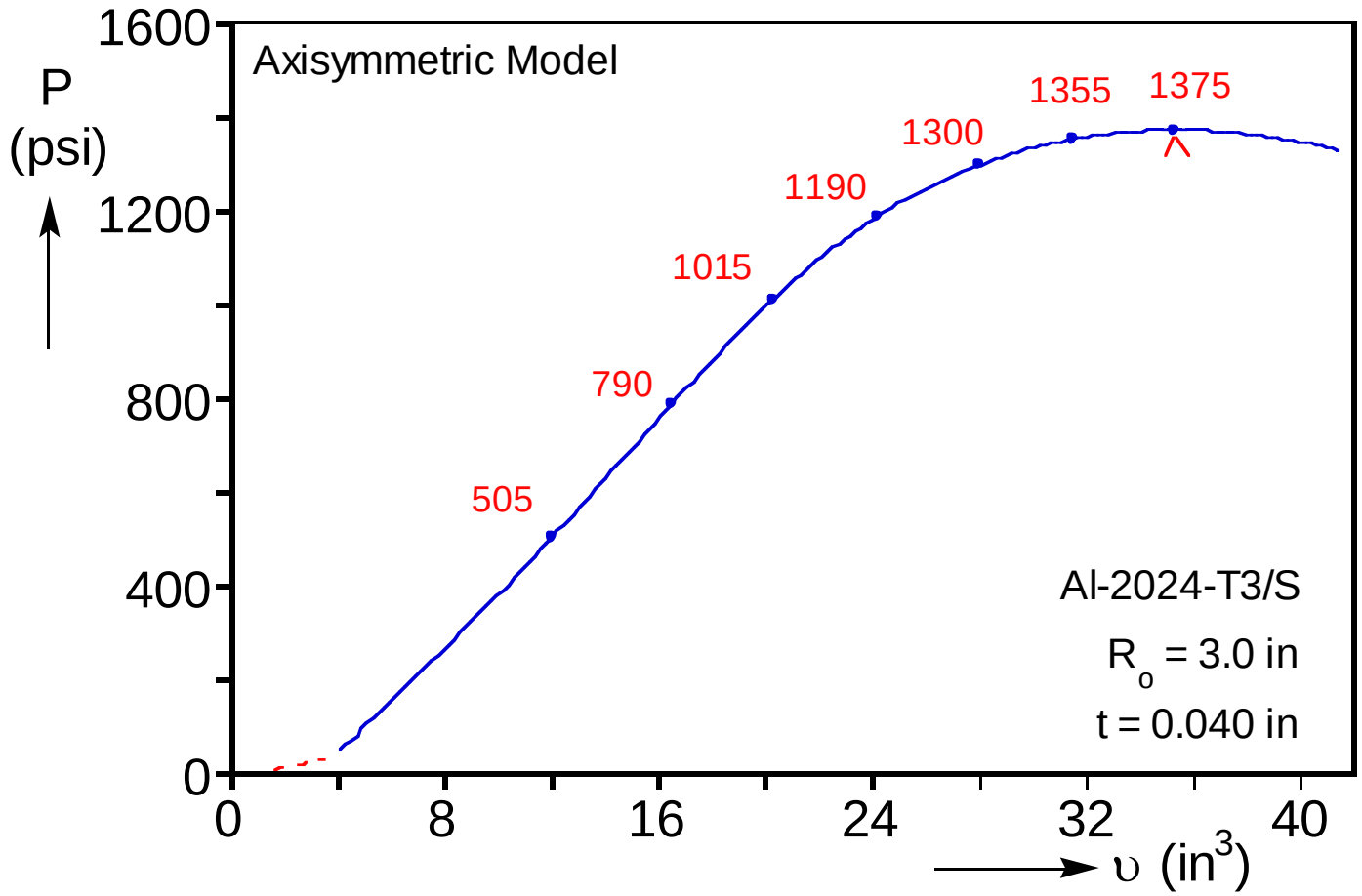

Figure 3.4 Calculated pressure-volume response for the base case.

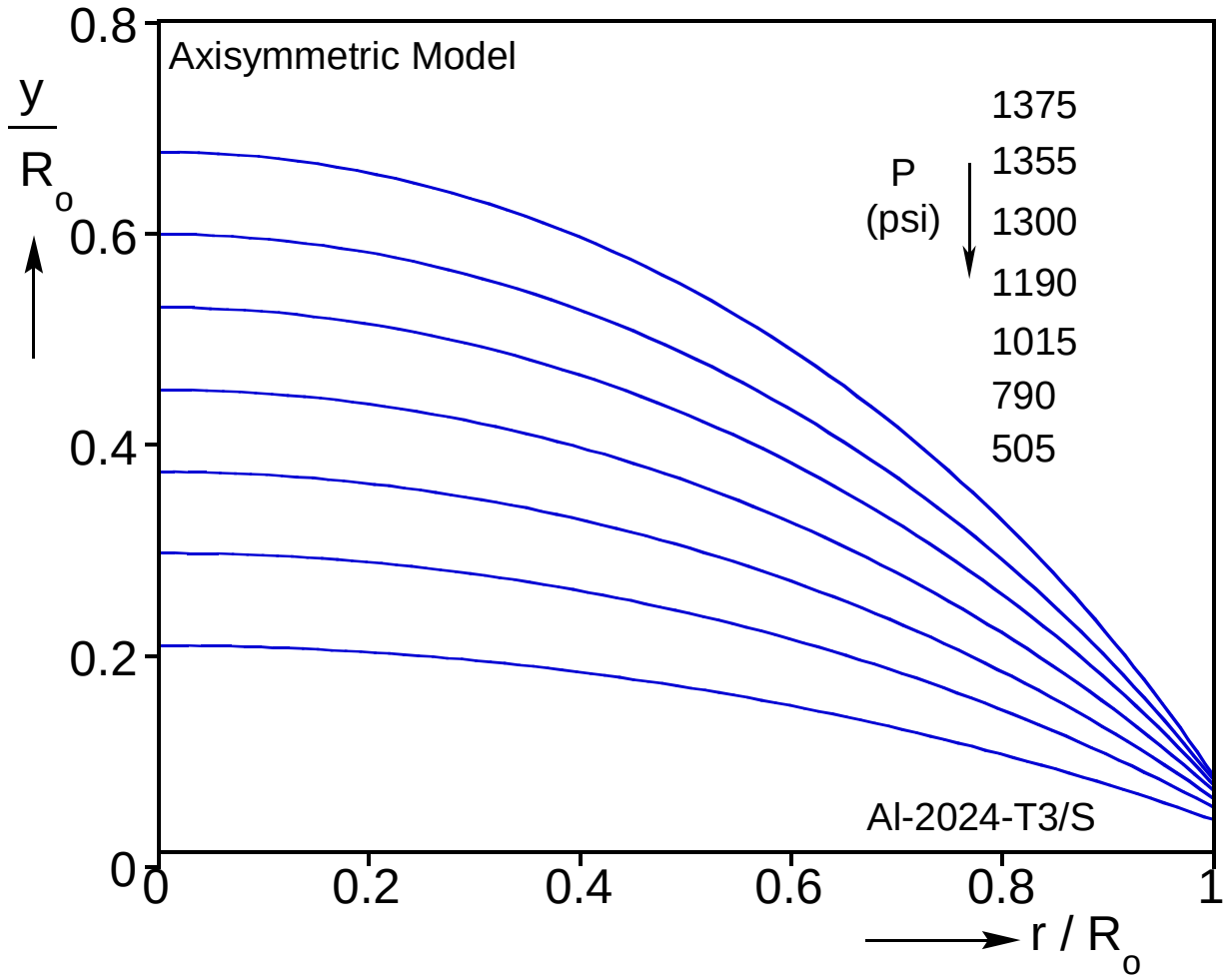

Figure 3.5 Evolution of bulged specimen with pressure.

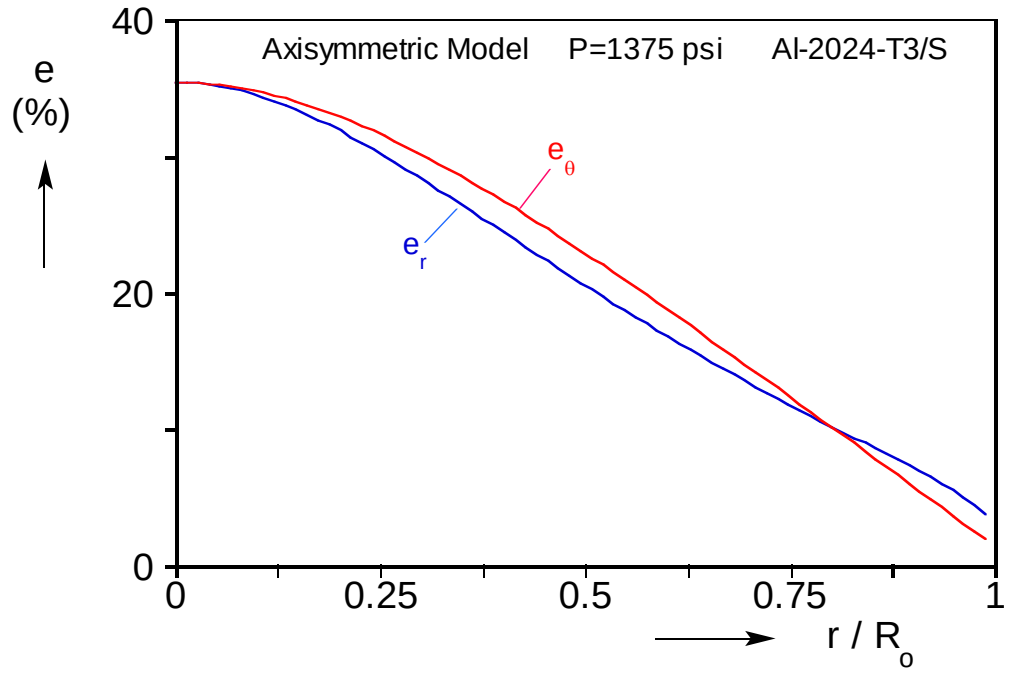

(a)

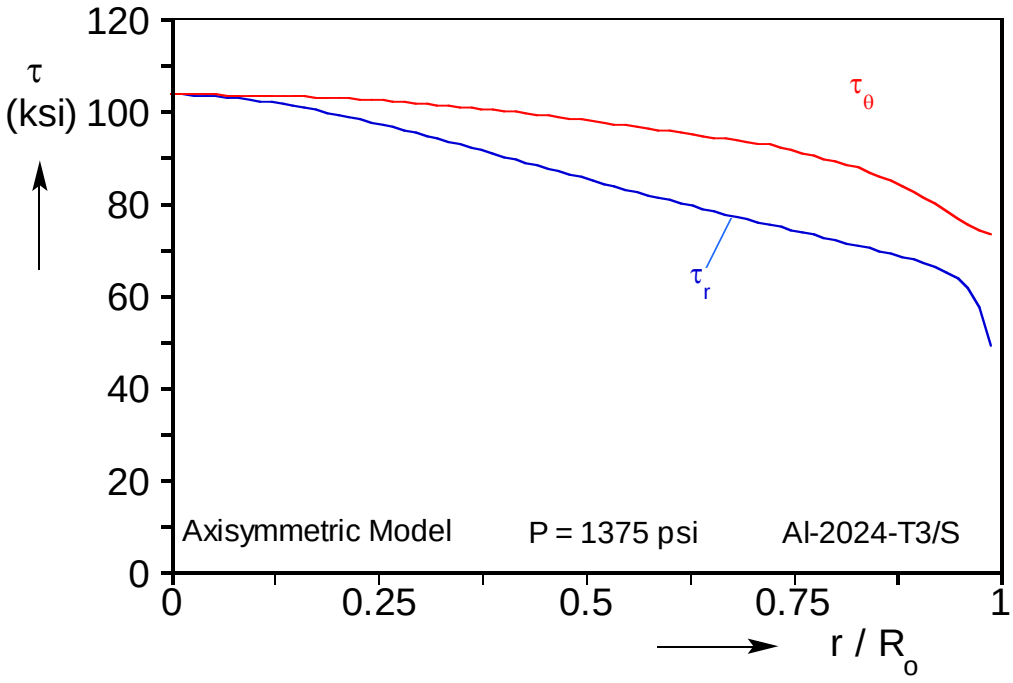

(b)

Figure 3.6 Logarithmic strains (a) and true stresses (b) in the r and θ directions at maximum pressure.

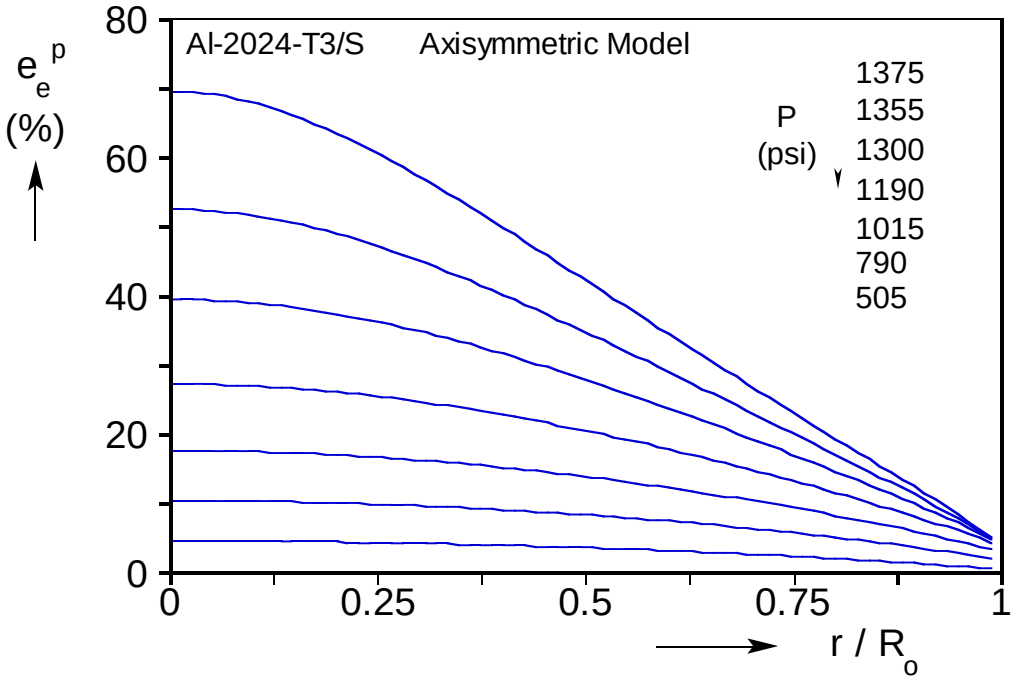

(a)

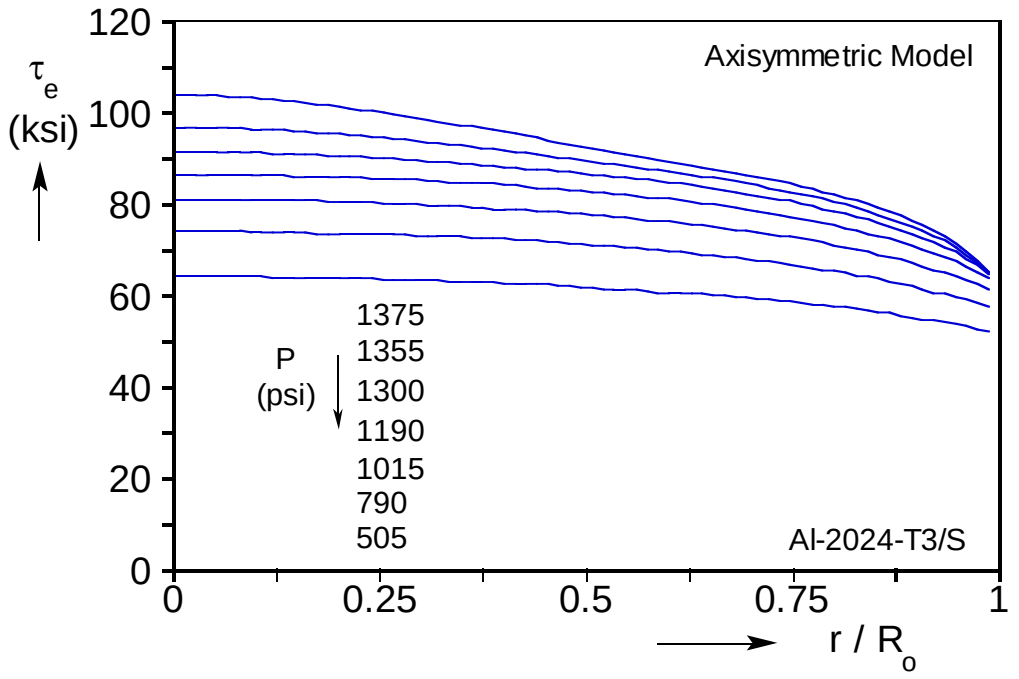

(b)

Figure 3.7 (a) True plastic equivalent strain and (b) true equivalent stress vs. radial position.

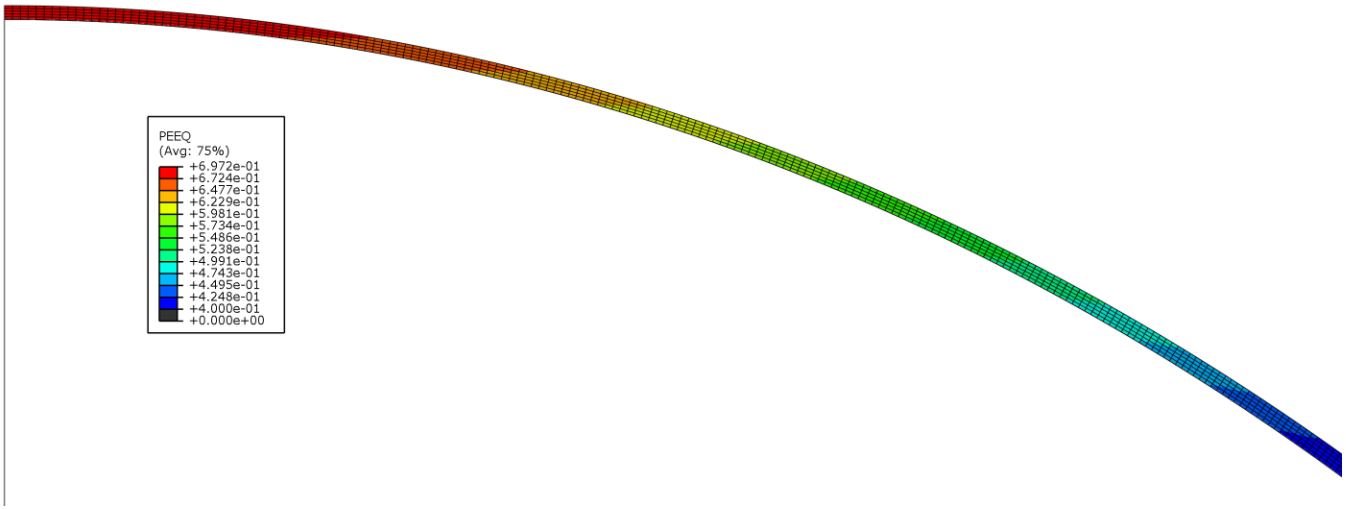

(a)

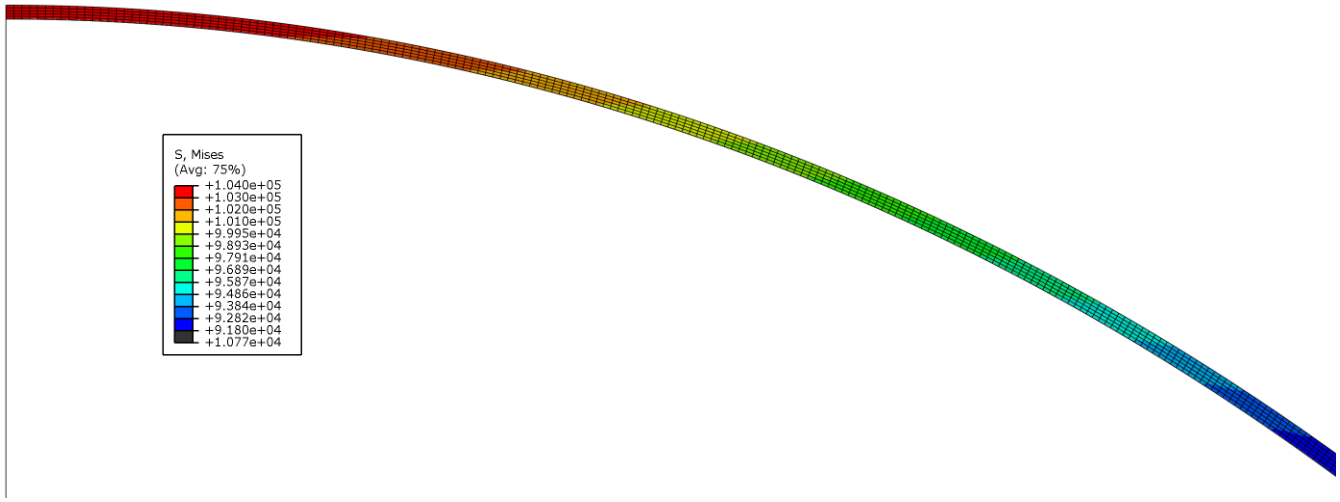

(b)

Figure 3.8 Deformed configurations showing plastic equivalent strain (a) and equivalent stresses (b) at P_{max}.

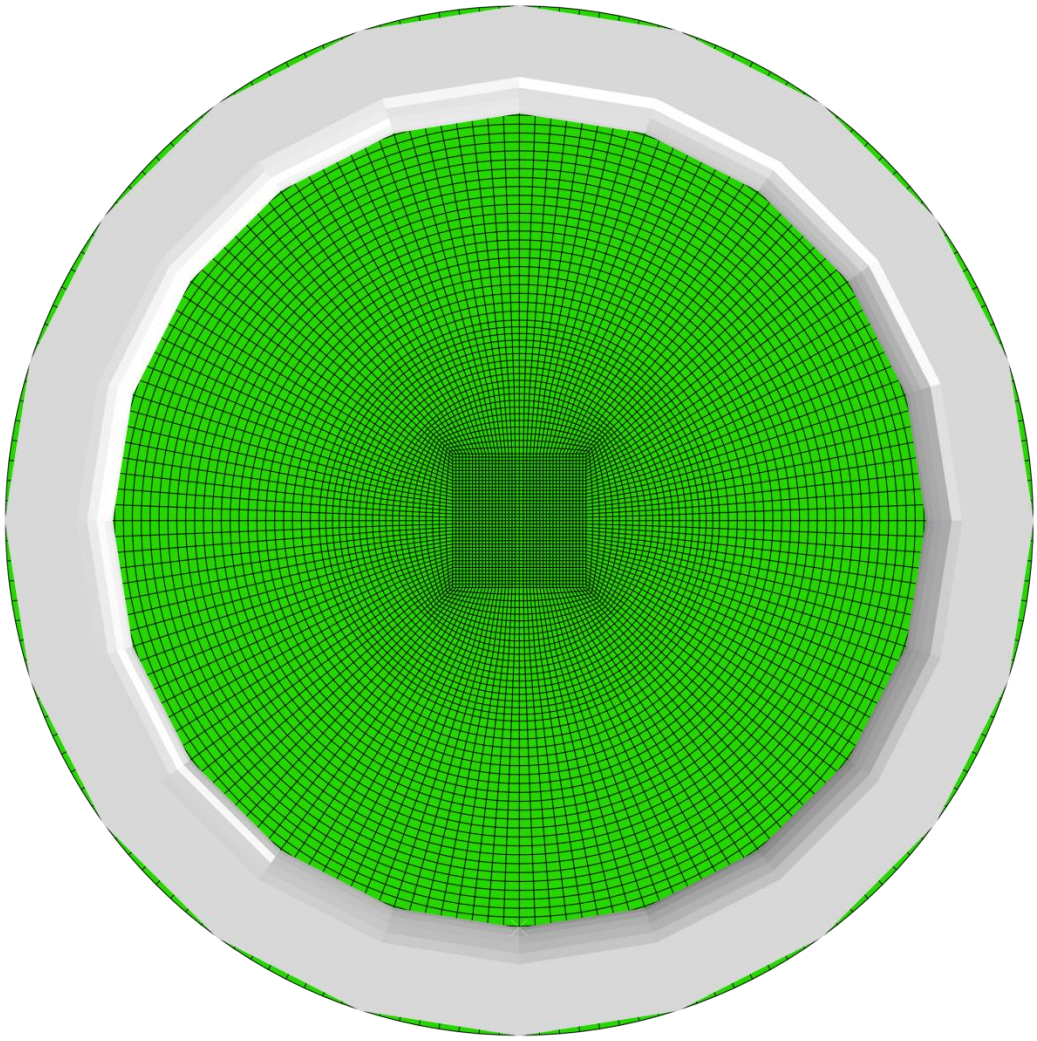

(a)

(b)

Figure 3.9 The shell model mesh with clamping ring: (a) top view and (b) cross-sectional view—half of the model.

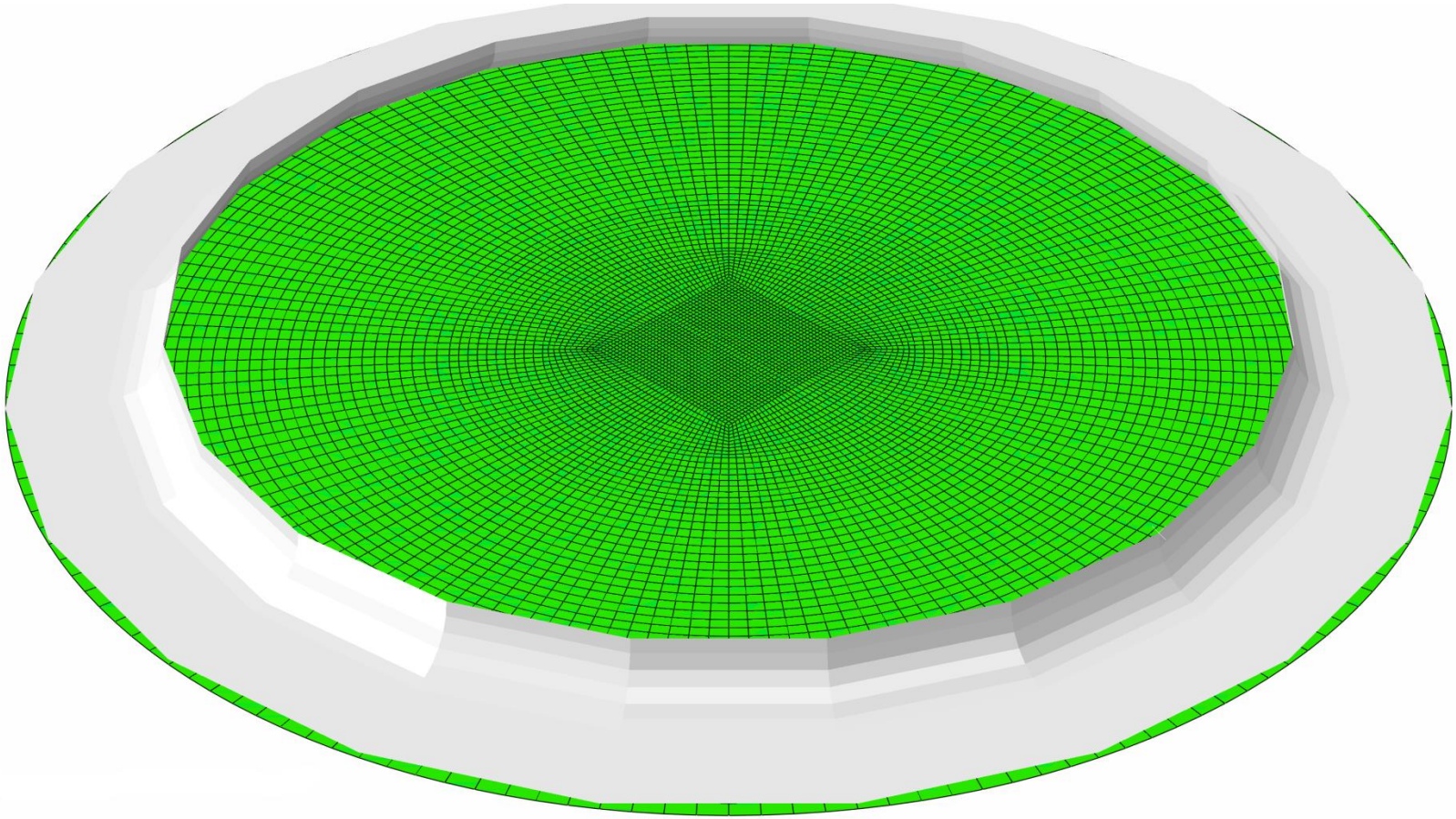

Figure 3.10 Isometric view of shell model mesh with the clamping ring.

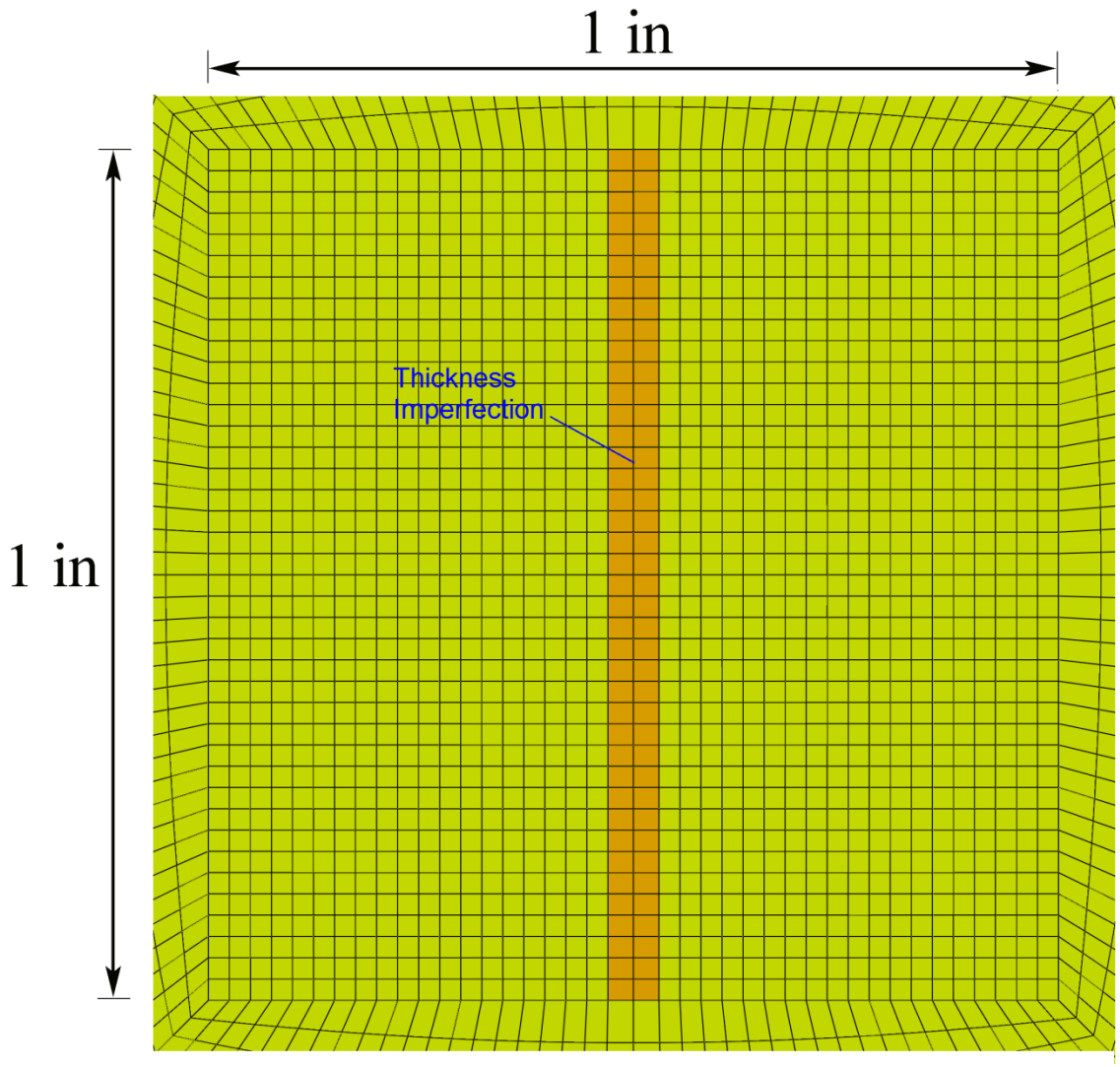

Figure 3.11 Zoomed in view of the central zone of the plate and the thickness imperfection (seen in orange).

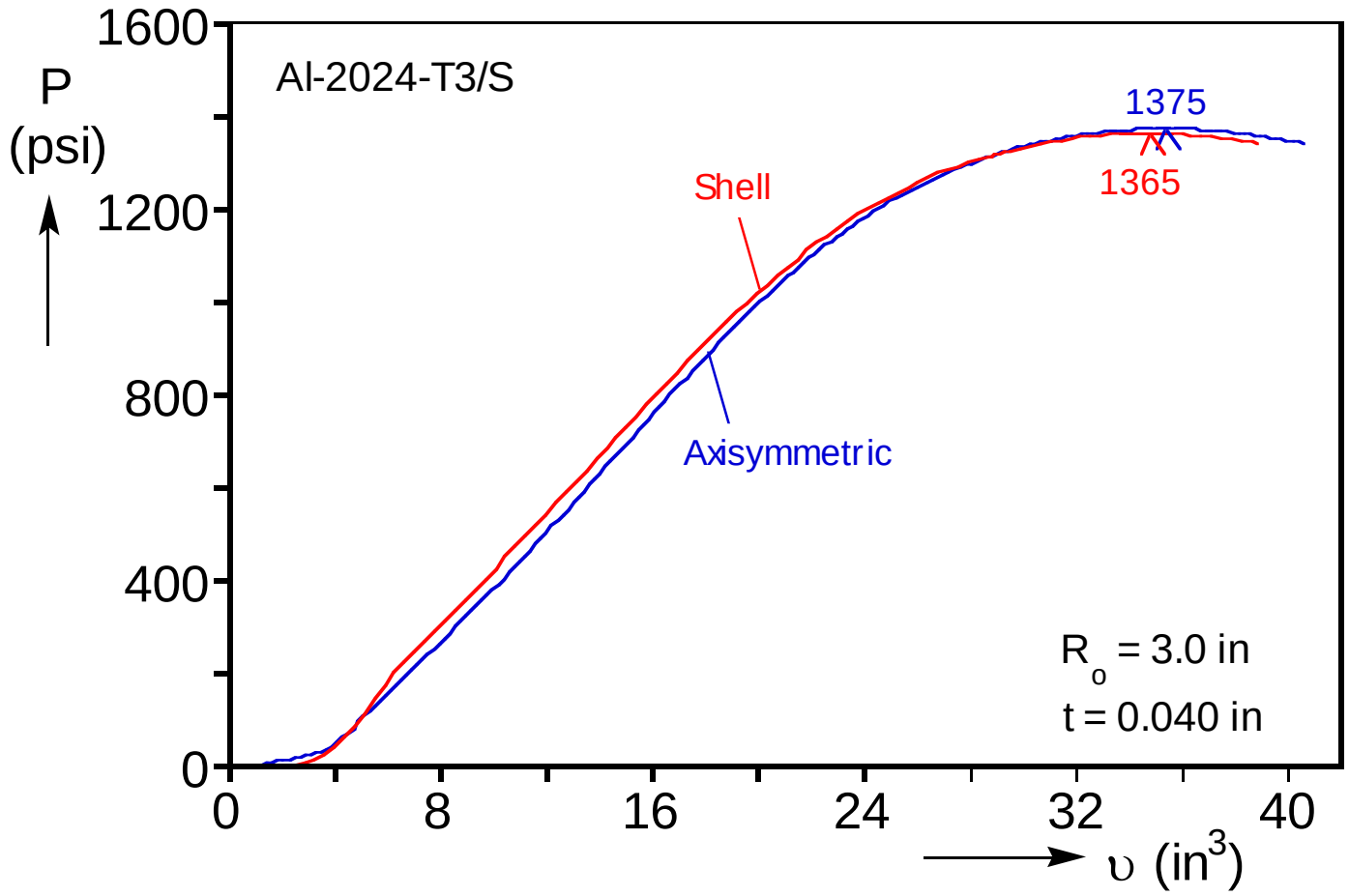

Figure 3.12 Comparison of the pressure-volume responses of the axisymmetric and shell models.

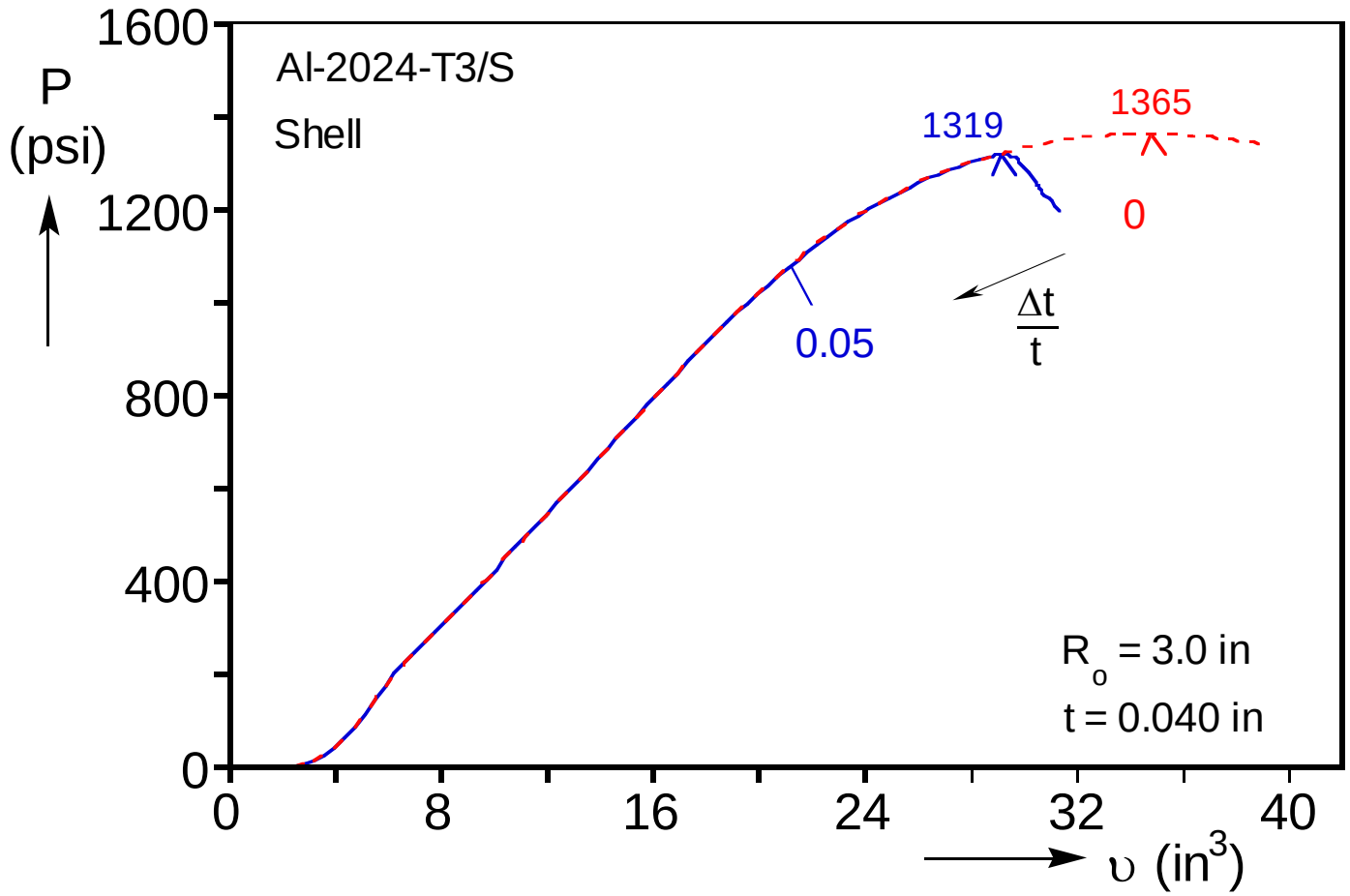

Figure 3.13 Shell model pressure-volume response for the perfect and an imperfect geometry.

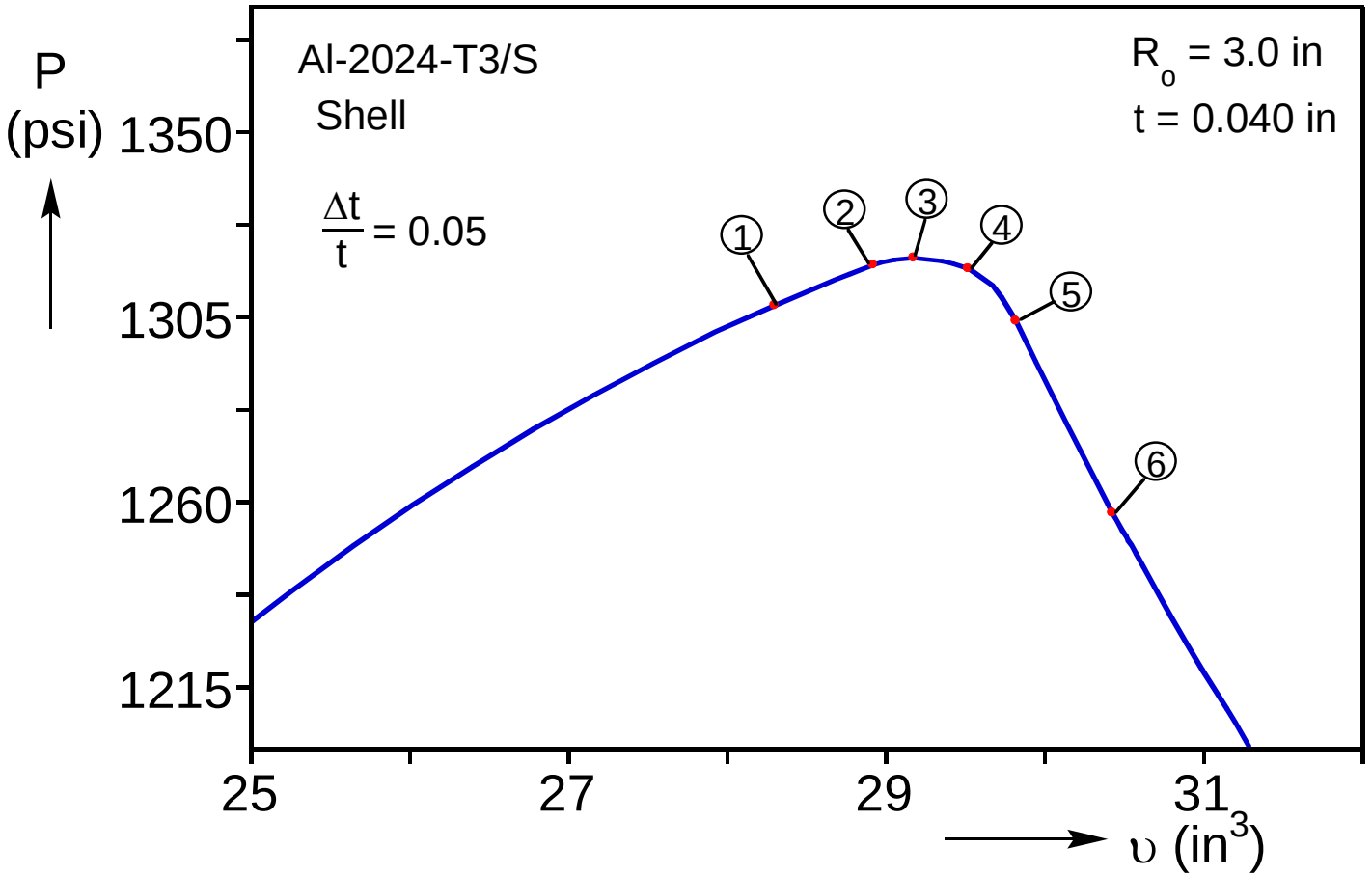

Figure 3.14 Expanded pressure-volume response in the neighborhood of the pressure maximum—shell model.

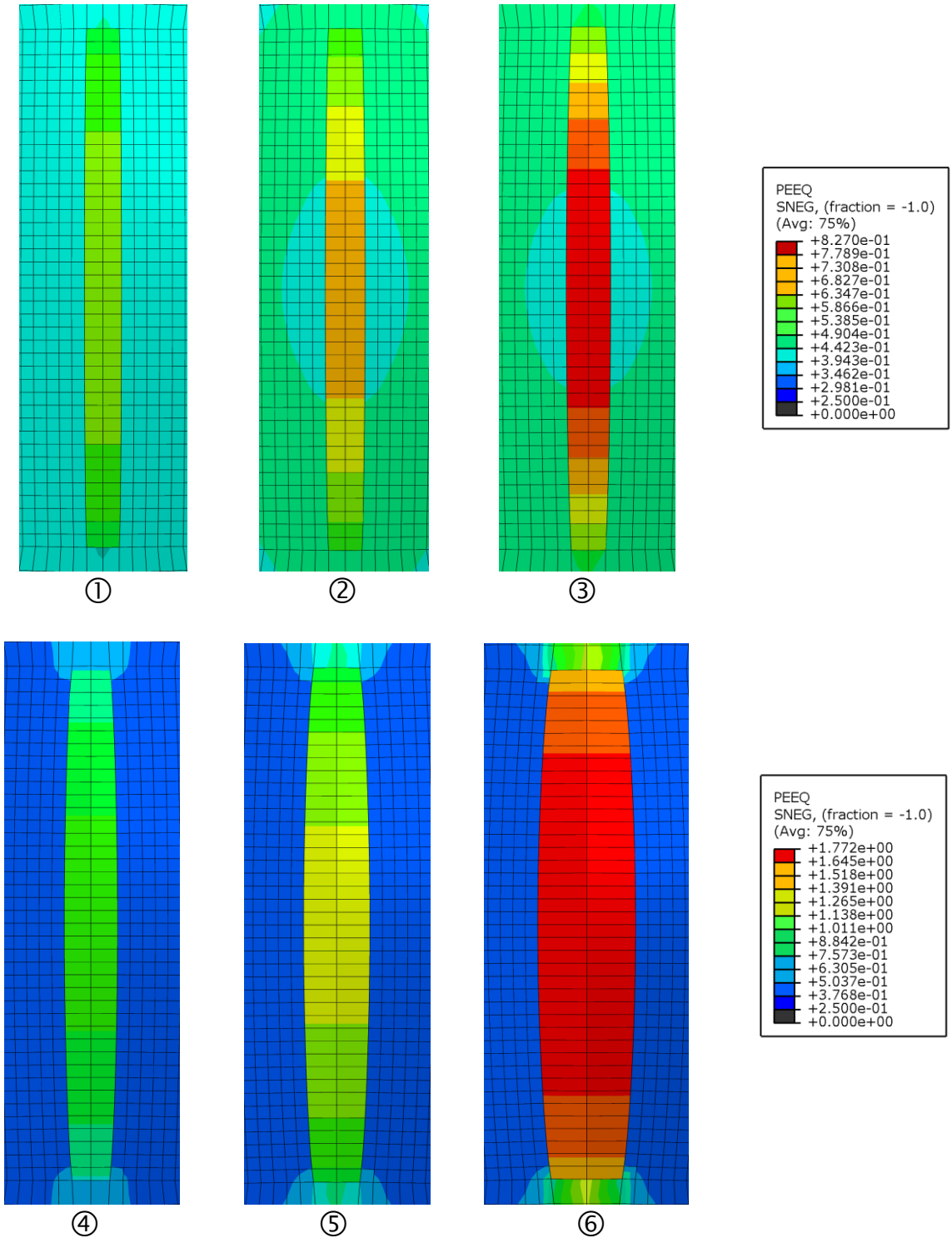

Figure 3.15 Evolution of imperfection around the maximum pressure (numbers correspond to points on response in Figure 3.14)—shell model.

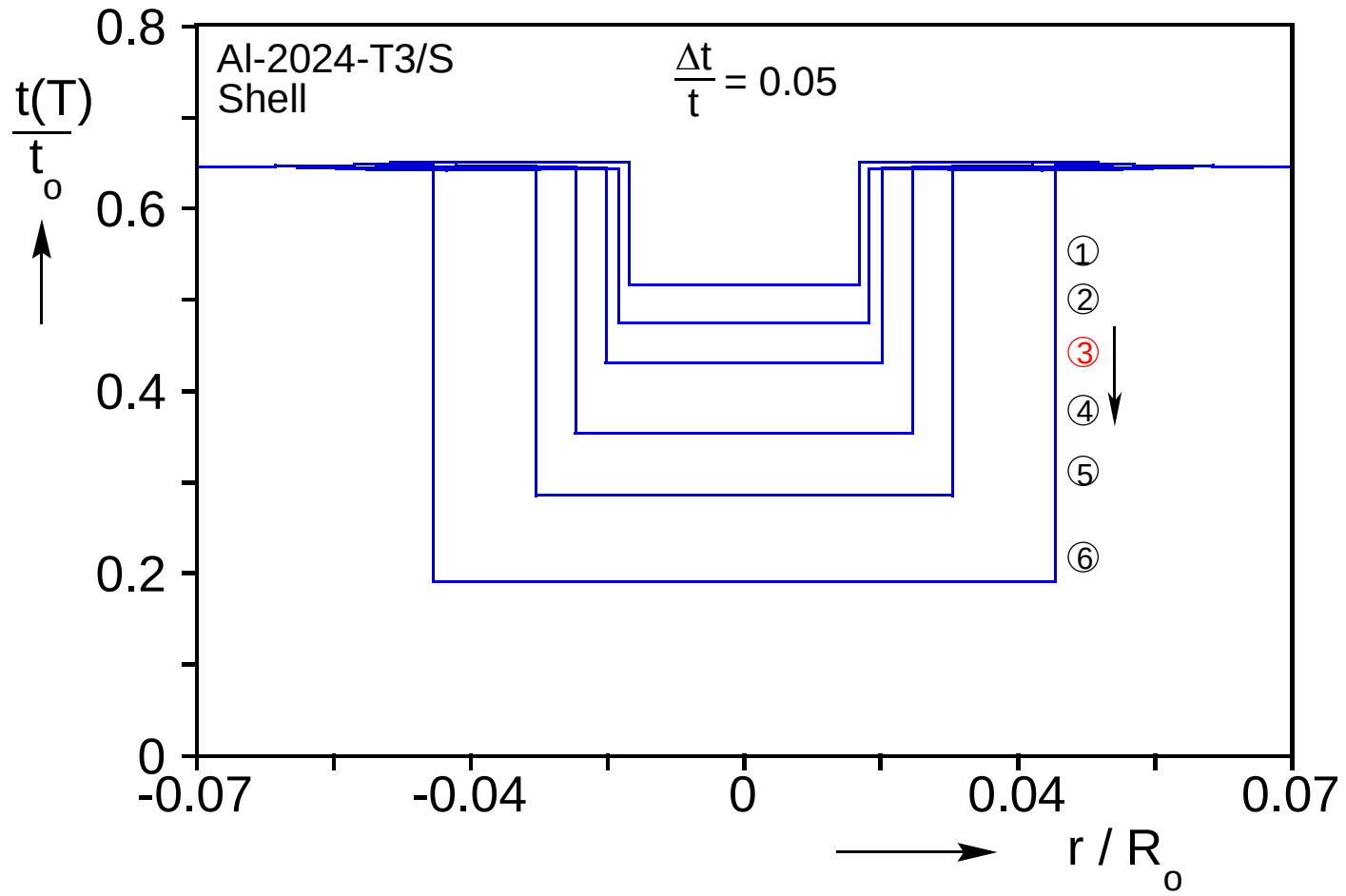

Figure 3.16 Evolution of thickness of the imperfection at apex around the pressure maximum (numbers correspond to points on response in Figure 3.14)—shell model.

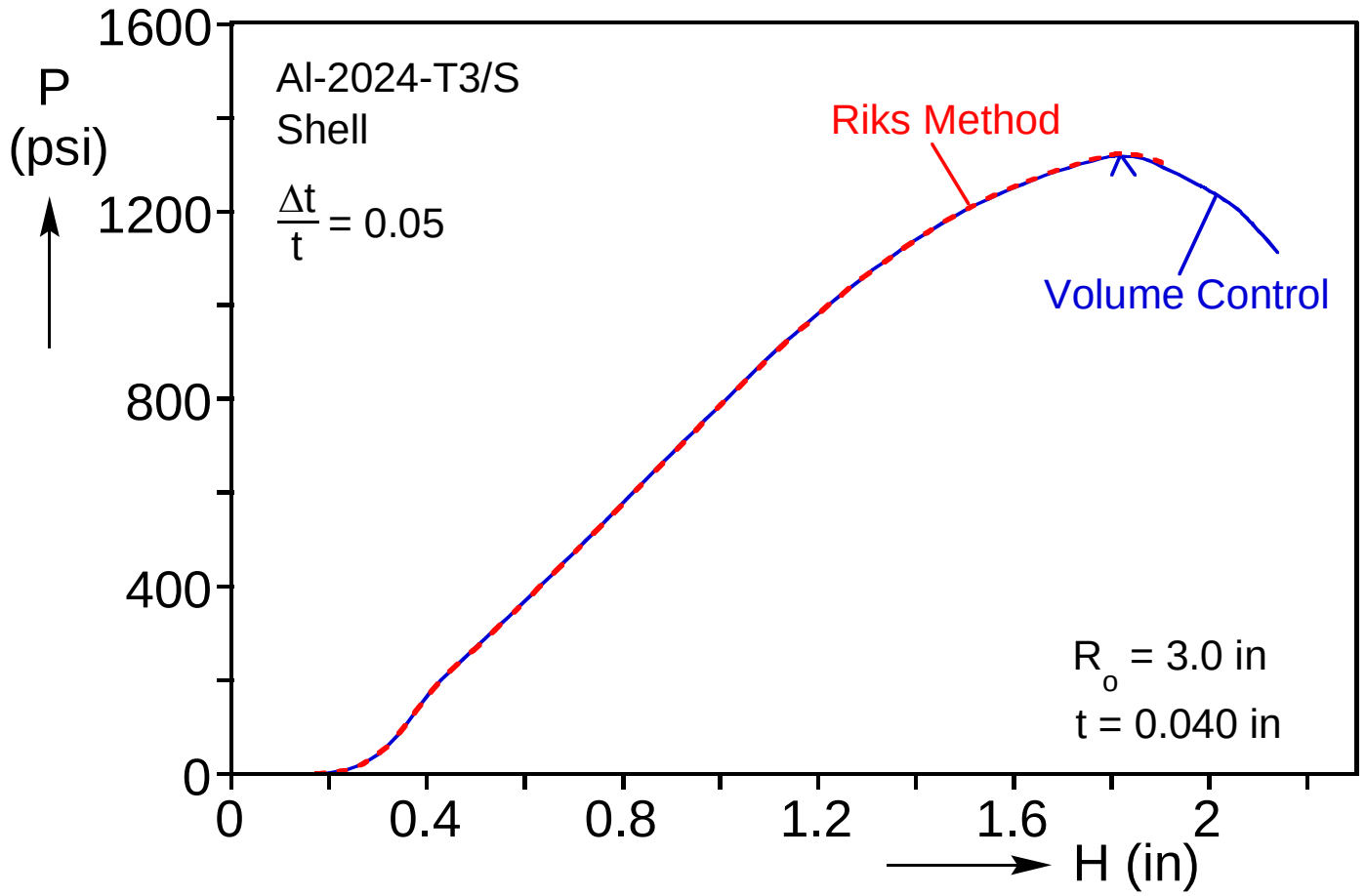

Figure 3.17 Pressure-height response—shell model.

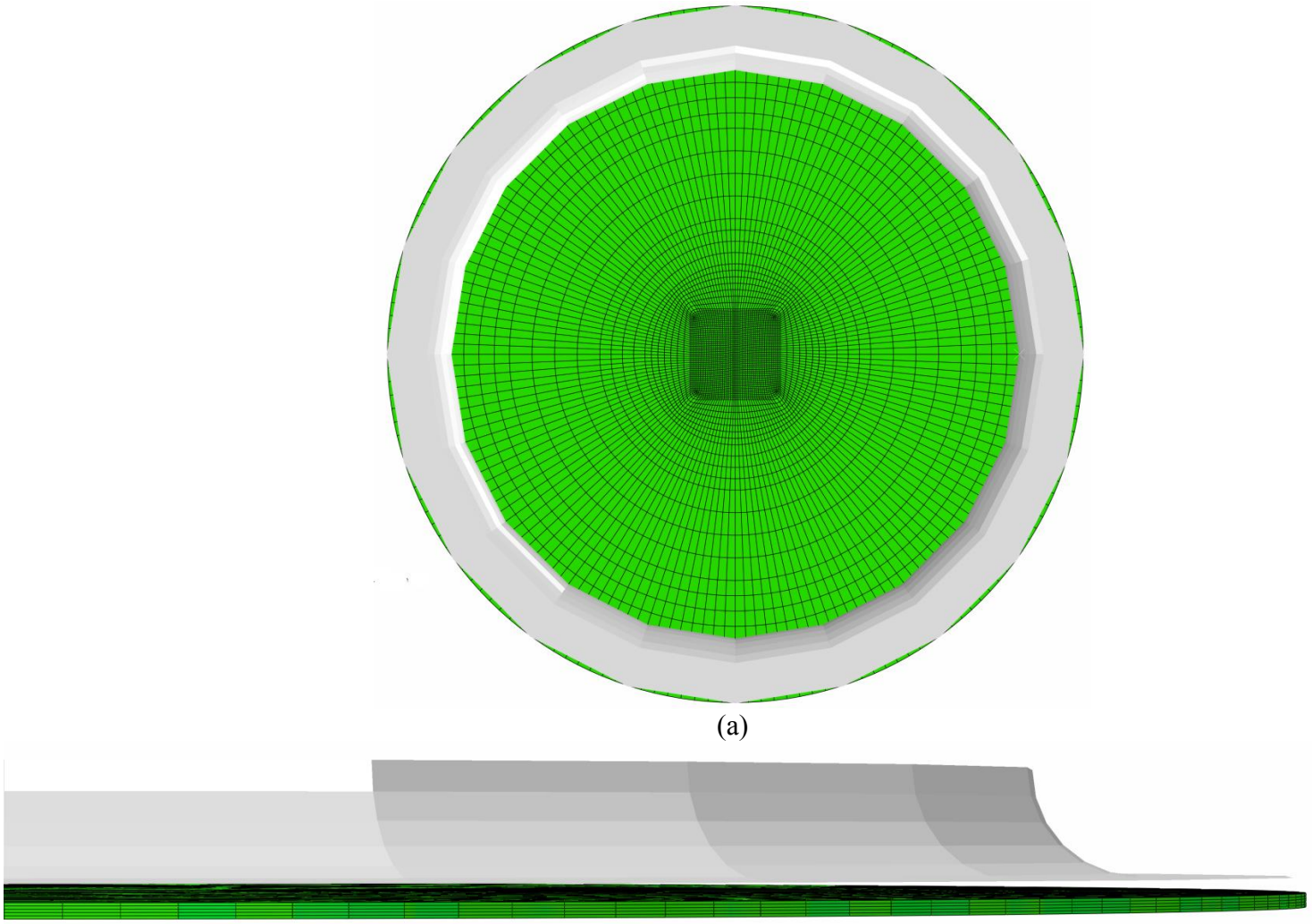

(a)

(b)

Figure 3.18 The solid model mesh with clamping ring: (a) top view and (b) cross-sectional view—half of the model.

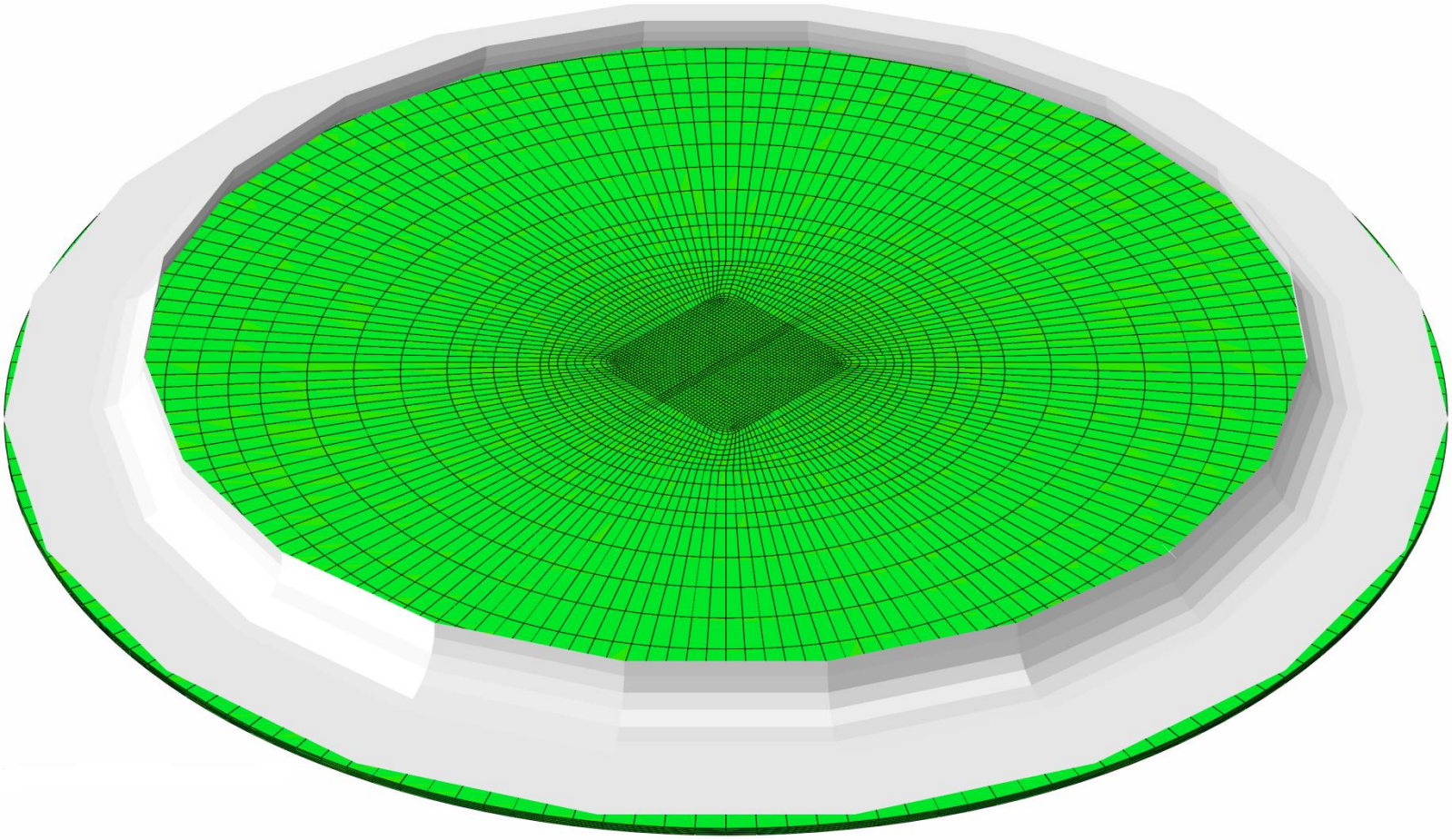

Figure 3.19 Isometric view of shell model mesh with the clamping ring.

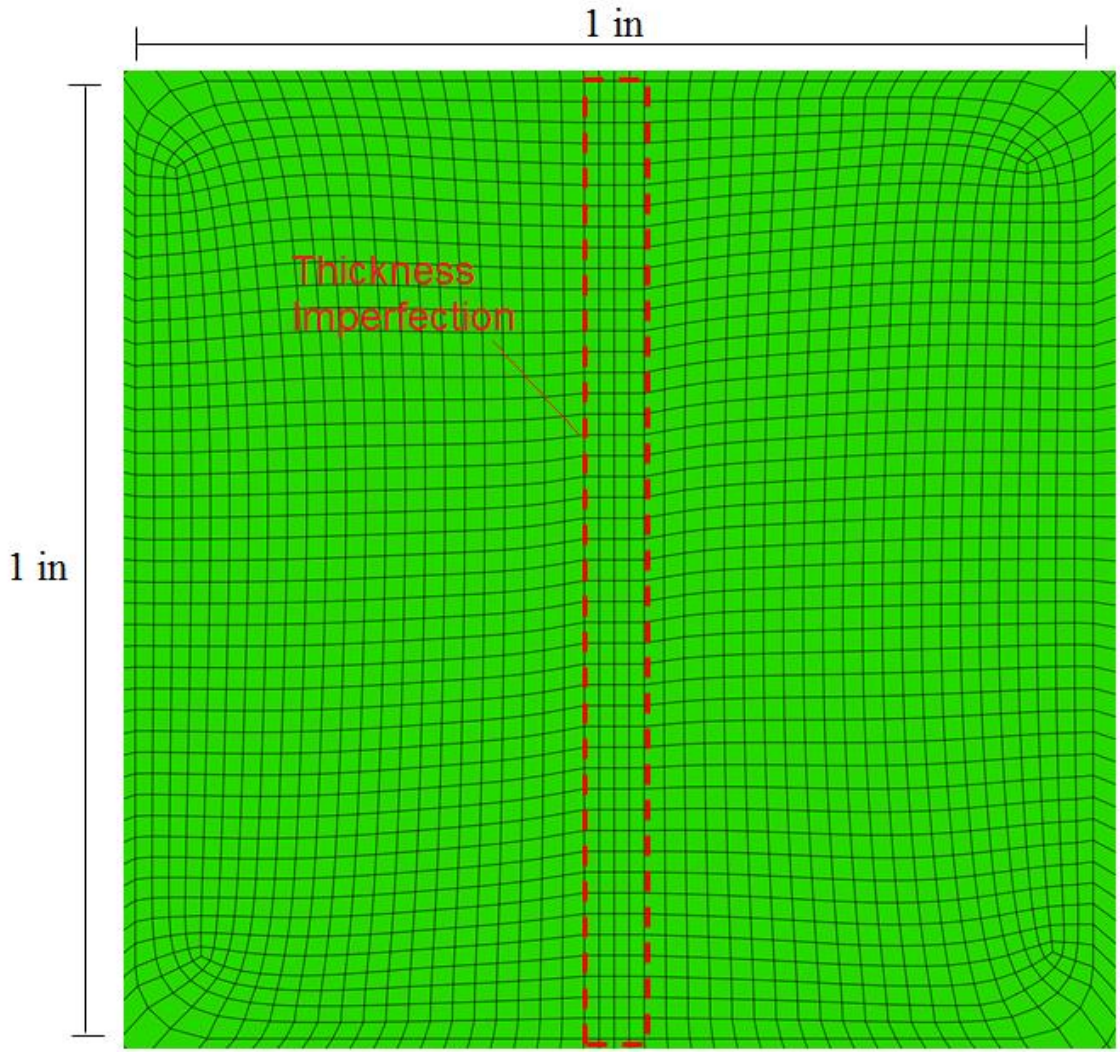

Figure 3.20 Zoomed in view of the central zone of the plate and the thickness imperfection.

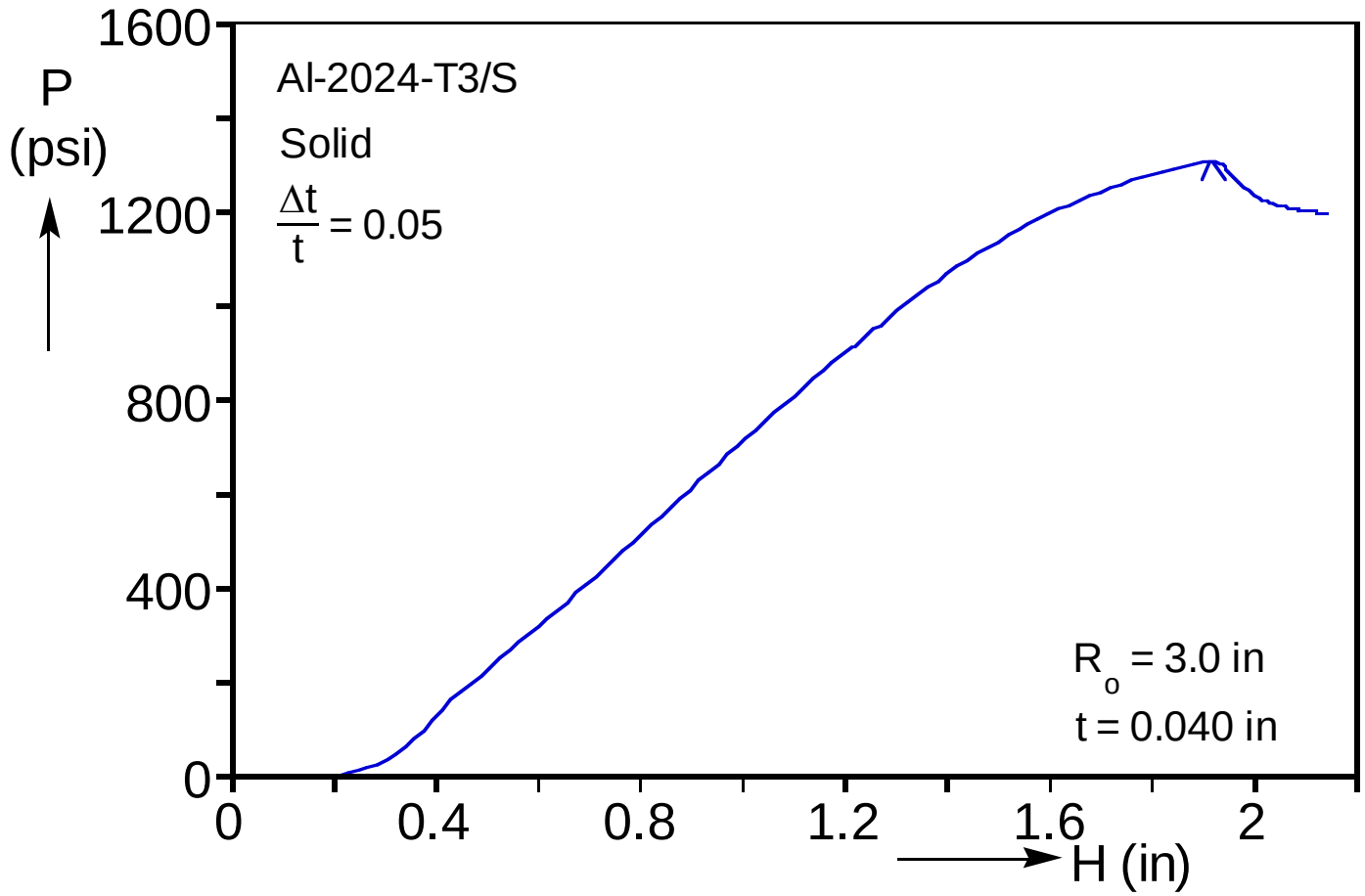

Figure 3.21 Pressure-height response of the solid element model.

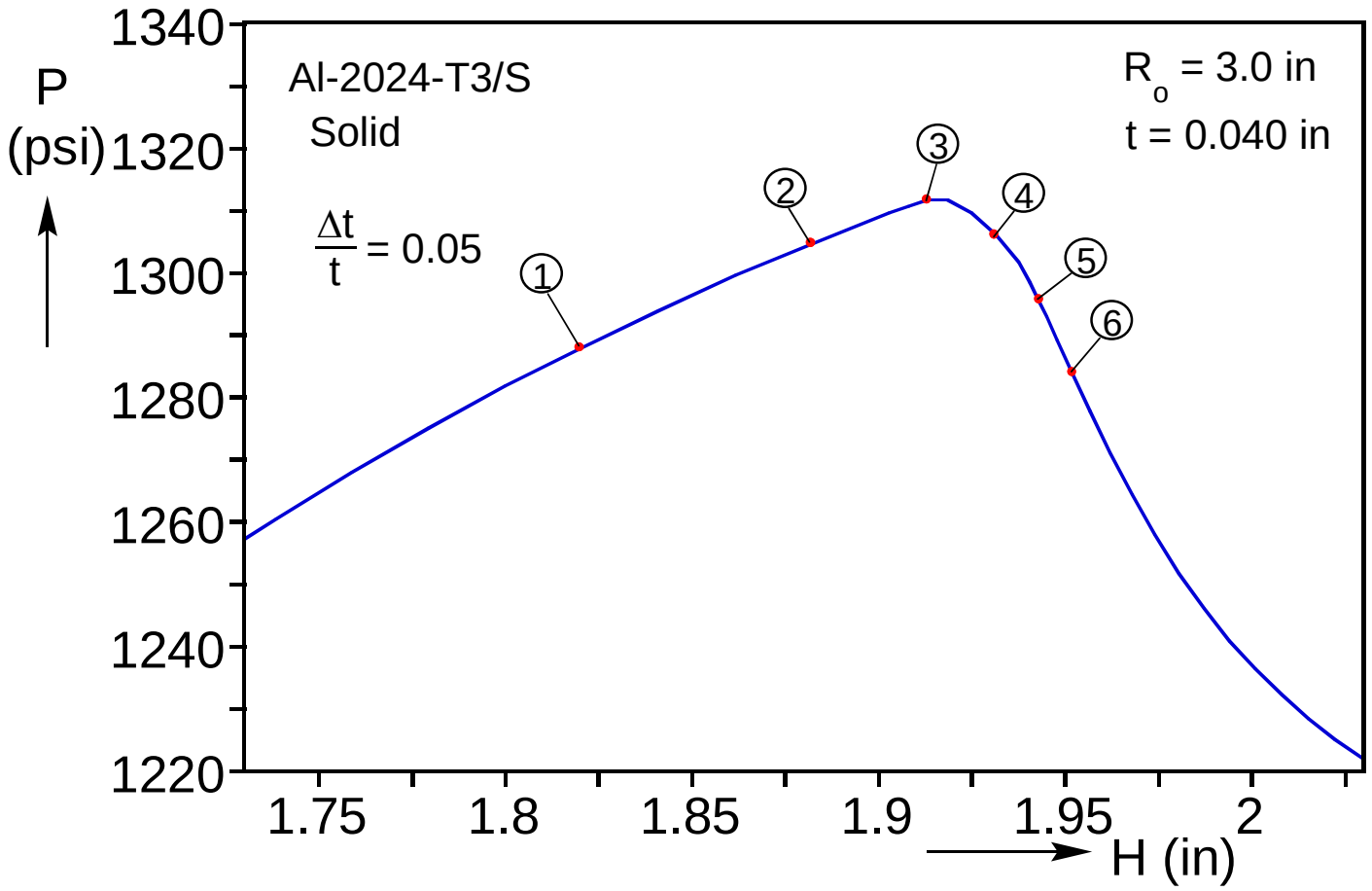

Figure 3.22 Expanded pressure-apex height response in the neighborhood of the pressure maximum—solid model.

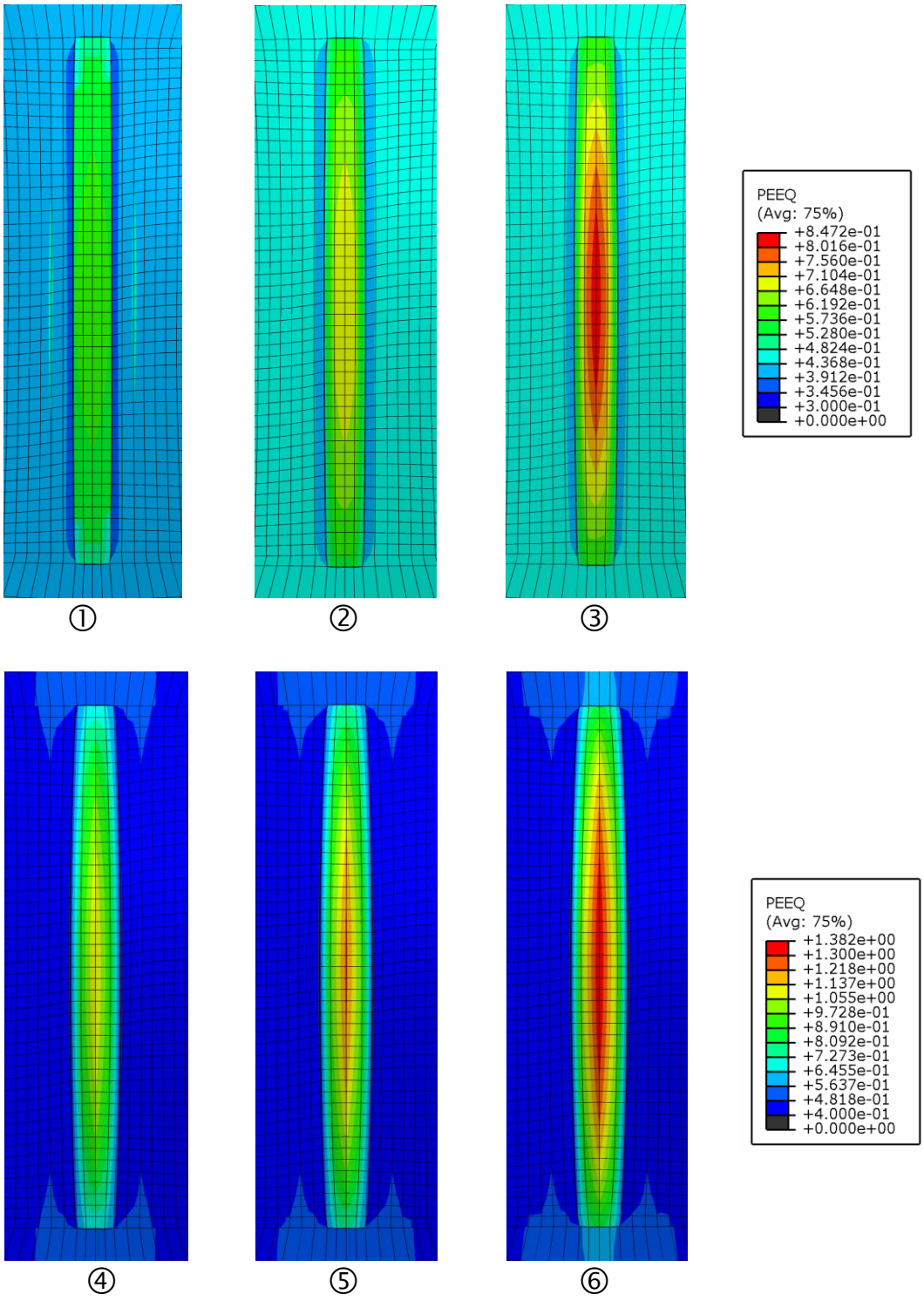

Figure 3.23 Evolution of imperfection around the maximum pressure (numbers correspond to points on response in Figure 3.22)—solid model.

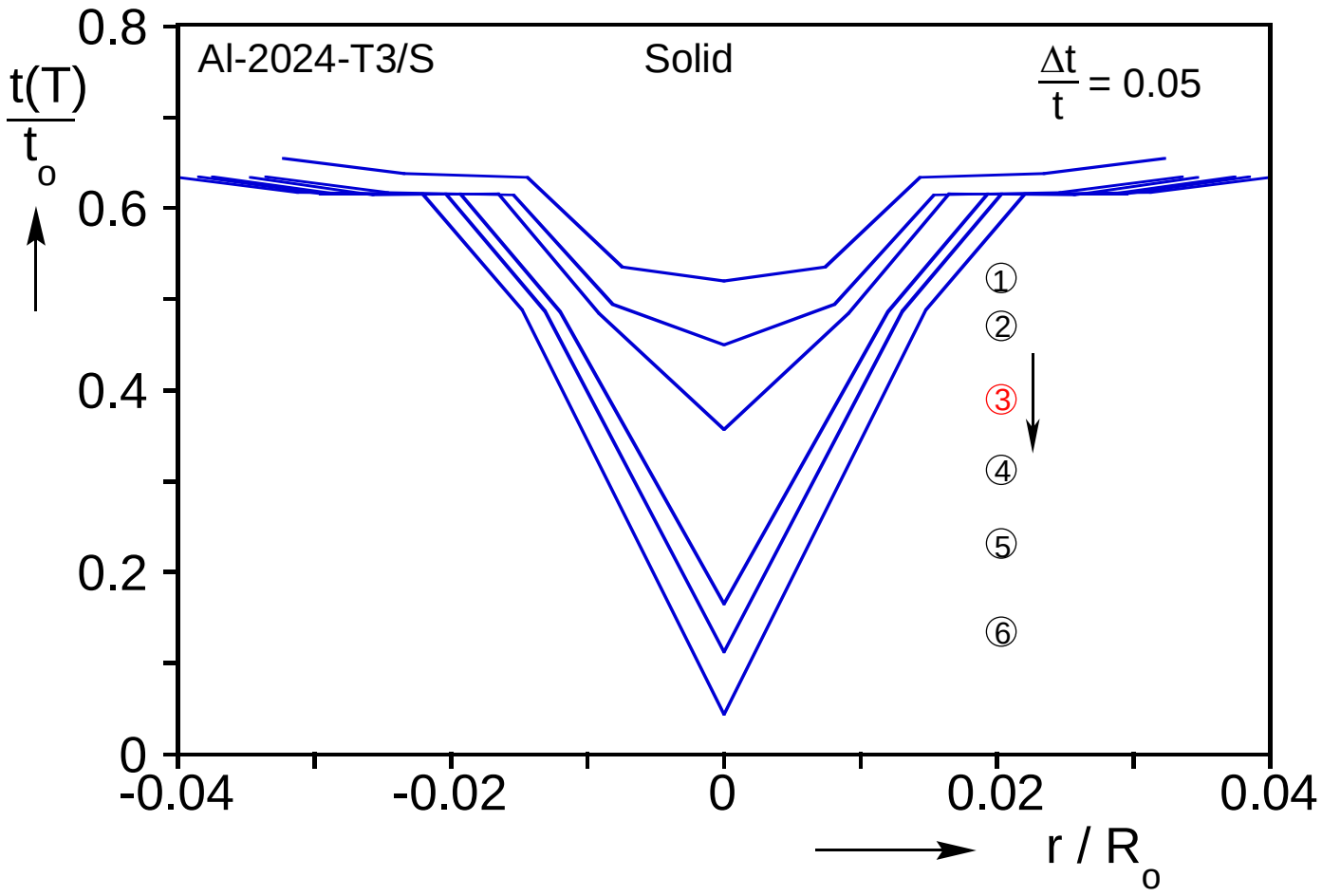

Figure 3.24 Evolution of thickness in the imperfection at the apex around the pressure maximum (numbers correspond to points on response in Figure 3.22)—solid model.

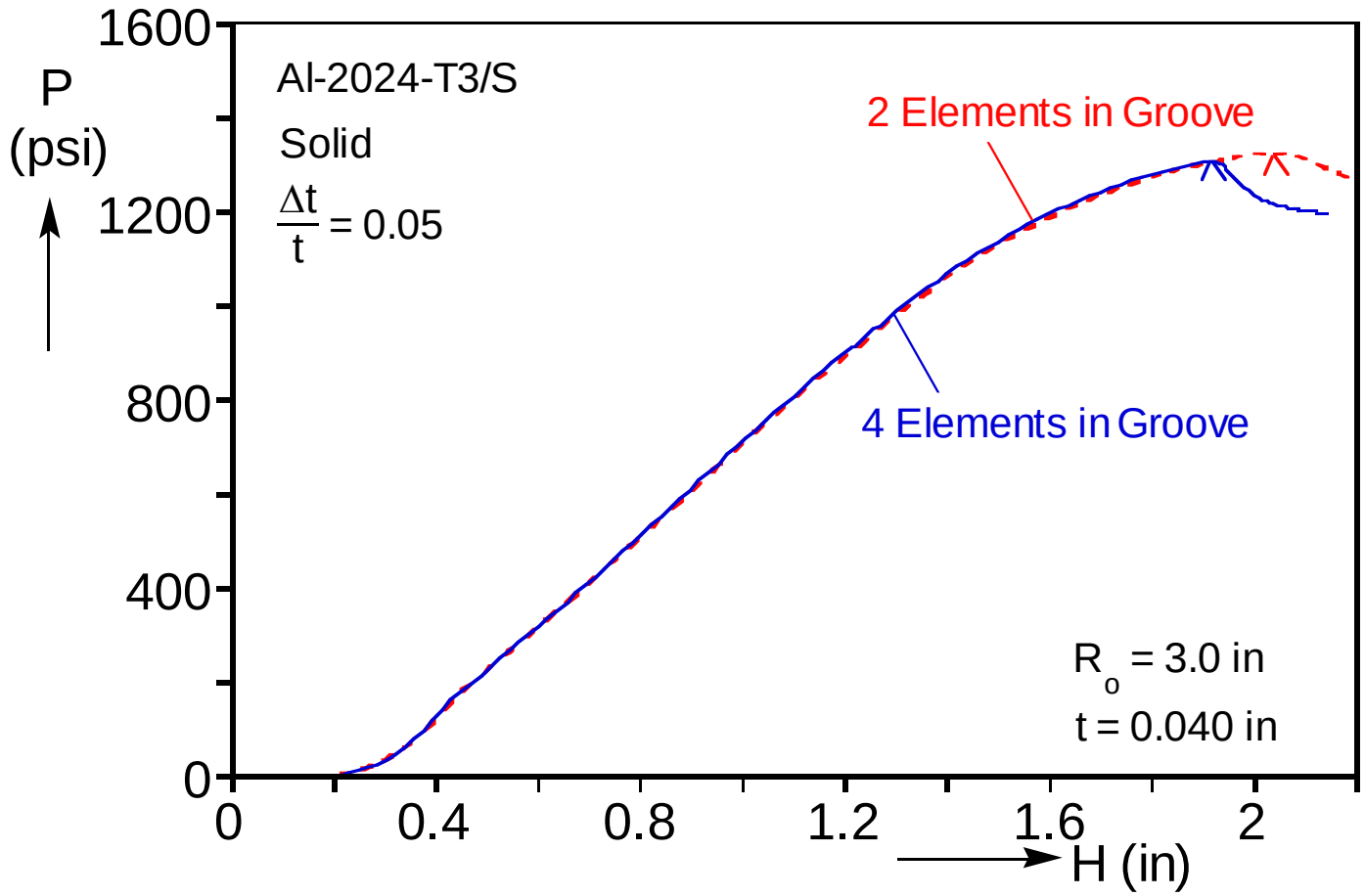

Figure 3.25 Pressure-height responses of the two and four element imperfection solid models.

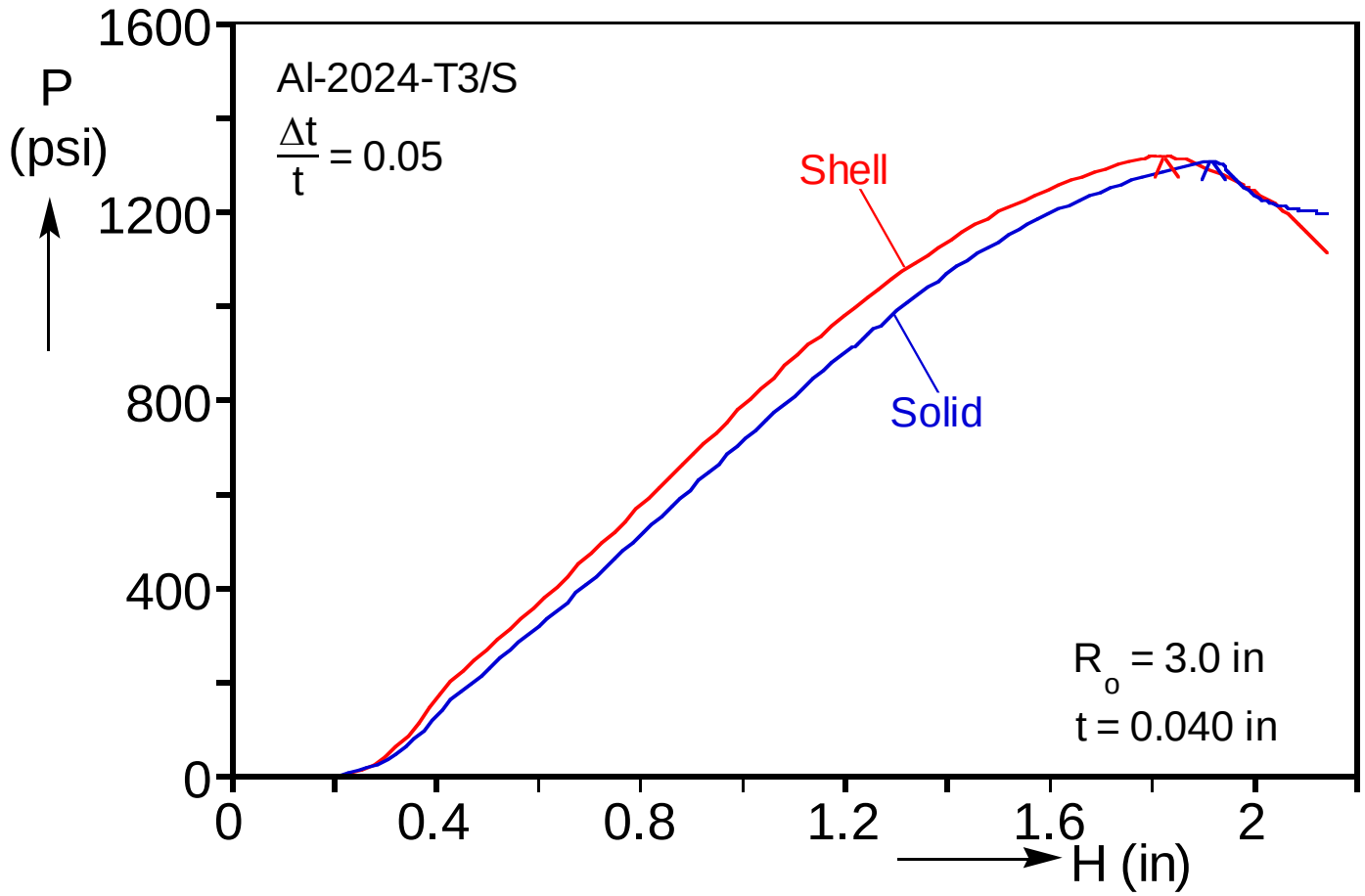

Figure 3.26 Comparison of the pressure-height responses of the solid and shell model.

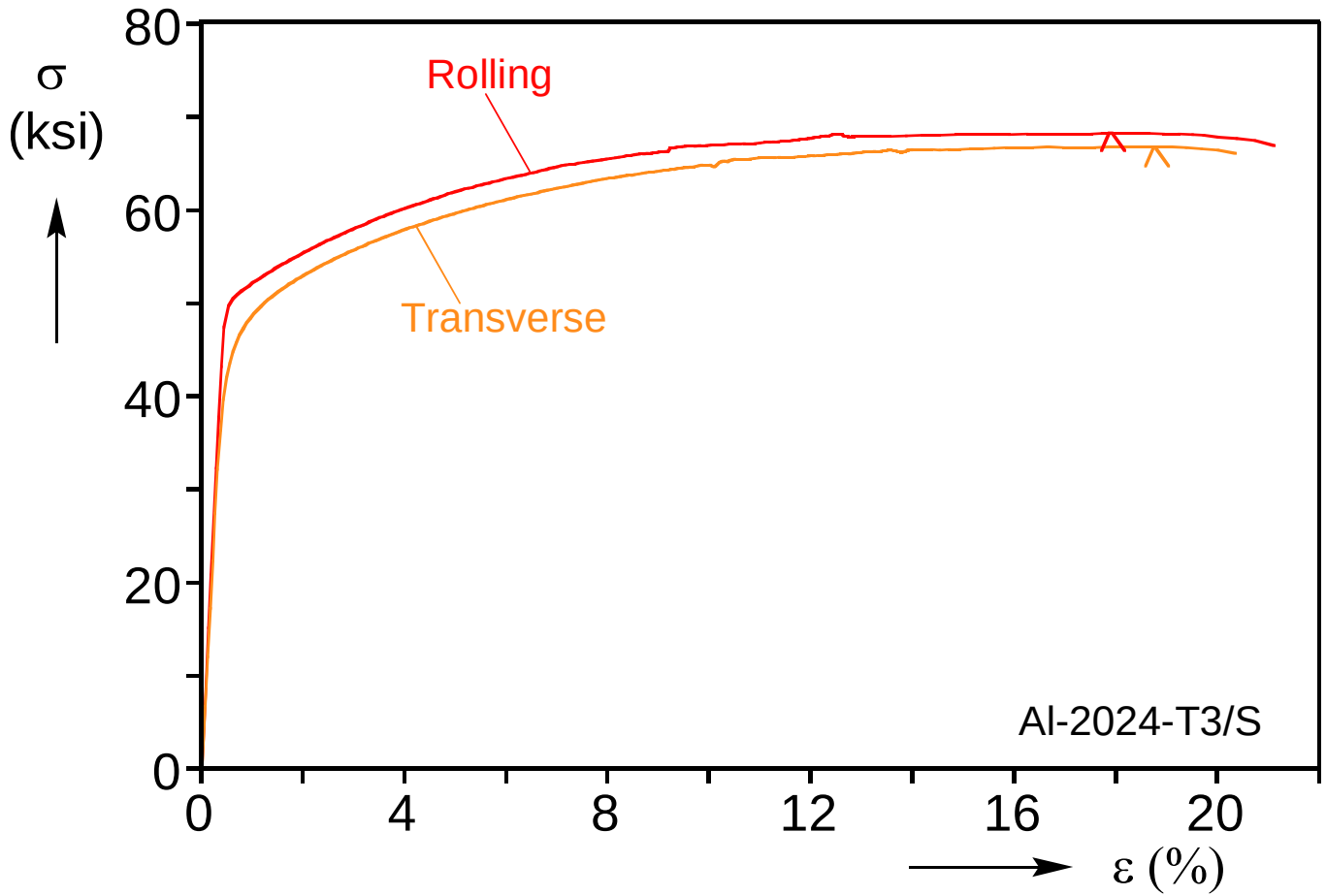

Figure 4.1 Tensile tests in rolling and transverse directions for Al-2024-T3 plate S.

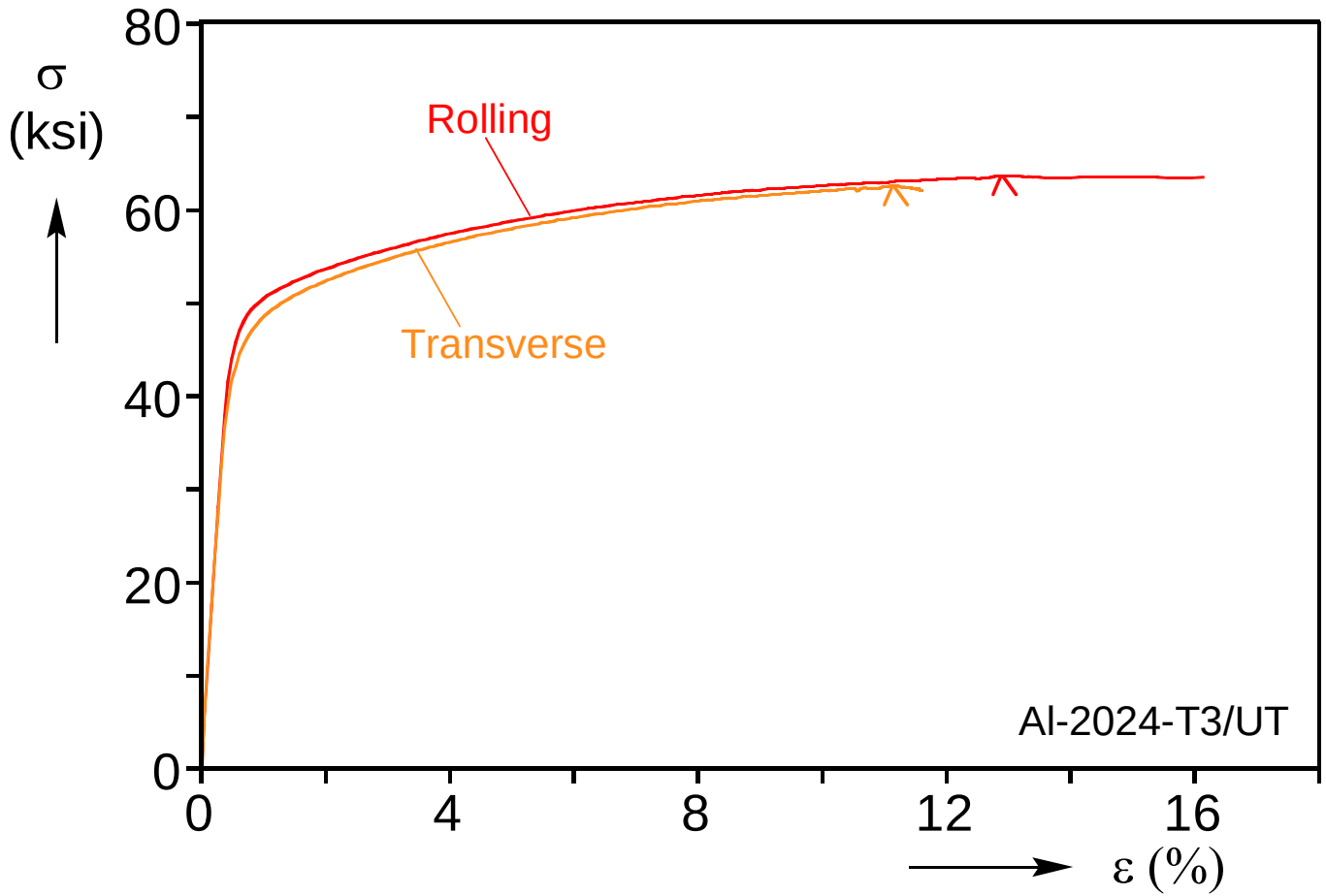

Figure 4.2 Tensile tests in rolling and transverse directions for Al-2024-T3 plate UT.

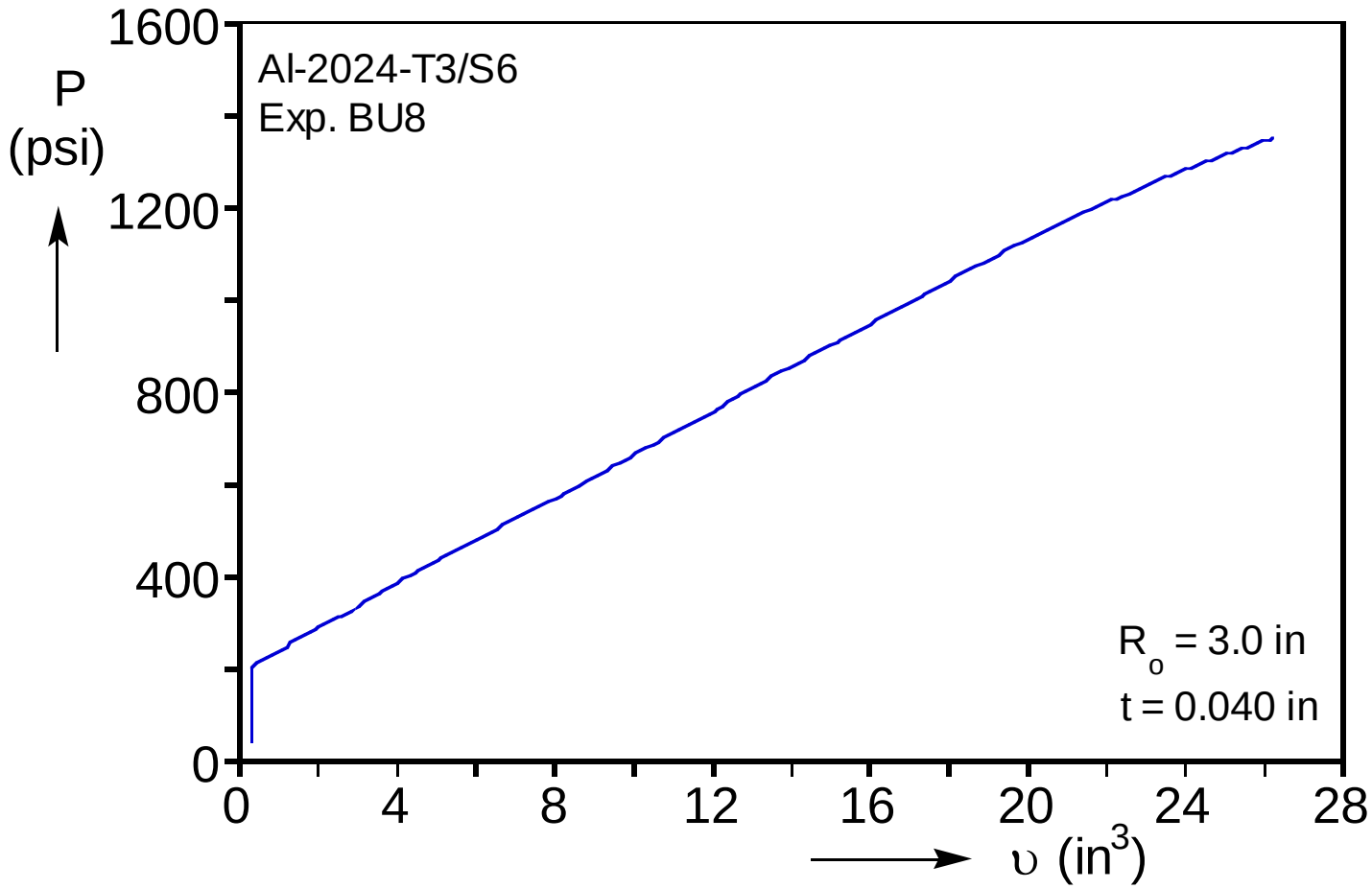

Figure 4.3 Pressure-volume response of the bulge test BU8/S6.

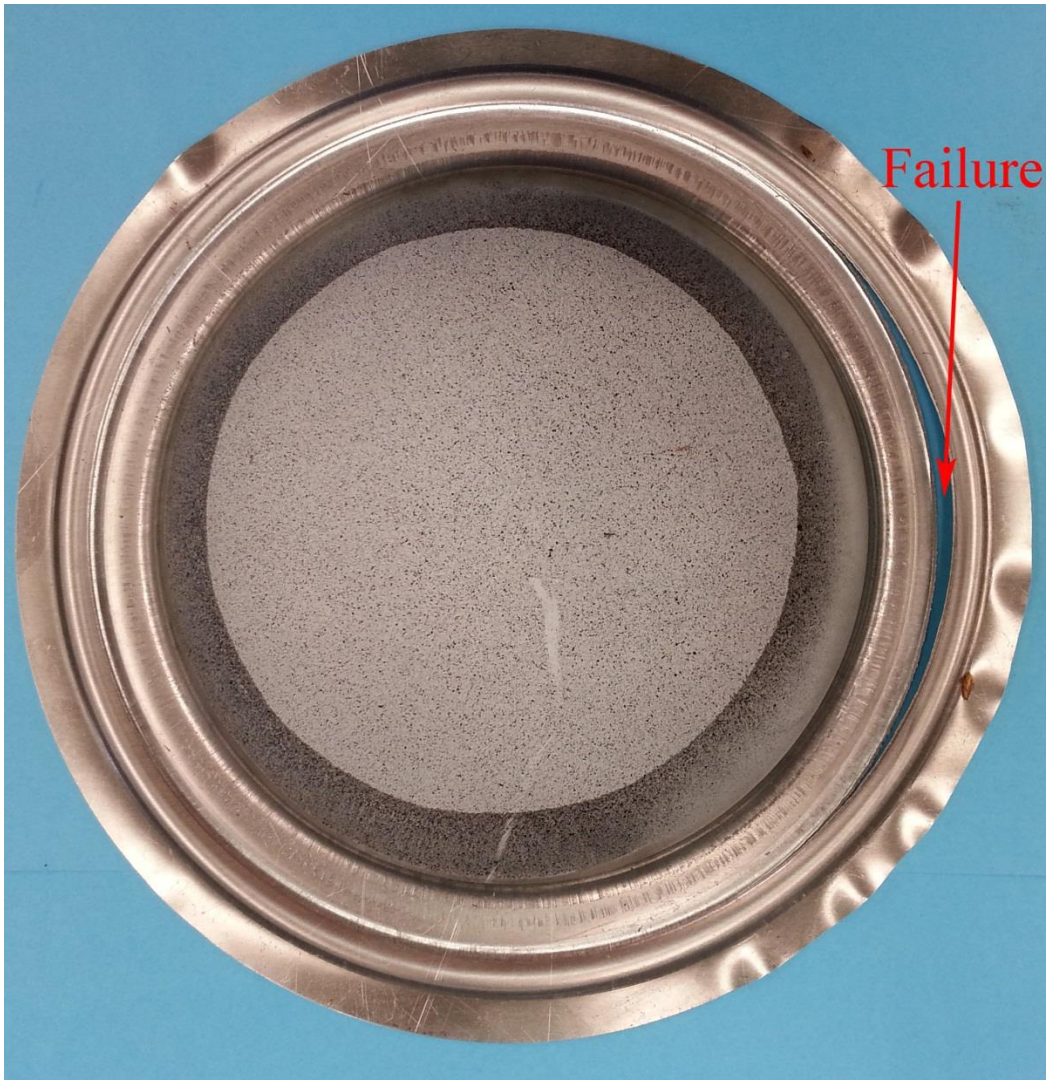

Figure 4.4 Test specimen for Exp. BU8 after failure.

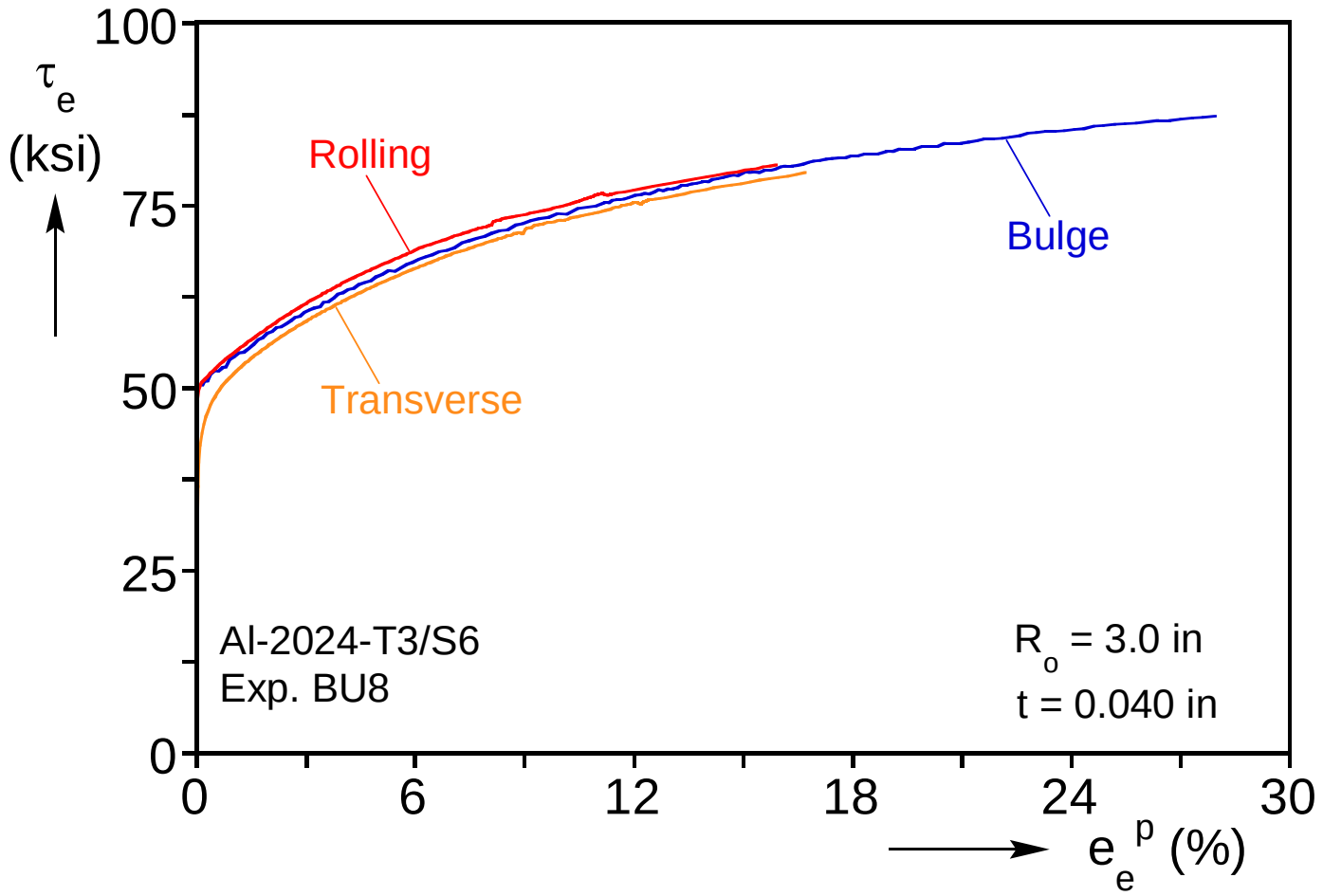

Figure 4.5 Equivalent stress-plastic equivalent strain response extracted from Exp. BU8.

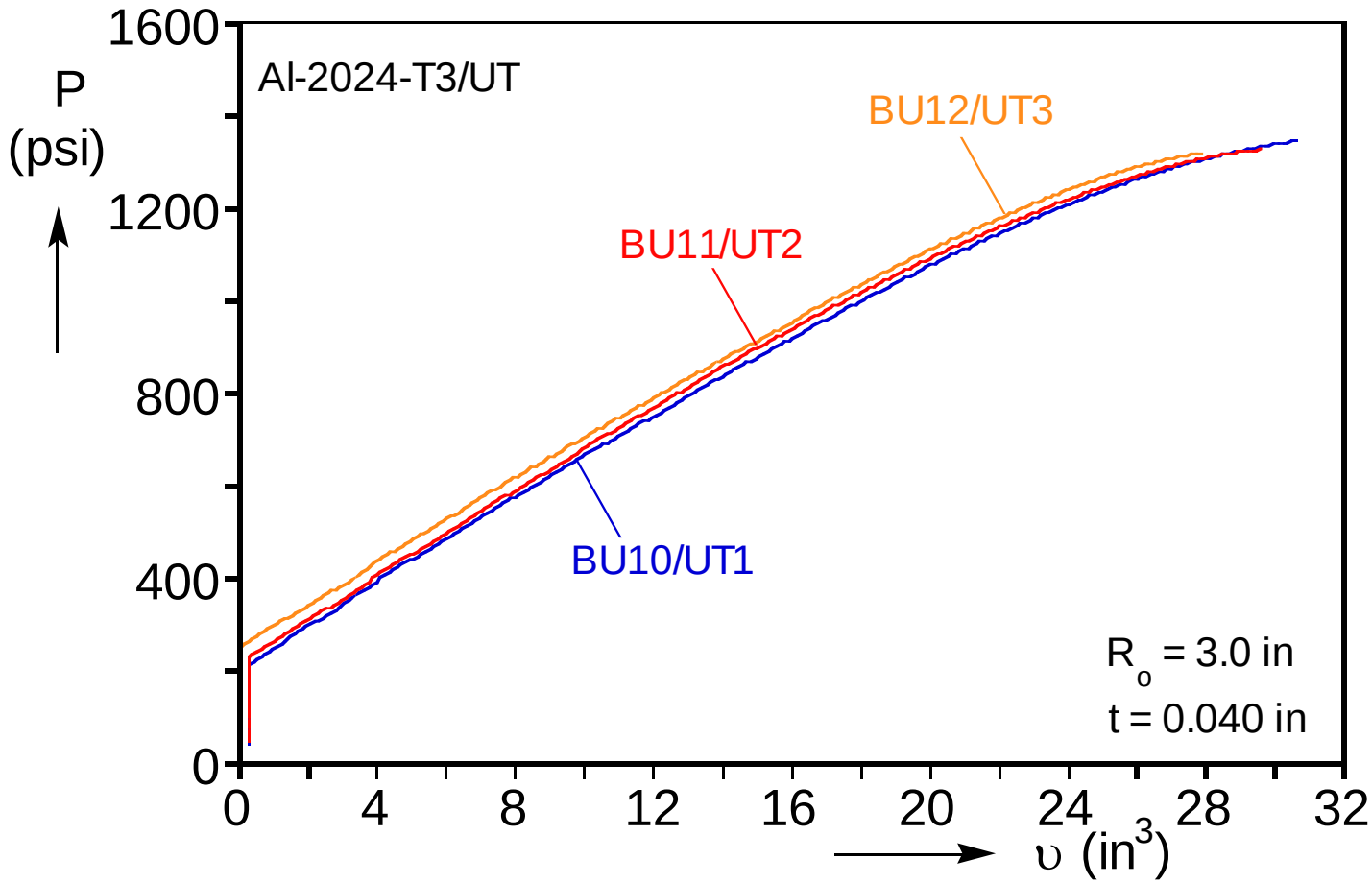

Figure 4.6 Pressure-volume response of the bulge tests BU10/UT1, BU11/UT2, and BU12/UT3.

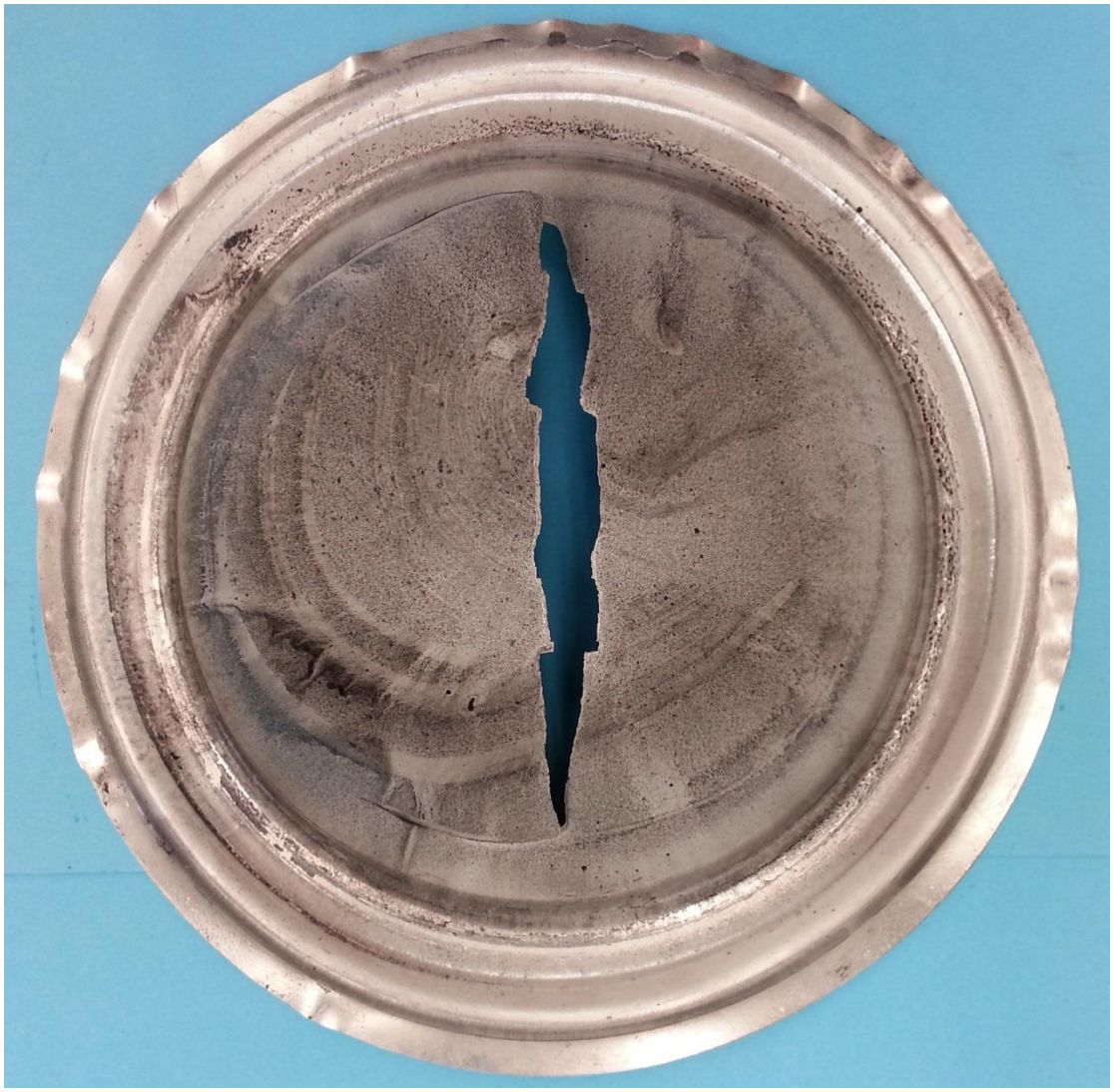

Figure 4.7 Test specimen for Exp. BU10 after failure.

Figure 4.8 Test specimen for Exp. BU11 after failure.

Figure 4.9 Test specimen for Exp. BU12 after failure.

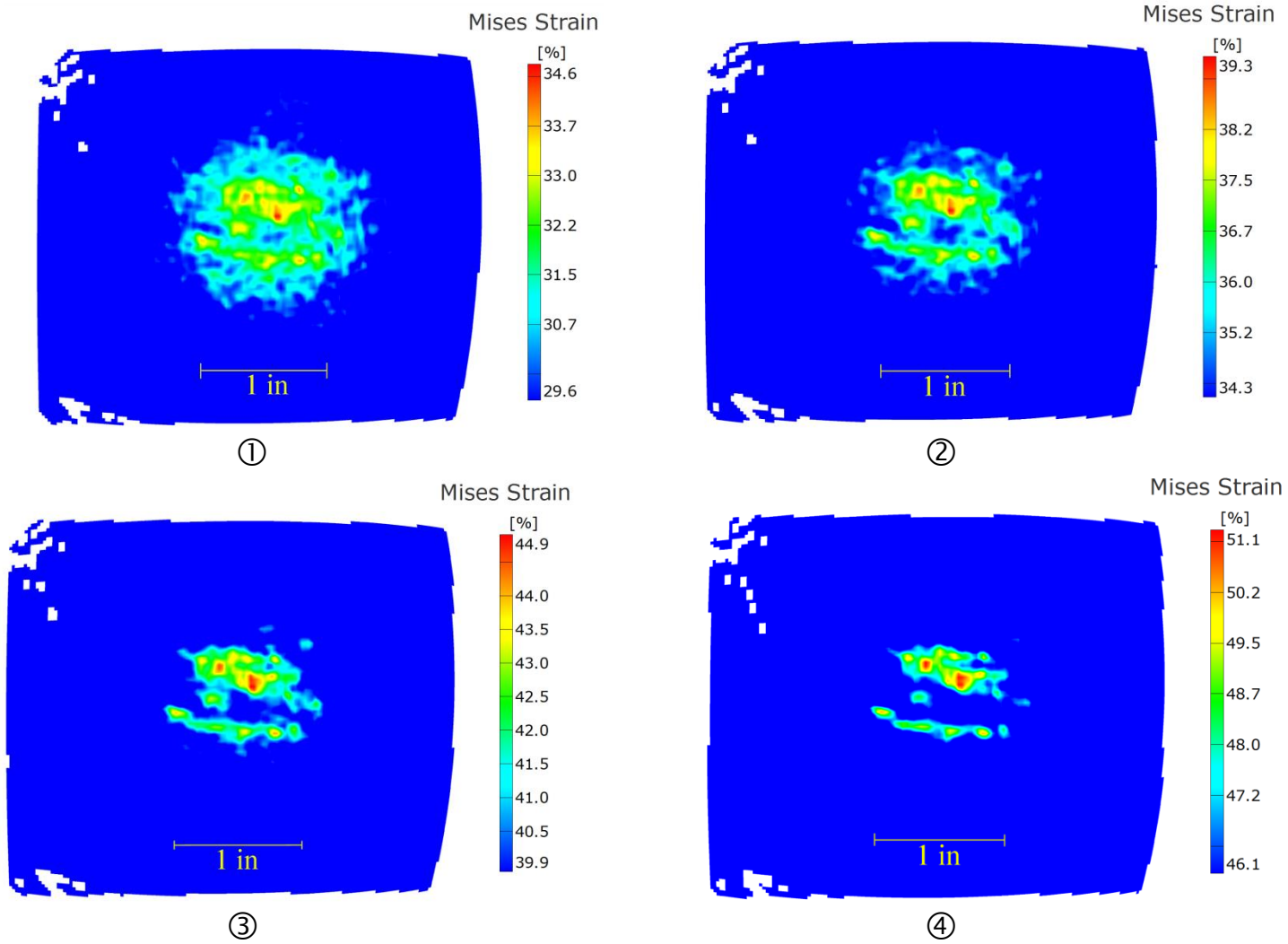

Figure 4.10 Evolution of the localization at the apex of specimen BU12— numbers correspond to response in Figure 4.11.

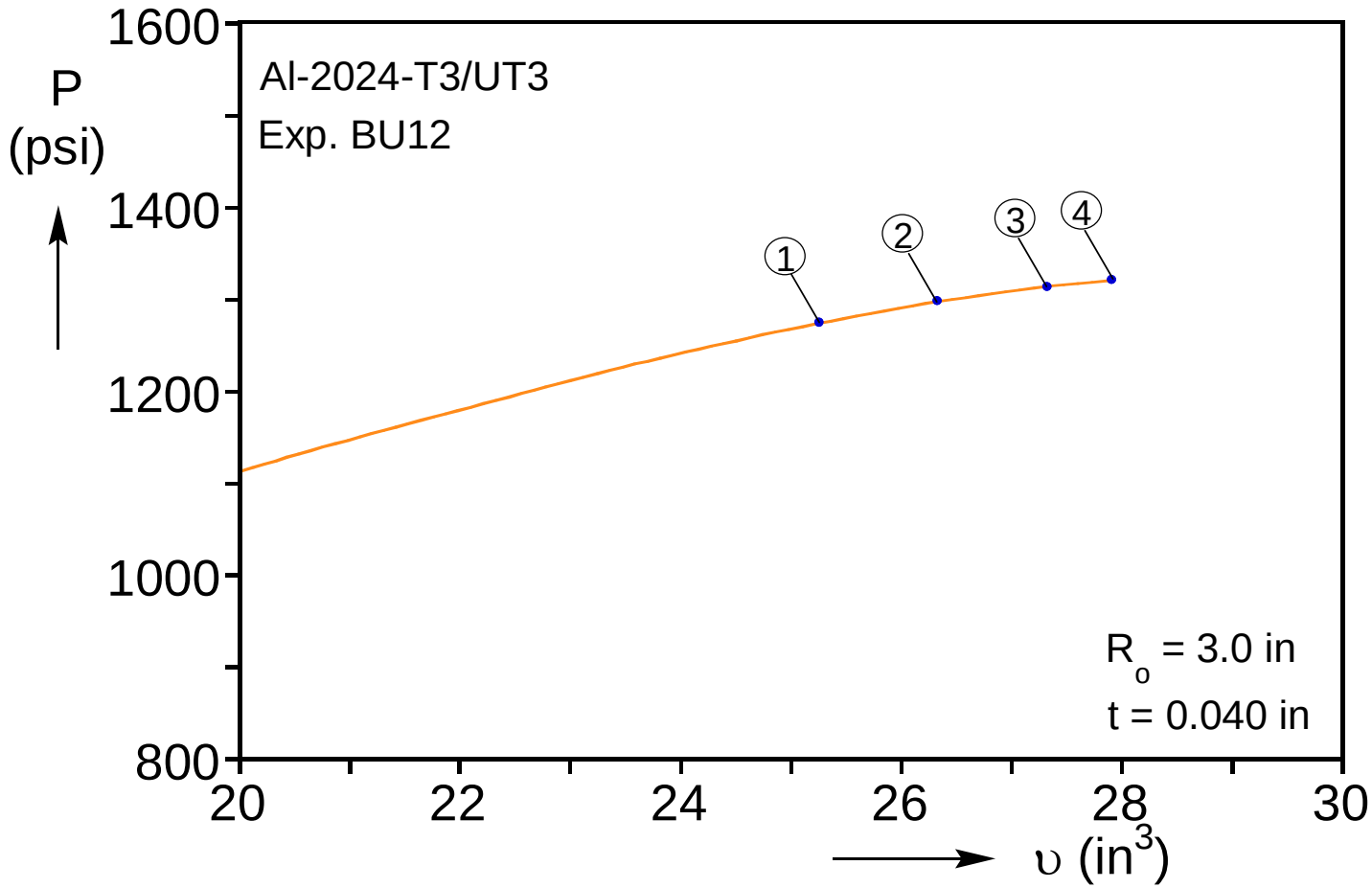

Figure 4.11 Expanded pressure-volume response in the neighborhood of the pressure maximum for Exp. BU12— numbered bullets correspond to images in Figure 4.10.

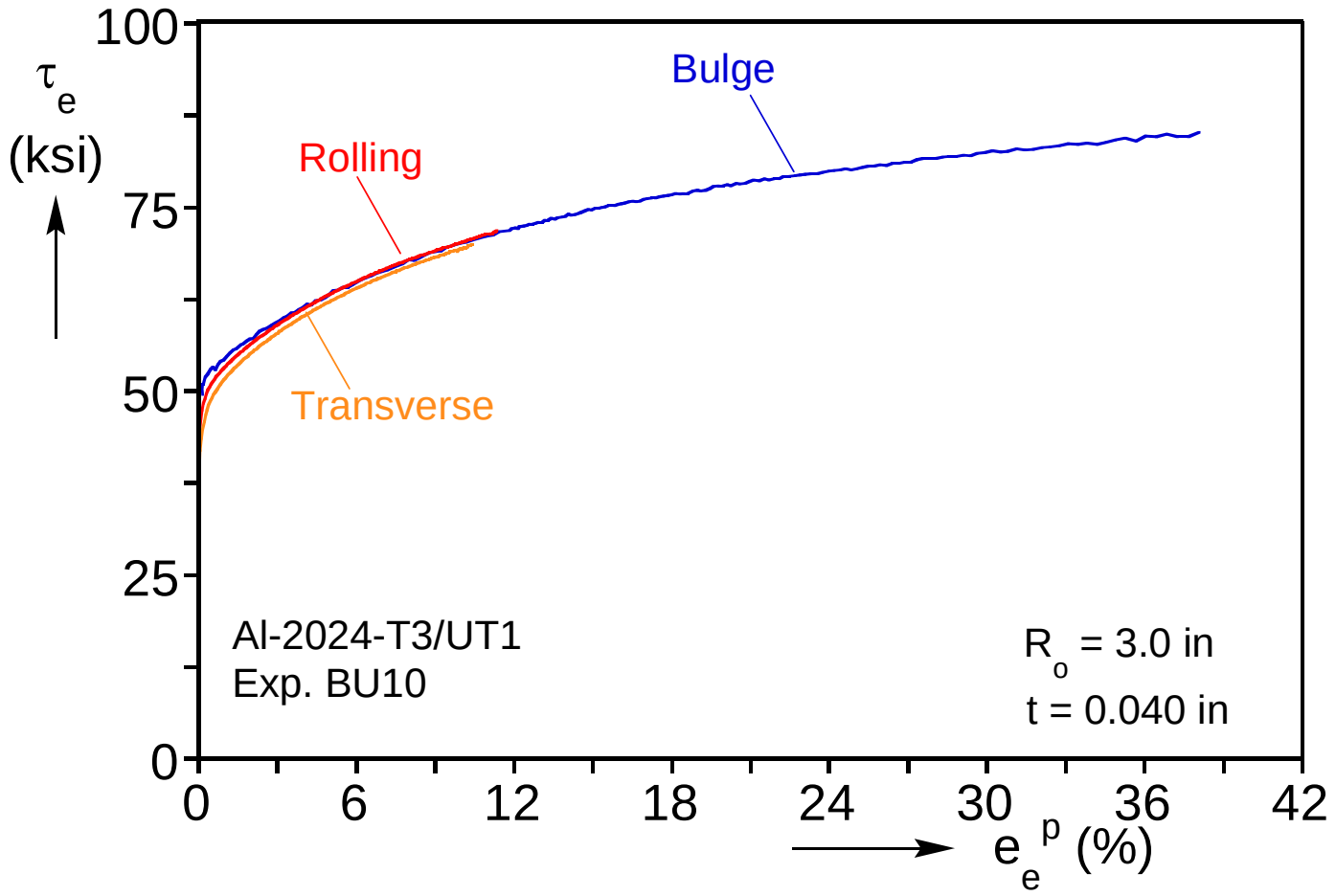

Figure 4.12 Equivalent stress-plastic equivalent strain response extracted from Exp. BU10.

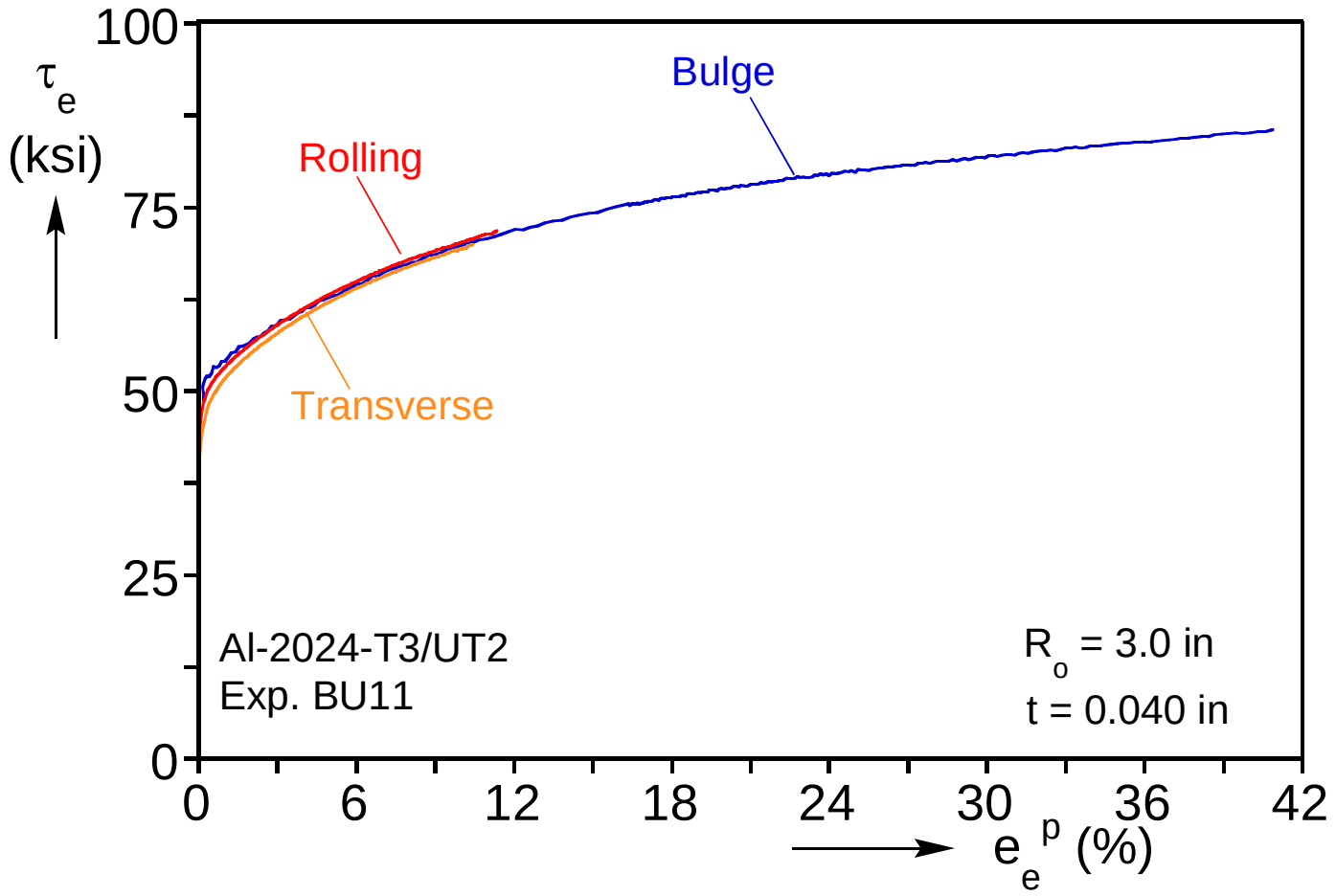

Figure 4.13 Equivalent stress-plastic equivalent strain response extracted from Exp. BU11.

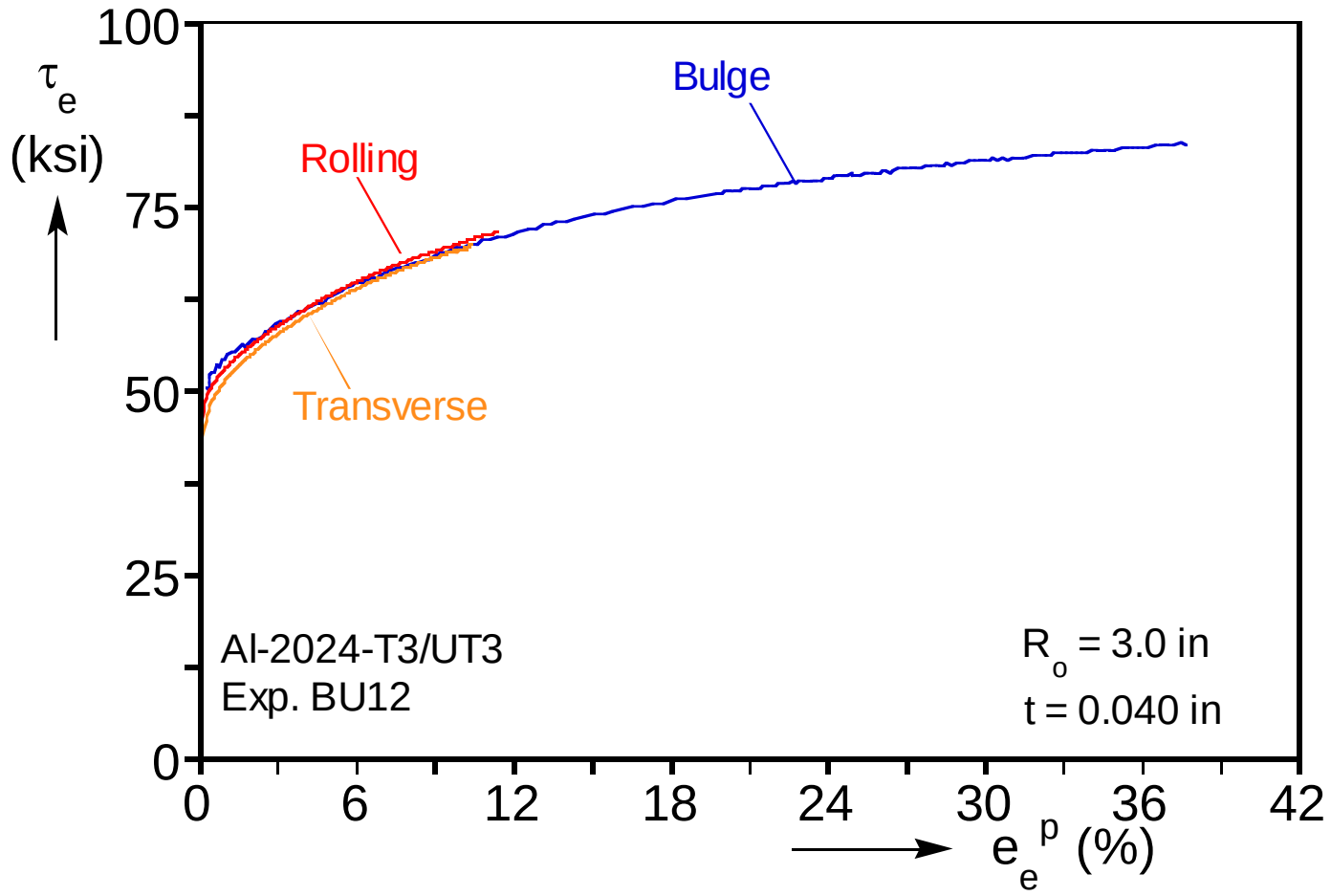

Figure 4.14 Equivalent stress-plastic equivalent strain response extracted from Exp. BU12.

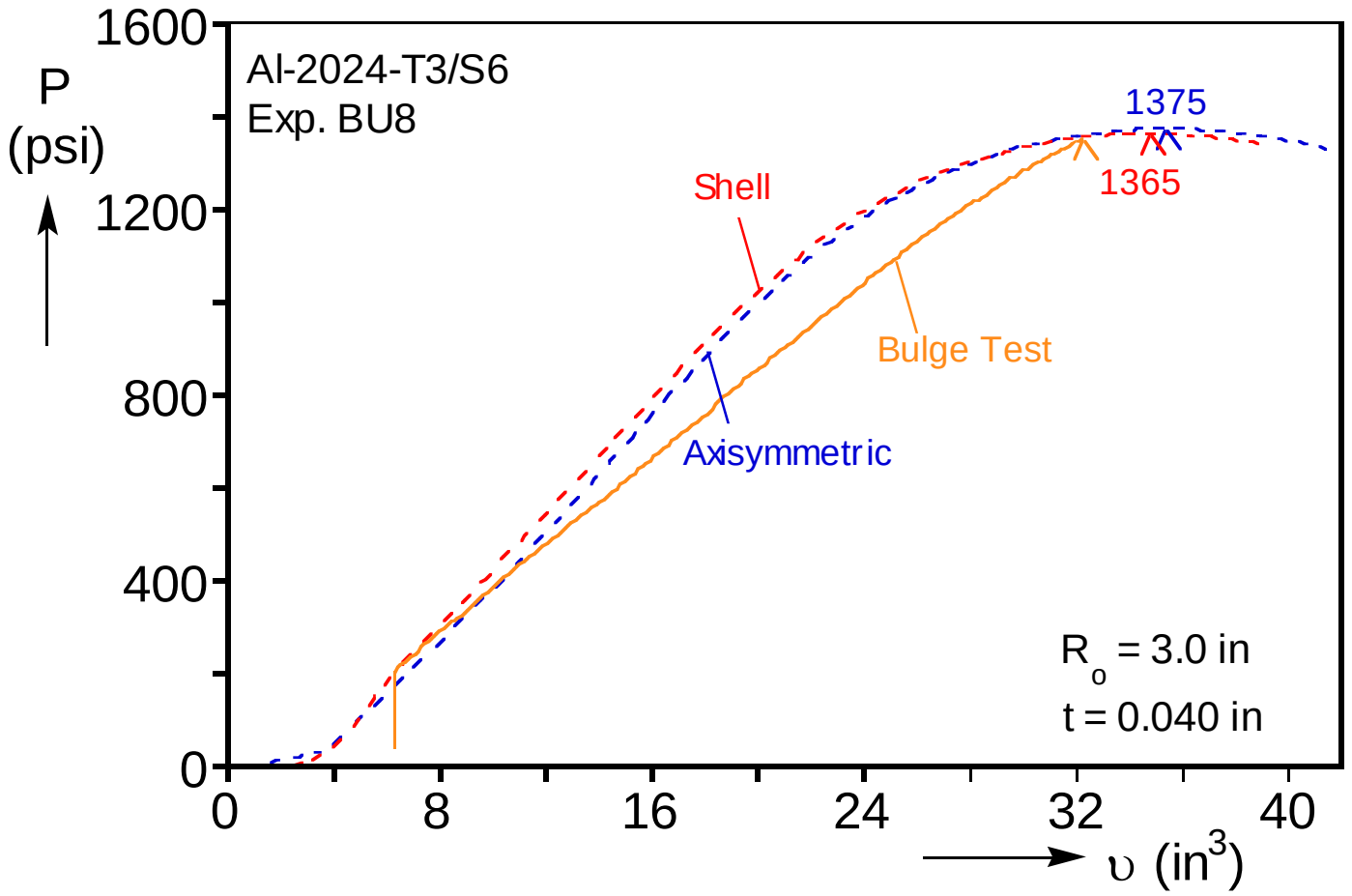

Figure 4.15 Comparison of measured pressure-volume response to numerical calculations for Exp. BU8.

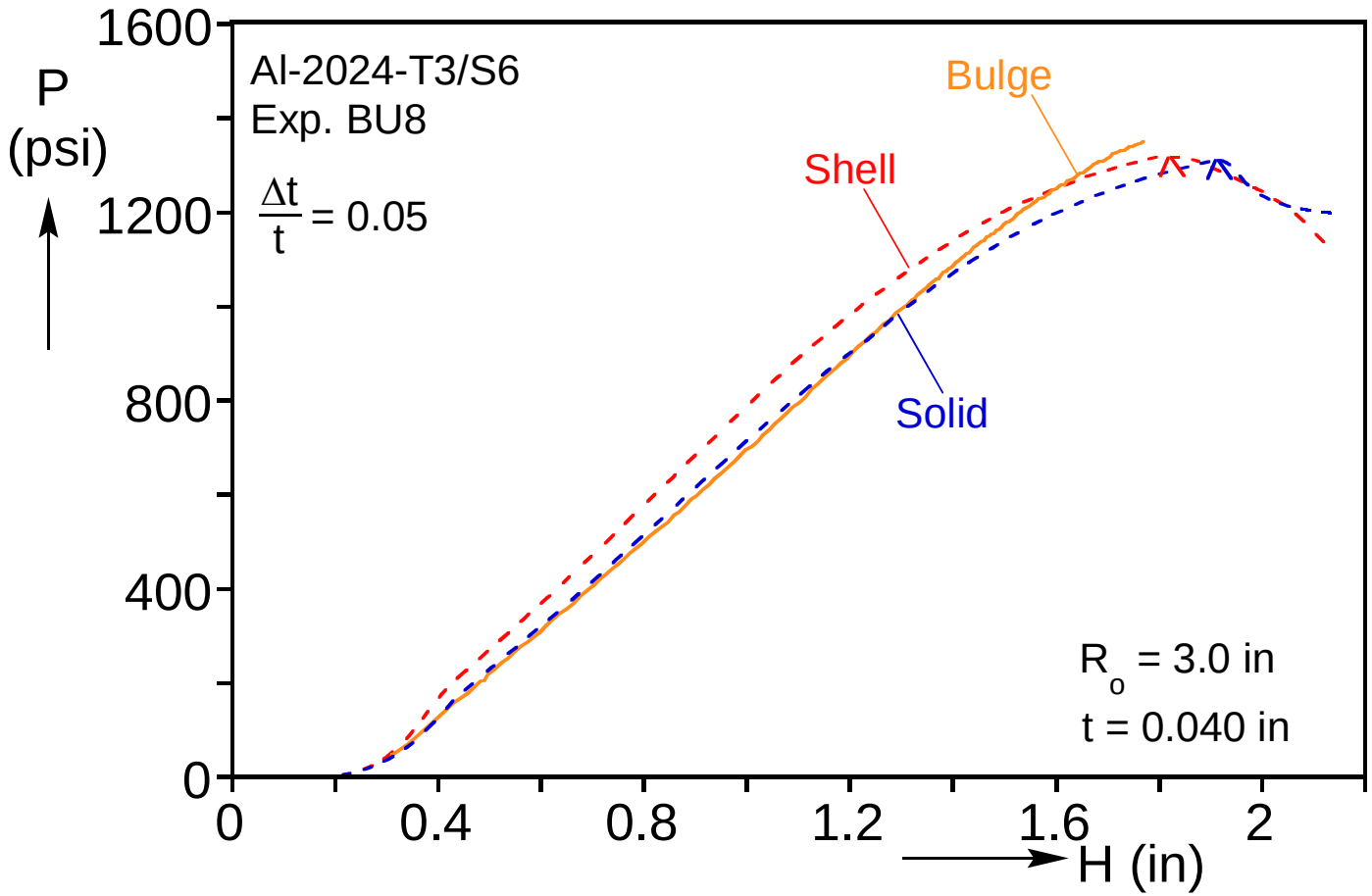

Figure 4.16 Comparison of measured pressure-height response to numerical calculations for Exp. BU8.

Appendix A

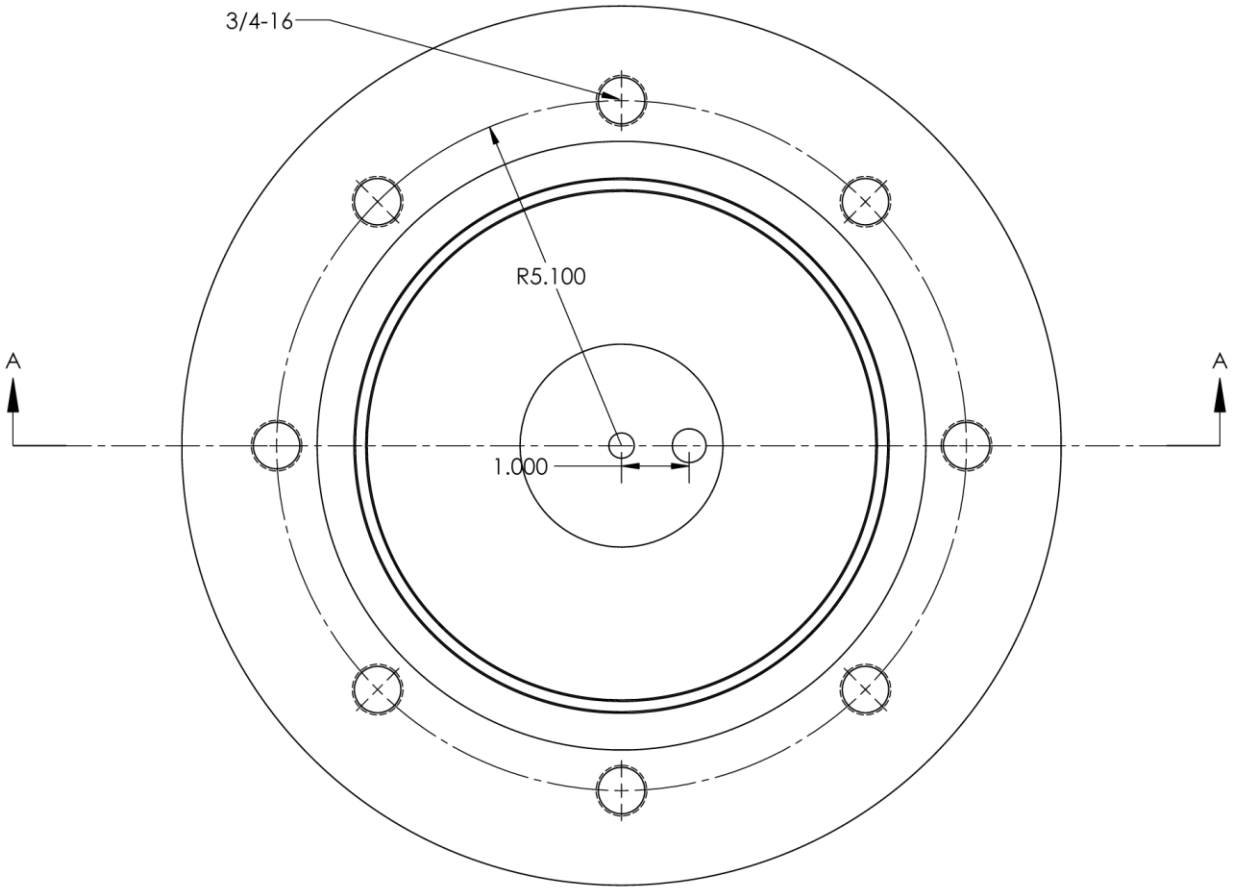

Figure A.1a Base plate: top view.

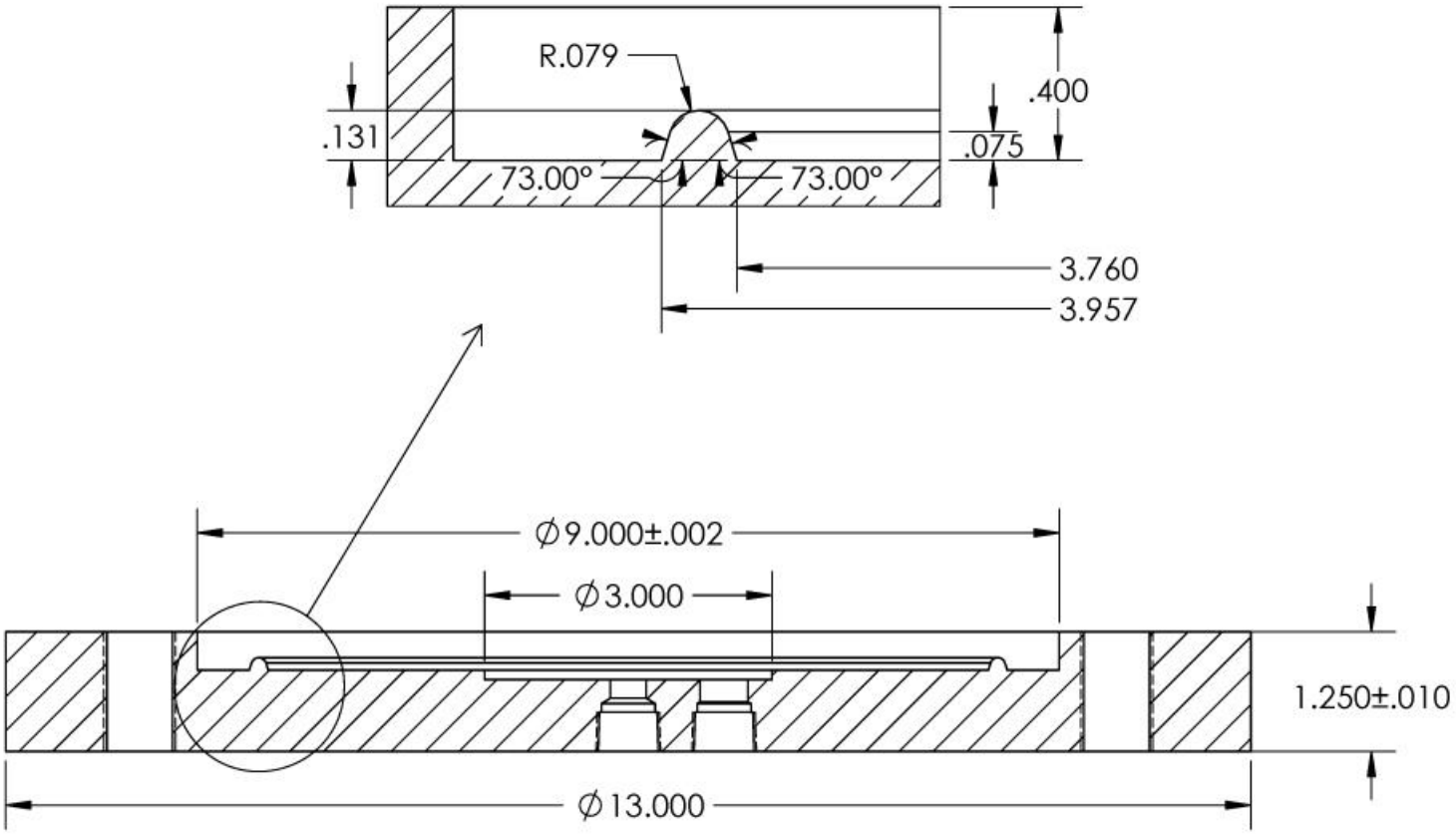

Figure A.1b Base plate drawing: cross-sectional view.

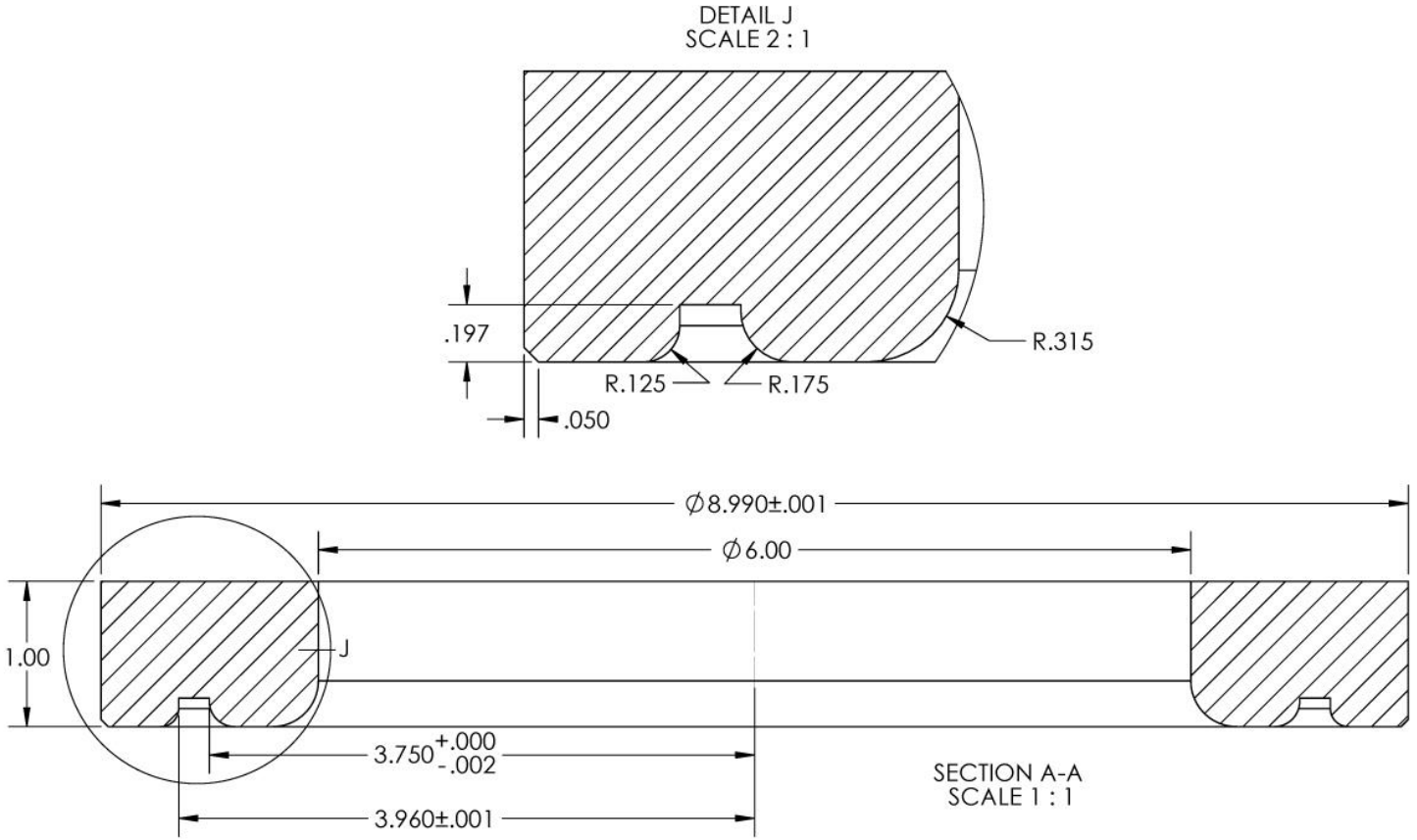

Figure A.2 Clamping ring drawing: cross-sectional view.

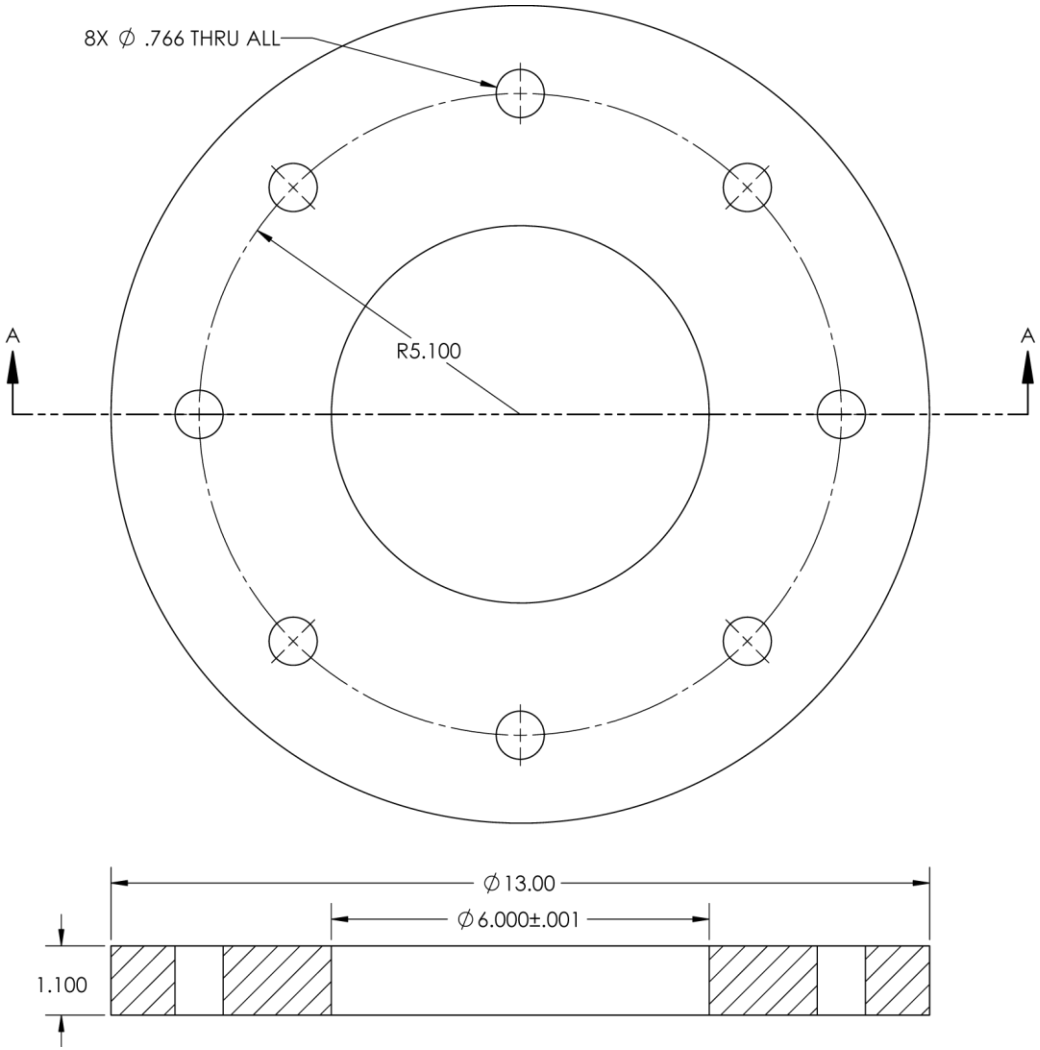

Figure A.3 Closing plate drawing: top and cross-sectional views.

Appendix B

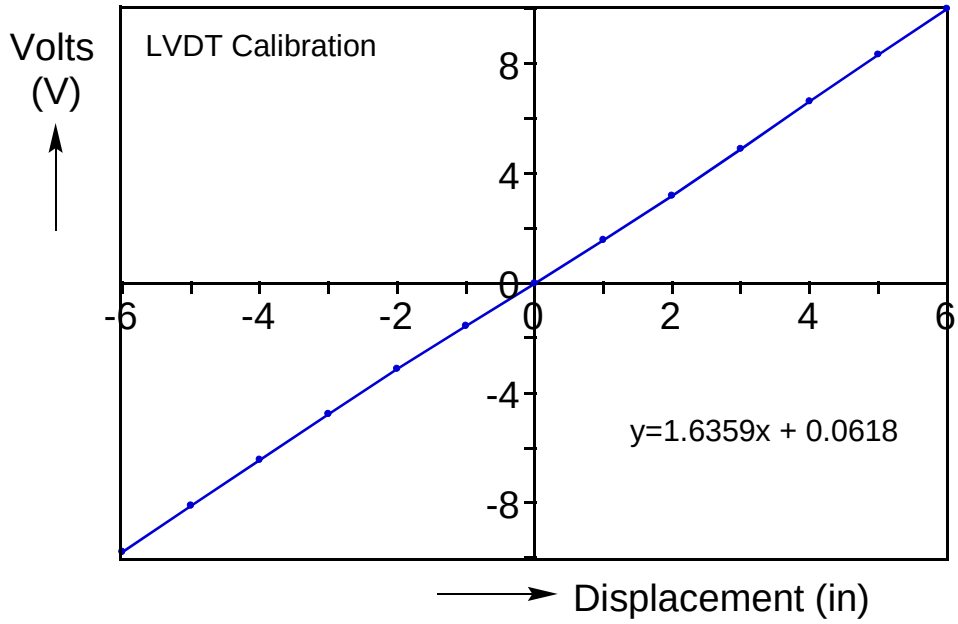

Figure B.1 Calibration of the LVDT.

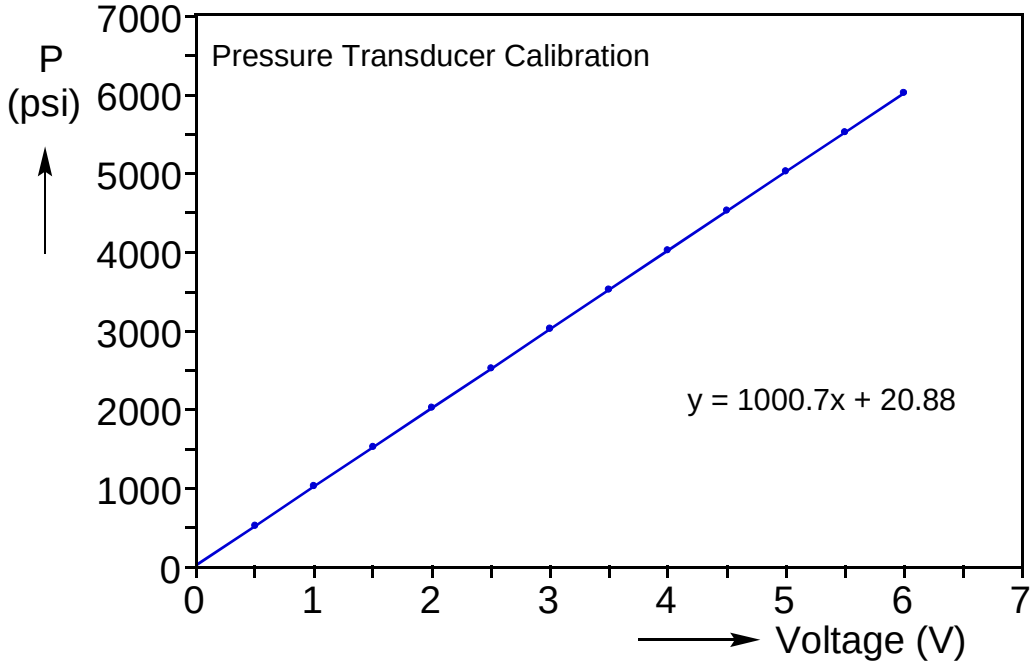

Figure B.2 Calibration of the pressure transducer.

References

ARAMIS User Information-Hardware. GOM Optical Measuring Techniques, 21 June 2011. PDF

ARAMIS User Manual-Software. GOM Optical Measuring Techniques, 23 May 2011. PDF

Bridgman, P.W., 1944. The stress distribution at the neck of a tension specimen. *Trans. American Society Metals* **32**, 553-574.

Chakrabarty, J and Alexander, J.M., 1970. Hydrostatic bulging of circular diaphragms. *Journal of Strain Analysis* **5**, 155-161.

Dziallach, S., Bleck, W., Blumbach, M., Hallfeldt, T. 2007. Sheet metal testing and flow curve determination under multiaxial conditions. *Advanced Engineering Materials* **9**, 987-994.

Giagmouris, T., Kyriakides, S., Korkolis, Y.P., and Lee, L.-H. (2010). On the localization and failure in aluminum shells due to crushing induced bending and tension. *Int'l J. Solids Struct.* **47**, 2680-2692.

Hill, R., 1950. A theory of plastic bulging of a metal diaphragm by lateral pressure. *Philosophical Magazine* **7**, 1133-1142.

Koç, M, Billur, E, Cora, O.N., 2010. An experimental study on the comparative assessment of hydraulic bulge test analysis methods. *Materials and Design* **32**, 272-281

Korkolis, Y.P. and Kyriakides, S., 2008a. Inflation and burst of anisotropic tubes for hydroforming applications. *International Journal of Plasticity* **24**, 509-543.

Lăzărescu, L., Comsa, D.S., Nicodim, I., Ciobanu, I., Banabic, D, 2012. Characterization of plastic behaviour of sheet metals by hydraulic bulge test. *Transactions of Nonferrous Metals Society of China* **22**, 275-279.

Mellor, P. B., 1956. Strech forming under fluid pressure. *Journal of the Mechanics and Physics of Solids* **5**, 41-56.

Rana, R., Singh, S.B., Bleck, W., Mohanty, O.N., 2010. Biaxial stretching behavior of a copper-alloyed interstitial-free steel by bulge test. *Metallurgical and Materials Transactions A* **41**, 1483-1492.

Ranta-Eskola, A.J., 1979. Use of the hydraulic bulge test in biaxial tensile testing. *International Journal of Mechanical Sciences* **21**, 457-465.

Swift, H. W., 1952. Plastic instability under plane stress. *Journal of the Mechanics and Physics of Solids* **1**, 1-18.

Tardif, N., Kyriakides, S., 2012. Determination of anisotropy and material hardening for aluminum sheet metal. *International Journal of Solids and Structures* **49**, 3496-3506.

Yanaga, D., Kuwabara, T., Uema, N., Asano,M. 2012. Material modeling of 6000 series aluminum alloy sheets with different density cube textures and effect on the accuracy of finite element simulation. *International Journal of Solids and Structures* **49**. 3488-3495

Young, R.F., Bird, J.E., Duncan, J.L., 1981. An automated hydraulic bulge tester. *Journal of Applied Metal Working* **2**, 11-18.

Vita

John Philip Mersch was born and raised in Bloomington-Normal, IL. He attended University High School and then the University of Illinois Urbana-Champaign, where he received his bachelor's degree in General Engineering in May of 2011. The following fall, he enrolled at The University of Texas at Austin to pursue a Master of Science degree in Engineering Mechanics. In the fall of 2013, he moved to Albuquerque, New Mexico to accept a position with Sandia National Laboratories.

jmersch16@gmail.com
This thesis was typed by the author.